



Durham E-Theses

A study of radio continuum emission of the Milky Way Galaxy

Sanguansak, Nuanwan

How to cite:

Sanguansak, Nuanwan (1996) *A study of radio continuum emission of the Milky Way Galaxy*, Durham theses, Durham University. Available at Durham E-Theses Online: <http://etheses.dur.ac.uk/5399/>

Use policy

The full-text may be used and/or reproduced, and given to third parties in any format or medium, without prior permission or charge, for personal research or study, educational, or not-for-profit purposes provided that:

- a full bibliographic reference is made to the original source
- a [link](#) is made to the metadata record in Durham E-Theses
- the full-text is not changed in any way

The full-text must not be sold in any format or medium without the formal permission of the copyright holders.

Please consult the [full Durham E-Theses policy](#) for further details.

A STUDY OF RADIO CONTINUUM EMISSION OF
THE MILKY WAY GALAXY

by

Nuanwan Sanguansak

The copyright of this thesis rests with the author.
No quotation from it should be published without
his prior written consent and information derived
from it should be acknowledged.

A thesis submitted to the University of Durham in accordance
with the regulation for admittance to the degree of Doctor of
Philosophy

Department of Physics
University of Durham
March, 1996



23 MAY 1996

Abstract

The synchrotron emissivity distribution of the Milky Way Galaxy has been modelled from the 408 MHz allsky survey of Haslam et al.(1982) after separation of its thermal component with the help of IRAS 60 micron emission(Broadbent et al., 1989). We have refined the spiral arm pattern in the inner part of the Galaxy by including a bar at the Galactic centre and an updated the Galactic distance scale and obtained fitted free parameters. At 408 MHz, there is very little absorption in the interstellar medium and the line of sight distribution of synchrotron emissivity was inferred mainly from its presumed relationship to the other tracers of spiral structure via these fitted free parameters. At lower frequencies, the absorption of synchrotron emission due to thermal electrons becomes significant and can give direct information of the nonthermal distribution along the line of sight. We have modelled the distribution of thermal electrons according to our synchrotron arm model and an alternative model based on pulsar dispersion measures using the Galactic rotation curve and the surveys of the distribution of H166 α emission. We have then used our synchrotron model applied at lower frequencies including the absorption to compare with the surveys of Dwarakanath et al.(1990) at 34.5 MHz and Jones and Finlay(1974) at 29.9 MHz. The result confirms that the absorption model of the synchrotron emissivity in the Galactic plane is broadly correct and illustrates the potentials of the absorption technique. However we were not able to distinguish the two models of ionised hydrogen spiral structure. To do this, recombination line surveys with improved frequency resolution are required. Using a new value of the cosmic ray gradient in the Galaxy from diffuse gamma-ray emission we obtain the separate variation of magnetic field and cosmic ray electron density. We give the global properties of the thermal and nonthermal emission that our model implies.

Acknowledgements

I am extremely grateful to my supervisor, Dr. J.L. Osborne, for his help, guidance, patience and encouragement throughout the period of my studies.

Institute of Promotion of Science and Technology of Thailand is thanked for sponsoring me during the period of this work.

I would like to thank the computer facilities at Durham University, especially the local Starlink node, whose manager is Mr. A.P. Lotts for the general running of the clusters and for assistance in solving computing problems that I have encountered, especially when the disk Baksan broke down.

The friendship and help which I have received from many other members of and visitors to the Physics Department at Durham are gratefully appreciated. I would like to thank Adrian Askew, Adnan Bashir, Chris Caron, Henry Day, Richard Dodson, Lilian Graham, Amy Hong, Alexandar Iskandar, Lydia Kwong and Yang Wang for putting up with me.

Finally thanks to my family and friends who have given me lots of support and encouragement, especially to my parents to whom I would like to dedicate this thesis.



Preface

The studies reported in this thesis were carried out between January 1992 and February 1996 while the author was a research student under the supervision of Dr. J.L. Osborne in the Physics Department of the University of Durham. None of the material has been submitted previously for a degree at this or any other university. The initial conception of the project was due to Dr. Osborne and the some of the conclusions were drawn following discussions with him. The synchrotron model of the Galaxy of Chapter 3 was developed from earlier models of the Durham Group but this development and the work on absorption has been performed almost entirely by the author. All of the computational and digitisation work has been done by the author. Progress reports on this work have been presented, as papers, at the International Astronomical Union Symposium no. 169, Den Haag, 1994 and at the 24th International Cosmic Ray Conference, Rome 1995, and in written form, in the following proceedings.

Sanguansak, N. & Osborne, J.L., 1994. Abstract in: *IAU symposium 169, Unsolved Problems of the Milky Way*, Eds. L. Blitz and J. Binney, Kluwer Academic Publishers, In press.

Osborne, J.L. & Sanguansak, N., 1995. *Proc. 24th International Cosmic Ray Conference, Rome*, v3 ,p33.

Contents

Chapter 1 – Introduction

1.1 Historical review	I-1
1.2 The aim of the present work	I-5
1.3 Galactic spiral structure	I-6
1.4 Dynamics of spiral structure	I-8

Chapter 2 – Thermal and nonthermal theory

2.1 Synchrotron radiation theory	II-1
2.2 Thermal radiation	II-5
2.3 408 MHz all-sky survey	II-10
2.4 Thermal - nonthermal separation technique	II-13

Chapter 3 – Synchrotron emission model

3.1 Introduction	III-1
3.2 The electron flux density	III-2
3.3 The galactic magnetic field	III-8
3.3.1 Measurement of the field	III-8
3.3.2 Alignment of magnetic field in the arms	III-11
3.3.3 Gas compression factor in spiral arms	III-12
3.3.4 Large-scale radial variation of magnetic field	III-14
3.3.5 The spiral arm pattern	III-18

3.3.6 Field irregularities in arm and interarm regions	III-23
--	--------

Chapter 4 – The absorption model

4.1 Low frequencies surveys	IV-2
4.1.1 The 34.5 MHz GEETEE surveys	IV-3
4.1.2 The 29.9 MHz Fleurs surveys	IV-7
4.2 The distribution of ionised hydrogen	IV-11
4.3 The distribution of electron density according to TC	IV-23
4.4 The predicted and observed absorption	
4.4.1 Calculation of the predicted absorption	IV-31
4.4.2 Comparison with the ‘observed’ absorption	IV-36

Chapter 5 – Conclusion

5.1 Summary	V-1
5.2 The magnetic field and cosmic ray electron density	V-8
5.3 Global emission of the Galaxy	V-13
5.4 Future work	V-13
List of symbols in general use in this thesis	L-1
References	R-1

Acknowledgements

Chapter 1

Introduction

A thousand miles' journey begins from the spot under one's feet.

LAO TZU

1.1 Historical review

The starting point of radio astronomy was in the experiments of Karl G Jansky in 1931. He built a rotating antenna array operable at 14.6 m(20.5 MHz) in order to study radio disturbances. He found that he could identify the static into three groups as follows: intermittent and strong, intermittent and weak, and very steady and weak. The first two types were from local and distant thunderstorms. But the origin of the third type was not known. In 1932, he noted that the direction of this static changed gradually through nearly 360° in 24 hours. Because of this periodic behavior, he speculated that it might be associated with the Sun. However in 1933, he found that the direction of this disturbance was not in the same position as the Sun but came from a fixed position in space which was near right ascension 18^h and declination -10°. This position was in the general direction of the centre of our galaxy. In 1935, he was able to demonstrate that radiation was received continuously when an antenna swept along the galactic plane. A maximum in the emission intensity appeared in the direction of the galactic centre and a minimum

appeared in the anticentre direction. He concluded that the sources of this radiation are located either in the stars themselves or in the interstellar matter distributed throughout the Galaxy. He noted that if stars were the source then strong radiation should be observed from the Sun, but he had not detected any solar radiation. In 1937, Whipple and Greenstein suggested that the observations referred to the Rayleigh - Jeans tail of the blackbody distribution of interstellar dust at 30 K.

In 1938, Reber made observations at frequencies 3300 and 910 MHz. The received power would have been greater at these frequencies if it followed the blackbody radiation law, but he was not able to detect any radiation. In 1939, he was at last able to detect the radiation at 162 MHz, and it also showed a marked concentration in the plane of the Galaxy. In 1940, he interpreted his fluxes as arising from thermal bremsstrahlung (free - free radiation) in a hot $T_e = 10^4$ K, dense ($n_e = 1\text{cm}^3$) interstellar gas. Henyey and Keenan showed that it was inconsistent with Jansky's lower frequency measurements which required a thermal medium with $T_e = 1.5 \times 10^6$ K. Reber(1944) interpreted secondary maxima in the longitudinal distribution at 162 MHz as being the directions tangential to spiral arms and concluded that spiral arms existed in the directions of Cygnus, Cassiopeia and Canis Major. This was the first use of the galactic continuum radiation in mapping the structure of the Galaxy. The result confirmed that if stellar radiation produced the galactic radio background, then a population of radio stars quite distinct from the Sun was needed.

Alfvén and Herlofson(1950) considered stellar models that might produce extremely high radio brightness temperatures. They suggested that the emission might originate from highly energetic electrons trapped in the magnetic fields of such stars. The resulting radiation would then be synchrotron emission. Kiepenheuer(1950) suggested a modified picture in which relativistic cosmic ray electrons spiral around the interstellar magnetic field and their synchrotron emission is re-

sponsible for the galactic radio background. In 1953, Shklovsky noted that synchrotron radiation should be polarized in order to explain the emission from the Crab nebula. It is now clear that in the frequency range 85 to 408 MHz, where the most complete large scale continuum surveys of the radio sky have been made, the major part of the emission is due to synchrotron radiation. This is termed 'nonthermal' emission. The remainder, the 'thermal' emission is due to bremsstrahlung of the thermal electrons as proposed by Reber. As we show in Chapter 2, the thermal component coming from an optically thin plasma has a rather flatter spectrum than the nonthermal component and at 5 GHz the two components contribute roughly equally in typical directions close to galactic latitude, $b = 0^\circ$. Beyond $|b| \sim 8^\circ$ the nonthermal component dominates to much higher frequencies. As the frequency decreases below 85 MHz the thermal plasma begins to become optically thick and the thermal regions are seen in absorption.

Mills(1959) showed that the radio continuum was correlated with the spiral arms of the Galaxy. Following on from this a number of workers produced models of the 2-dimensional distributions of the radio continuum emissivity in the plane of the Galaxy to fit the observed 1-dimensional profile of emission along the galactic plane. These distributions can be produced in two ways. *Either*, the 'Spiral Arm Method', the Galaxy's spiral arm pattern, based on other, independent, observations, can be used with a model for the variation of magnetic field and relativistic electron density across an arm, *or*, the 'Unfolding Method', the observed profiles may be unfolded, under some assumed symmetries to give the distribution directly. The Durham group has made a long term contribution to this work. French and Osborne(1976) applied the Spiral Arm Method by combining the spiral arm model of Georgelin & Georgelin, based on observations of HII regions, with the map of neutral hydrogen outside the solar circle of Verschuur. Comparison was made with the 'observed' profile at 150 MHz of Landecker and Wielebinski(1970). Brindle et

al.(1978) extended the model to 3-dimensions to compare with the complete 150 MHz map.

A disadvantage of using the Landecker and Wielebinski map was that in fact it was a composite of a number of surveys made at frequencies from 85 to 178 MHz, scaled then added together, and of differing and rather large beam shapes ($3.5^\circ \times 3.8^\circ$, $2.2^\circ \times 2.2^\circ$ and $5^\circ \times 1.25^\circ$). Much improved radio continuum data were provided by the allsky map of Haslam et al.(1982). This was made from surveys at a common frequency of 408 MHz done at Effelsberg, Jodrell Bank and Parkes, and smoothed slightly to a Gaussian beam with Half Power Beam Width (HPBW) of $51'$. Phillipps et al.(1981a), collaborating with Haslam on the prepublication data, from the galactic plane profile produced a map of the emissivity distribution in the galactic plane. This time the Unfolding Method was used to convert from 1 to 2-dimensions the assumption being made that the galactic plane could be represented as being divided into 60 logarithmic spiral sections of 12° pitch angle each having its own emissivity level but all having the same radial dependence of emissivity. The Unfolding Method is straightforward to apply and can be used to obtain global parameters of the Galaxy such as the total synchrotron emission. The reality of the galactic plane distribution depends, however, on how well the Galaxy follows the assumed symmetry. At 408 MHz typically 20% of the emission observed at $b = 0^\circ$ is thermal although particular features in the galactic plane profile may be almost entirely thermal. It could be argued that without a prior separation of the thermal features an attempt to obtain a detailed distribution of the synchrotron emissivity in the plane by the Spiral Arm Method is not justified. Nevertheless Kearsy(1983) used it on the 408 MHz data in an unpublished part of his Ph.D Thesis. Phillipps et al.(1981b) then proceeded to derive a 3-dimensional model of the distribution of the synchrotron emissivity from the 2-dimensional map of the whole sky. Again an unfolding technique was used to determine the variation of emissivity with distance,

z , from the galactic plane. As the proportion of thermal emission decreases rapidly with z it is not important in this case to have a detailed separation of the thermal component and we believe that their deduced z -variation remains valid.

Broadbent et al.(1989) developed a technique for separating the thermal and nonthermal components of the radio continuum emission based on the strong empirical correlation between the former and the 60 micron infrared emission as observed by the IRAS satellite. Further details of this are given in Chapter 2. When it was applied to the 408 MHz survey it gave a clearer picture of the synchrotron emission and Broadbent concluded her thesis work with a 3-D model of the emissivity distribution derived by the Spiral Arm method.

1.2 The aim of the present work

The aim of the present work has been first to refine the model of Broadbent taking into account some more recent information on spiral arm structure. We have also rescaled the model to put the sun at the presently accepted distance of 8.5 kpc from the galactic centre as opposed to the 10 kpc distance which was used in all previous Durham models.

By its nature a nonthermal emission region gives no direct evidence of its distance from the observer and judgement of the fit of the 3-dimensional model to the 2-dimensional observations has up to now been based only on the emission integrated along each line of sight. A new feature of the present work is to make use of the absorbing properties of the thermal component at low frequencies on a Galaxy wide scale to give a check on the relative distributions along the line of sight of the nonthermal emitting regions and the thermal, largely absorbing, regions. The thermal continuum does not of itself possess distance information but the regions of extended low density (ELD) ionised hydrogen gas which give the thermal bremsstrahlung also give a proportional intensity of recombination line

emission. By measuring the Doppler shift of this line emission and using knowledge of the differential rotation of the Galaxy one can infer the distance of the thermal regions. The ELD regions have appropriate optical depths for Galaxy wide studies at Decametre wavelengths. For our absorption studies we have used the recent 34.5 MHz survey of Dwarakanath and Uday Shankar(1990) for the first quadrant of galactic longitude and the older 29.9 MHz survey of Jones and Finlay(1974) for the fourth quadrant.

Although the distribution of the synchrotron emissivity in the Galaxy is interesting in itself as a feature of galactic morphology, of more fundamental concern is the information on the distribution of galactic magnetic field and cosmic ray electron density that it contains. In the concluding chapter we examine the independent evidence for variation of cosmic ray electron density and the variation of magnetic field that this implies.

1.3 Galactic spiral structure

In order to calculate synchrotron emission from the Galaxy we have to consider its spiral structure. There have been many efforts for tracing the spiral arm pattern of the Galaxy. There are three main tracers: 1) the recombination lines of HII regions, 2) the 21 cm emission of HI gas, and 3) the CO lines associated with molecular hydrogen.

HII regions surround young hot O and B type stars and are used as spiral tracers of spiral galaxies. HII regions can be seen optically or as thermal radio sources. In the plane of our Galaxy, beyond about 8 kpc from the Sun, because of dust it is difficult to make the optical detection of HII regions so radio measurement must be used. Therefore in the inner part of the Galaxy, HII regions are useful tracers because the ambiguity in their kinematic distances can be solved through the use of absorption spectra and optical measurements. Georgelin and Georgelin (1976)

studied the distribution of bright HII regions in the Galaxy which involved the determination of distance by using observations at optical and radio wavelengths. Distances measured from radio recombination lines are determined kinematically but there is a problem whether the HII region is at the 'near' or 'far' distance. Georgelin and Georgelin suggested that a four armed spiral pattern gives the best fit to the distribution of HII regions.

The study of the spiral structure from 21 cm line observations has been based on the differential galactic rotation, which is the main cause of broadening of line profiles. In general, radiation from the various spiral arms along a line of sight will be received at different frequencies because the arms will have different apparent radial velocities. These velocity line profiles can be used to find a mean rotation curve *i.e.* the variation of the rotation velocity of gas with galactocentric radius assuming that the motion is all in circular orbits and is axisymmetric. In addition the line profile for a particular direction gives a relationship between brightness temperature and frequency (or velocity). In order to get the distribution of HI over the galactic plane, one has to convert this relationship to the density of HI gas in terms of distance under a certain set of assumptions. In early studies of the distribution of HI gas in the Galaxy, it was assumed that the gas was optically thin with a constant spin temperature and the motion of the gas was in a circular orbit. Burton(1971) found the evidence of non-circular motion of HI gas with deviations from the mean rotation curve of the order of $\pm 10\text{kms}^{-1}$, which is a few percent of the circular rotation velocity. Weaver(1974) looked for the curves and loops in the longitude-velocity diagram of the Berkeley 21 cm survey but still assumed circular rotation. Later studies of density and kinematic variation model had to consider the density wave theory. Simonson(1976) constructed a spiral pattern consisting of two arms with a small pitch angle originating 4 kpc from the galactic centre with a multiple arm structure of larger pitch angle beyond the solar circle.

To study the galactic structure from CO emission line surveys is a relatively new approach but there has been much discussion about their suitability. Cohen et al.(1980) show good evidence of spiral arm structure from CO data. These features also appear in the 21 cm surveys but the CO surveys showed a higher contrast of intensity between arms and interarms than in 21 cm measurements. Cohen et al.(1985) and Grabelsky et al.(1985) studied a similar CO survey made in the fourth quadrant and showed that the Carina arm can be clearly distinguished. Solomon, Sanders and Rivolo(1985) concluded from another CO survey of the north side of the Galaxy that it is only the warm molecular clouds that are the spiral tracers and the cold clouds have a more widespread distribution. We should bear in mind that H₂ and CO prevail in the central and inner parts of our Galaxy but there is mostly HI and very little HII in the outer parts. Robinson et al.(1983) studied CO data in the southern part jointly with the northern part analysed by Cohen et al. The result showed the four-armed spiral pattern. All the spirals fitted to data by Robinson et al. have pitch angles of 11° – 12°. Blitz et al.(1983) reported a result from an analysis of the Weaver-Williams HI survey and northern CO surveys that the four-armed spiral was traced but it is different from the model by Robinson et al.

Broadbent(1989) studied several models of spiral structure of our Galaxy and adjusted it in order to fit with the synchrotron emission at 408 MHz. We will use this model as a starting point and attempt to improve it for our work.

1.4 Dynamics of spiral structure

It was realised that the spiral arms in our Galaxy could not be solid-bodied material arms because of the effects of the observed differential rotation would cause them to wind up into tight spirals within a few revolution periods. Lin and Shu(1964,1966) and Lin, Yuan and Shu(1969) proposed the theory that the

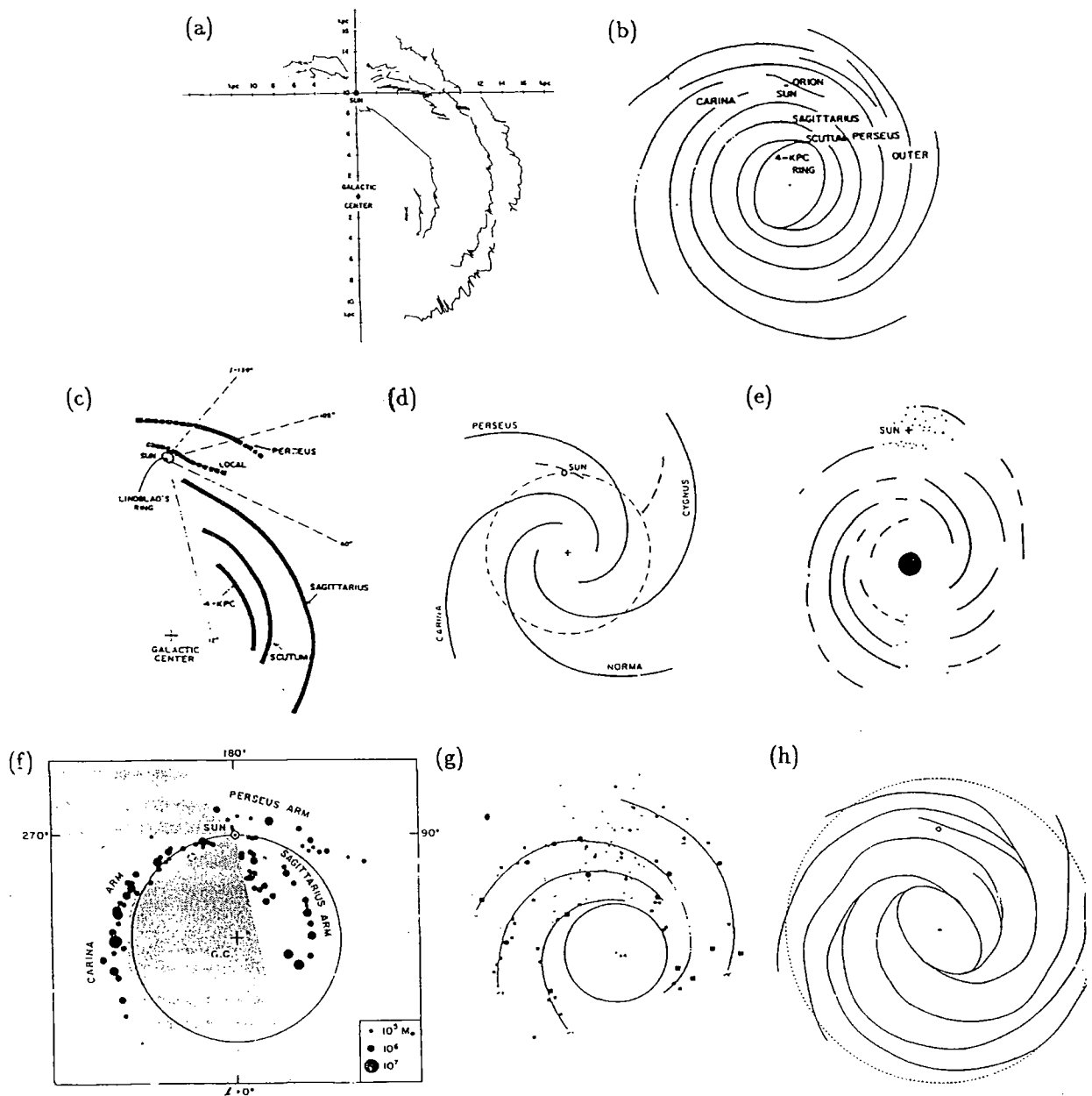


Figure 1.1: The collection of some of spiral structures for the Galaxy that have been deduced from the tracers HI, HII and CO; (a) Weaver(1974) (HI), (b) Simonson(1976) (HI), (c) Cohen et al.(1980) (CO), (d) Blitz et al.(1983) (CO and HI), (e) Robinson et al.(1983) (CO and HI), (f) Cohen et al.(1985) (CO), (g) Georgelin and Georgelin(1976) (HII), (h) Broadbent(1989).

galactic spiral patterns were caused by density waves moving through the galactic disc. They found the spiral perturbations of the gravitational field. By using the rotation curve of Schmidt(1965), it was possible to solve the equations of motion of gas and stars which move across these gravitational perturbations. In order to solve these equations, they assumed that the spirals were tightly wound and there were only small perturbations in the gravitational field which made them able to linearise the equations. The result showed that the gas and stars were found to be spiral density perturbations and by equating this to the initial state the dispersion relation for the density waves was obtained. This dispersion relation predicts that there are two galactocentric radii which are known as the inner and outer Lindblad resonances between which the spiral density waves propagate as a rigid pattern. The inner resonance for an n-armed spiral pattern is at a galactocentric radius, r , such that $\Omega(r) = \Omega_p - \kappa(r)/n$, where $\Omega(r)$ is the orbital angular velocity, Ω_p is the pattern angular velocity and κ is the epicyclic angular velocity. The latter is the velocity with which a particle, suffering a small perturbation from its circular orbit, undergoes small oscillations about the unperturbed orbit. The outer resonance is at r such that $\Omega(r) = \Omega_p + \kappa(r)/n$. Using the Schmidt model of the Galaxy as shown in Fig 1.2, the '4 kpc ring' can be identified with the inner resonance. The co-rotation radius is the galactocentric radius at which the spiral density wave pattern and the stars and gas both rotate at the same angular velocity. It occurs between galactocentric radii of 16 kpc and 18 kpc for a pattern speed of $11-13 \text{ km s}^{-1}\text{kpc}^{-1}$ in a two-armed spiral density wave pattern as shown in Fig 1.3.

However, a spiral pattern produced by the linear theory of density waves would not be very prominent due to an assumption of small perturbations and hence a small density contrast between arm and interarm. It was clear that non-linear solutions of the equations of motion must be used. Roberts(1969) solved the equations by assuming that the gravitational perturbation was only caused by the

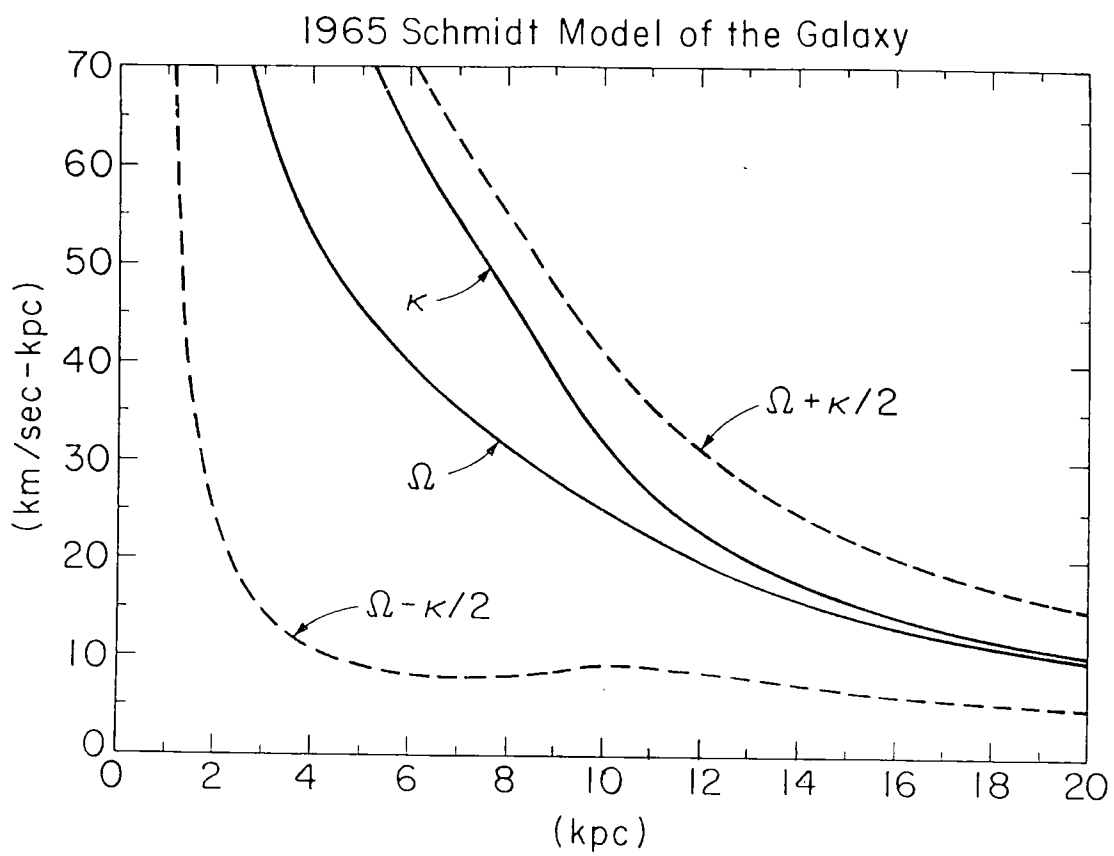


Figure 1.2: Rotation curve of the Galaxy produced by Schmidt(1965)

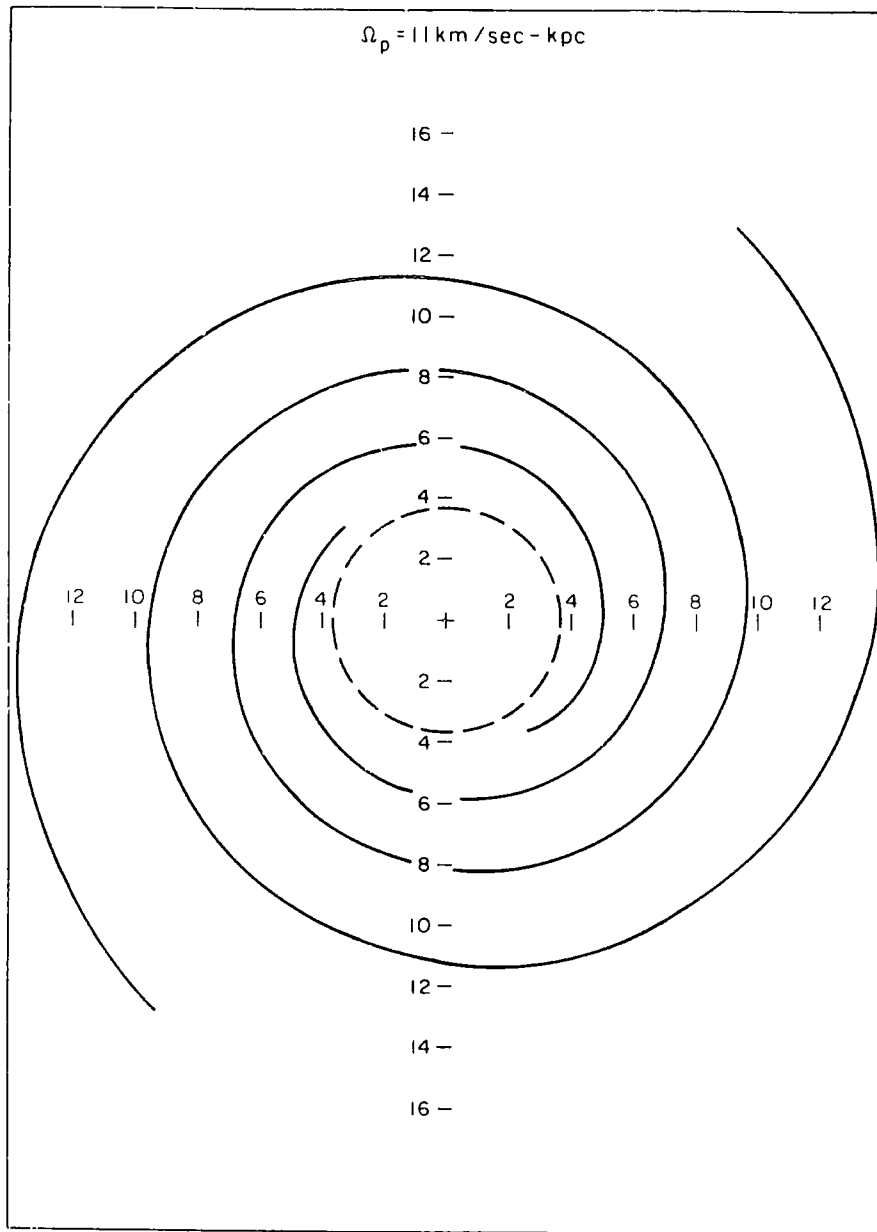


Figure 1.3: Spiral pattern of the Galaxy using Schmidt model (Lin and Shu 1967), for a pattern speed $\Omega_p = 11 \text{ km s}^{-1}\text{kpc}^{-1}$.

stars. Then he solved the hydrodynamic equations for the gas flowing through this spiral field by assuming that gas had only two phases (cool clouds in a warmer intercloud medium). The velocity with respect to the gas of the density wave due to the stars would be higher than the sound velocity in the intercloud medium and the gas should react more violently to the gravitational perturbation. The solutions were obtained in a form in which the gas flowed in closed, nearly concentric stream tubes which contained two periodically located shock waves. He termed this the STS solution (Stream tube band through Two periodically located Shock waves) as shown in Fig 1.4. The complete family of STS solutions gave the composite gas flow over the whole Galaxy, and it was referred to as the Two-Armed Spiral Shock(TASS) pattern. From this work, it was possible to see how narrow, well-defined, spiral arms might be formed. Roberts and Yuan(1970) found that incorporating the magnetic field into the TASS model was possible and the magnetic field direction lay nearly parallel to that of the spiral arms. Gas moving into such shocks would be compressed and also any dust associated with the gas would be concentrated producing dust lanes. As the gas left the shock, it would be quickly decompressed and star formation would stop. One would expect that a region behind the dust lane would exist in which new O and B type stars and their associated HII regions would also be found as shown in Fig 1.5.

It seemed that density wave theory might provide an excellent explanation of the presence of spiral structure in galaxies. However, Toomre(1969) demonstrated that these quasi-stationary state density waves had a tendency to split in half at the co-rotation radius and drift towards the nearest Lindblad resonance, where they were quickly dissipated. In order to maintain the density wave pattern, there must be some source of new waves to take place of those that drift away and disappear. Lin(1970) suggested that mechanisms for spiral arm have invoked the existence of bars in the galactic nucleus. Toomre(1981) suggested that tidal disturbances caused

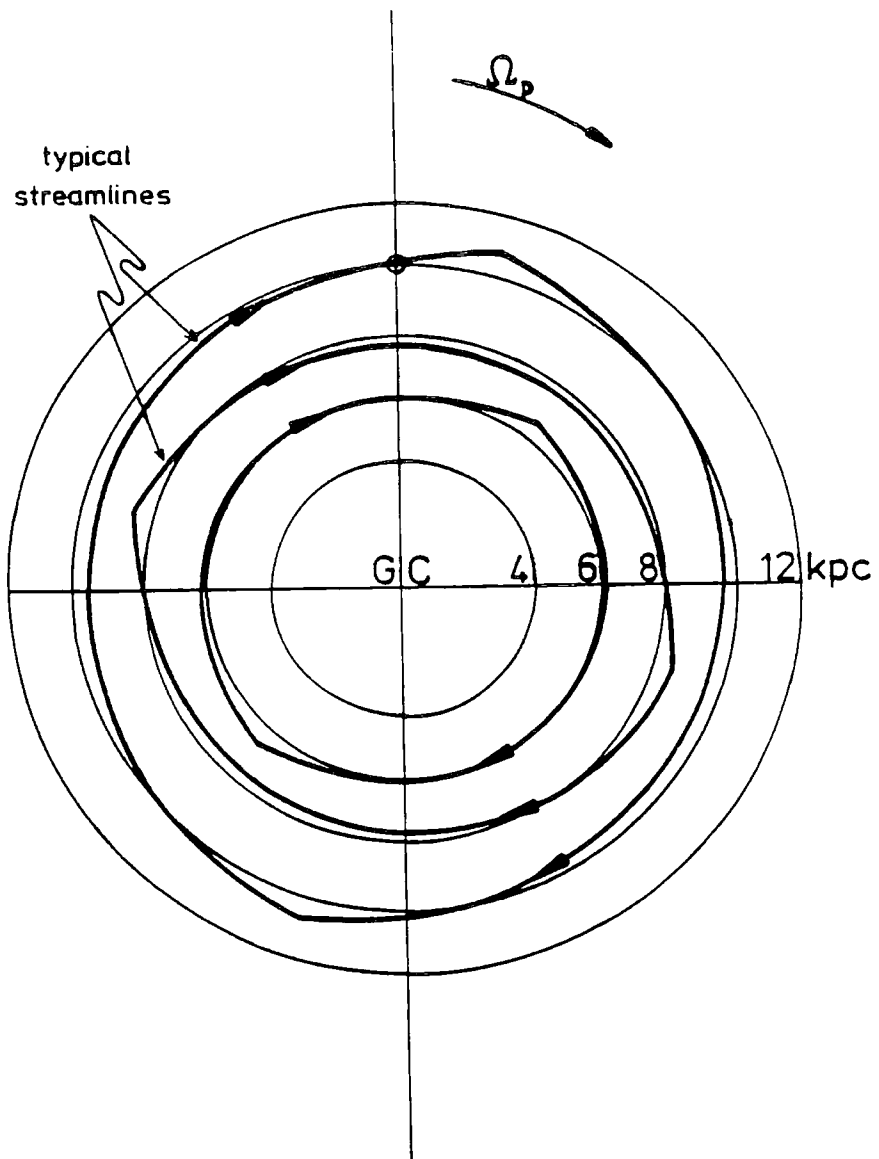


Figure 1.4: STS solution for gas flowing through a spiral density wave. Each streamline appears as a sharp-pointed oval with a sharp turning point at each shock (Robert 1969).

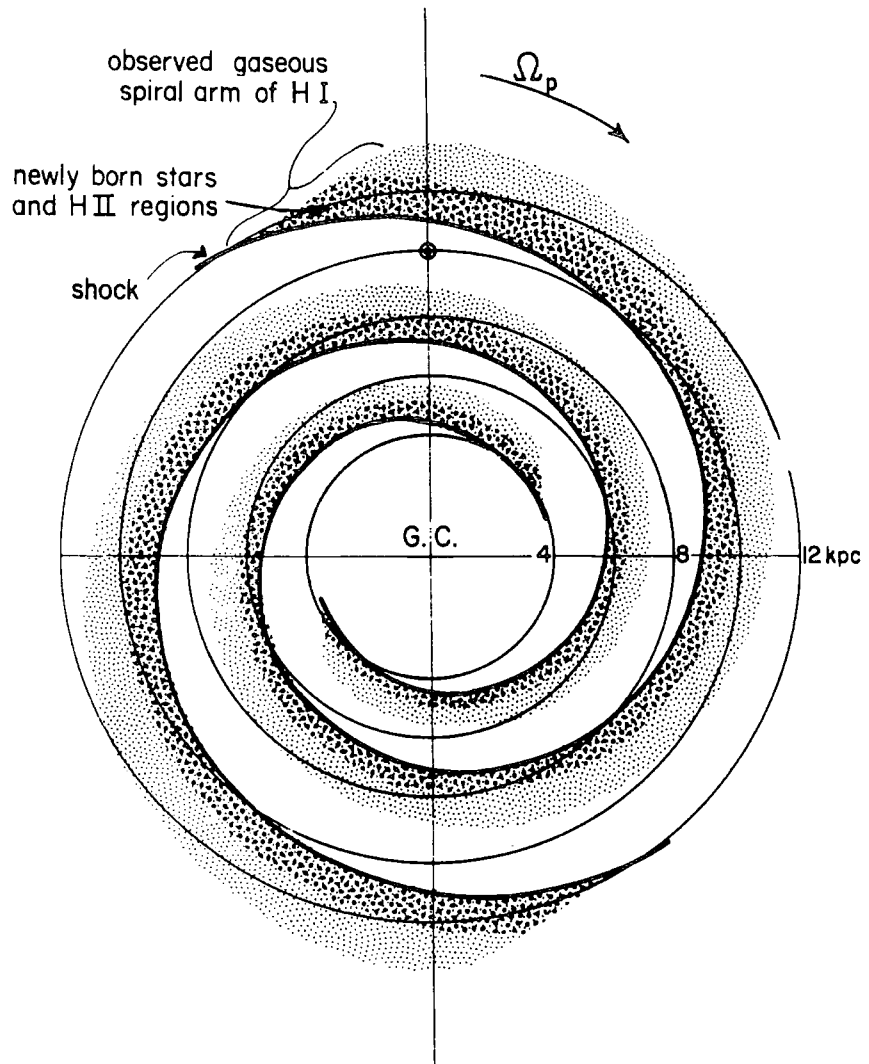


Figure 1.5: Shock and star formation in a spiral galaxy.

by close encounters with nearby galaxies may result in the triggering of spiral density wave patterns. As we shall see there is now evidence for a bar-like structure near to the centre of the Galaxy. Later the idea of spiral arms being formed from shocks in the interstellar medium has been brought into question because of the evidence that interstellar matter had four phases (McKee and Ostriker 1977). Their model has Cool clouds surrounded by inner and outer regions of Warm Neutral and Warm Ionised gas all embedded in a Hot Intercloud Medium. This new model appeared to be incompatible with density wave theory as it was supposed that the hot component had the largest filling factor and therefore would determine the dynamics of gas. However the sound speed in this plasma is too large to form strong shocks on encountering the density wave. Reinhardt and Schmidt-Kaler (1979) suggested that the hot component has a large filling factor only in the spiral arms, the interstellar medium between the arms being in a state capable of supporting density wave shocks. But Schmidt-Kaler and Weigandt (1980) pointed out that the difficulty may not exist if the effective sound velocity is determined largely by the 'warm' rather than the 'hot' component. Another mechanism proposed by Gerola and Seiden (1978) that the spiral arm forming mechanism is 'stochastic self-propagating star formation'. In this process, aggregates of stars are created by the chain reaction mechanism in which shock waves from the supernova explosions of high-mass stars induce the formation of more high-mass stars. The differential rotation of the Galaxy then stretches these strings of stars out into spiral arm features. They also demonstrated that the spiral patterns display correlations between morphological type and rotation curve that are similar to those found in other galaxies (Seiden and Gerola 1979). Although this theory seems to solve the problem of producing a strong shock in three phase ISM, Roberts and Hausman (1984) pointed out that some of the ordered structure evolving from the model may be a consequence of the modelling procedure rather than physical properties and assumed that the dense clouds of the

ISM dictate the dynamics of the medium. They considered each cloud as a particle in a N-body system orbiting the galactic centre and undergoing collisions with other clouds instead of treating the clouds as a fluid. The collisions were assumed to be inelastic and the clouds were effected by an increase in velocity from nearby SNRs. The collisions between clouds is the dominant star formation mechanism and the clouds are concentrated in spiral arms. The model by considering each cloud as a particle could resolve some of the problems of density wave theory. Also the case in which collisions between the clouds dominate seems to produce spiral patterns that persist for at least 10^9 years. The two-armed density wave is the fundamental and predominant one. Shu, Milione and Roberts(1973) suggested that the formation of branches and spurs and features could be the result of nonlinear responses to spiral gravitational perturbation. The simulations using the stochastic self-propagating star formation by Gerola and Seiden are also able to produce multiple arm spiral patterns.

In the next chapter we discuss the theories of thermal and nonthermal emission which are used in our modified model to study the effect of the absorption by thermal electrons at lower frequencies. Earlier models of the distribution of synchrotron emission in the Galaxy (French and Osborne(1976), Brindle et al.(1978), Phillips et al(1981a,b), Beuermann et al(1985)) had relied upon spectral index information in an attempt to separate the thermal and nonthermal components of the radio continuum emission. We describe the new technique of Broadbent et al.(1989) for this separation and its application to the 408 MHz survey. The initial model is based on the 408 MHz all sky survey of Haslam et al.(1982). We give some details of the 408 MHz all sky survey.

In chapter three, we describe in more detail the parameters that are used in the earlier synchrotron model and how we modify those parameters to make them give a better fit with the observational data. In the earlier model, all the parameters

were based on a distance of the Sun from the galactic centre, $R_{\odot} = 10$ kpc but we have changed them to $R_{\odot} = 8.5$ kpc. Therefore all the parameters have been scaled. We have also shown that how we modified our spiral pattern by including the bar in the spiral arm pattern according to the evidence of the asymmetry in the near infrared emission from stars and kinematics of the gas in central bulge(Blitz, 1993). In this model, we consider that the irregular field component undergoes a certain degree of alignment along the arm. This field alignment parameter depends on the compression in the arms but in some other galaxies which are the same class of our galaxy this alignment is not apparent. We discuss why we continue to use this parameter in our model.

At 408 MHz, there is very little absorption of synchrotron emission. But at lower frequencies (34.5 MHz made by Dwarkanath and Shankar(1990), and 29.9 MHz made by Jones and Finlay(1974) have been chosen), the absorption due to thermal electrons becomes important. The thermal electrons in the interstellar medium absorb some of synchrotron emission along the line of sight. We discuss how we can obtain the absorption model in chapter 4. We consider the model of the distribution of thermal electrons which we have developed from H166 α emission of Lockman(1976) and Cersosimo et al.(1989). We have used two models to obtain the distribution; one is according to our synchrotron model and another is based on Georgelin & Georgelin's model(1976) as modified by Taylor and Cordes(1993). We have obtained the absorption model by using our synchrotron model applied to 34.5 MHz and 29.9 MHz together with the absorption due to the distribution of thermal electrons according to the two spiral arms patterns. Also in the chapter 4, we have compared the predictions by using these two models with the surveys at 34.5 and 29.9 MHz.

In chapter 5, we draw conclusions from our model concerning the synchrotron emissivity and consider the separate variation of cosmic ray electron density and

magnetic field strength. We suggest some ways in which such a model as ours might be improved following the acquisition of more observational data.

Chapter 2

Thermal and non-thermal emission

2.1 Synchrotron radiation theory

Synchrotron radiation is emitted by relativistic electrons moving in magnetic fields. An electron with velocity, \mathbf{v} , moving in a magnetic field, \mathbf{H} , has a magnetic force (Fig 2.1)

$$\mathbf{F} = \frac{e\mathbf{v} \times \mathbf{H}}{c} \quad (2.1)$$

The force causes it to move in a helical path around the field lines and produce electromagnetic radiation. If θ is an angle between \mathbf{v} and \mathbf{H} and it has a total energy $E = mc^2/(1 - \frac{v^2}{c^2})^{1/2} = \gamma mc^2$ where γ is the Lorentz factor, it spirals around the field with a frequency

$$\nu_g = \frac{eH_{\perp}}{2\pi\gamma mc} = \frac{\nu_o}{\gamma} \quad (2.2)$$

where $H_{\perp} = H\sin\theta$ is the magnetic field component perpendicular to the electron's path and

$$\nu_o = \frac{eH_{\perp}}{2\pi mc} \quad (2.3)$$

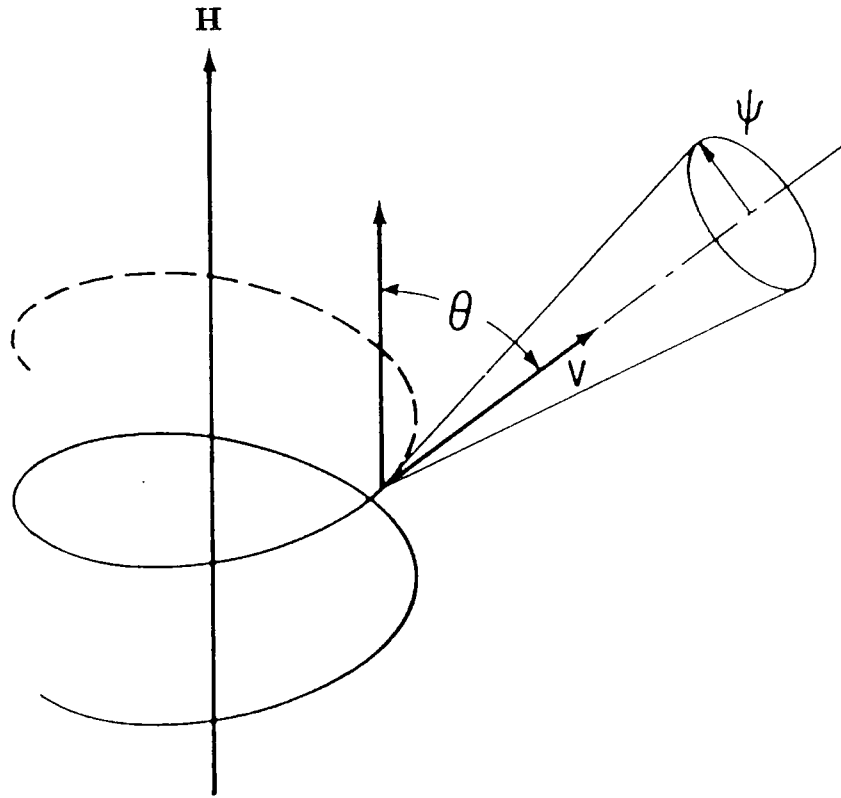


Figure 2.1: Synchrotron radiation from an electron accelerated by a magnetic field.

is the nonrelativistic electron gyrofrequency.

The radiation is concentrated within a narrow cone of angular half-width $\psi = 1/\gamma$. An observer intercepting this narrow beam will detect a pulse of radiation each time the velocity vector sweeps past him, assuming that further away from the direction of electron velocity, the radiation is negligible. The observer will see each pulse at the Doppler-shifted gyration frequency, ν_g' , and all its harmonics, where

$$\nu_g' \sim \frac{\nu_g}{\sin^2 \theta} = \frac{\nu_o}{\gamma \sin^2 \theta} \quad (2.4)$$

and the time interval of each pulse is defined as

$$\Delta t \sim \frac{1}{2\pi\nu_g\gamma^3} = \frac{1}{2\pi\nu_o\gamma^2}. \quad (2.5)$$

Most of the energy will be radiated in harmonics which yield frequencies that are multiples of

$$(2\pi\Delta t)^{-1} \sim \nu_g\gamma^3 = \nu_o\gamma^2. \quad (2.6)$$

For $E \gg mc^2$, the harmonics are so closely spaced that the spectrum is essentially a continuum. The frequency which is near the maximum synchrotron emission is called the critical frequency, ν_c , and is given by

$$\nu_c = \frac{3}{2}\gamma^2\nu_o = \frac{3e}{4\pi mc} H_{\perp} \gamma^2 = 16.08 \times 10^6 H_{\perp} E^2 \quad \text{MHz} \quad (2.7)$$

where E is electron energy in GeV and H is in Gauss.

The power spectrum for the radiating electron is

$$P(\nu) = \frac{\sqrt{3}e^3}{mc^2} H_{\perp} \left[\left(\frac{\nu}{\nu_c} \right) \int_{\nu/\nu_c}^{\infty} K_{5/3}(\xi) d\xi \right] \quad (2.8)$$

where $K_{5/3}(\xi)$ is a modified Bessel function and the shape of the quantity in square brackets is shown in Fig 2.2 .

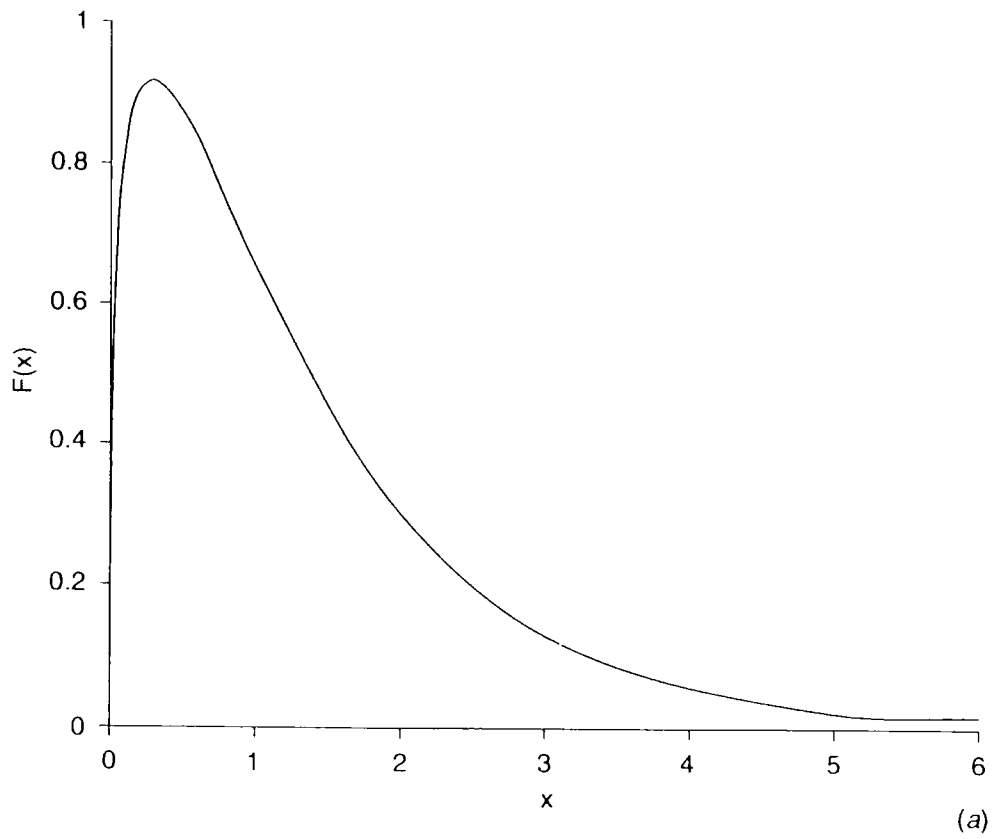


Figure 2.2: The synchrotron spectrum from a single electron as a function of $x = \nu/\nu_c$ where ν_c is the synchrotron critical frequency.

For a power law distribution of the number density of electrons defined by

$$N(E) = N_e E^{-\alpha} dE \quad (2.9)$$

α is the spectral index of the differential energy spectrum of the cosmic ray electrons. and the total emissivity ϵ_ν is

$$\begin{aligned} \epsilon_\nu &= \int_0^{2\pi} \int_0^\infty N(E) P(\nu) dE \\ &= \frac{\sqrt{3}e^3}{4\pi mc^2} H_\perp \int_0^\infty N(E) \frac{\nu}{\nu_c} \int_{\nu/\nu_c}^\infty K_{5/3}(\xi) d\xi \\ &= \frac{\sqrt{3}e^3}{8\pi mc^2} \left(\frac{3e}{4\pi m^3 c^5} \right)^{(\alpha-1)/2} N_e H_\perp^{(\alpha+1)/2} \nu^{-(\alpha-1)/2} a(\alpha) \end{aligned} \quad (2.10)$$

where

$$\begin{aligned} a(\alpha) &= \int_0^\infty x^{(\alpha-1)/2} \int_x^\infty K_{5/3}(\xi) d\xi dx \\ &= \left[\frac{\alpha + 7/3}{\alpha + 1} \right] \Gamma \left[\frac{3\alpha - 1}{12} \right] \Gamma \left[\frac{3\alpha + 7}{12} \right]. \end{aligned}$$

The observed brightness temperature is given by $T_b = c^2 \epsilon_\nu s / 2k\nu^2$. s is the distance along the line of sight.

$$T_b = \frac{\sqrt{3}e^2}{16\pi km} \left[\frac{3e}{4\pi m^3 c^5} \right]^{(\alpha-1)/2} N_e H_\perp^{(\alpha+1)/2} \nu^{-(\alpha+3)/2} \Gamma \left[\frac{3\alpha - 1}{12} \right] \Gamma \left[\frac{3\alpha + 7}{12} \right] \left[\frac{\alpha + 7/3}{\alpha + 1} \right] s \quad (2.11)$$

If α is taken to be 2.6, then

$$\left[\frac{T_b}{\text{K}} \right] = 6.168 \times 10^4 \left[\frac{\nu}{\text{MHz}} \right]^{-2.8} \int_0^s \left[\frac{N_e(s)}{\text{m}^{-2} \text{sr}^{-1} \text{s}^{-1} \text{GeV}^{-1}} \right] \left[\frac{H_\perp(s)}{\mu\text{G}} \right]^{1.8} \left[\frac{ds}{\text{kpc}} \right] \quad (2.12)$$

2.2 Thermal radiation

Thermal radiation is radiation which is caused by interactions between free electrons and positive ions in a partially or fully ionized plasma. It is also known as free-free radiation or bremsstrahlung radiation.

The brightness of the radiation from a blackbody is given by Planck's radiation law,

$$B_\nu(T) = \frac{2h\nu^3}{c^2} \frac{1}{e^{\frac{h\nu}{kT}} - 1}. \quad (2.13)$$

In the region of radio frequencies, $h\nu$ is very small compared to kT ($h\nu \ll kT$), so the factor $(e^{\frac{h\nu}{kT}} - 1)$ is approximately equal to $\frac{h\nu}{kT}$. Therefore

$$B_\nu(T) = \frac{2\nu^2 kT}{c^2} \quad (2.14)$$

Equation(2.14) is the Rayleigh-Jeans radiation law.

If a beam of radiation with intensity I_s passes through an absorbing cloud of thickness L , the intensity of the radiation when leaving the cloud is

$$I = I_s e^{-\tau_\nu} \quad (2.15)$$

where the optical depth $\tau_\nu = \int_0^L \kappa_\nu dx$, κ_ν is the absorption coefficient per unit length in the cloud, and the subscript ν indicates the frequency. If the cloud itself also emits and absorbs radiation, then equation (2.15) becomes

$$I = I_s e^{-\tau_\nu} + I_c (1 - e^{-\tau_\nu}) \quad (2.16)$$

where I_c is the intensity emitted from the cloud. The second term is the contribution to the observed intensity due to emission and absorption by the cloud. If the specific intensity I is expressed as a brightness temperature T , these are related at radio frequencies by the Rayleigh-Jeans approximation,

$$I = \frac{2kT\nu^2}{c^2}. \quad (2.17)$$

Thus expressing intensities as brightness temperatures, we can rewrite equation (2.16) as

$$T_b = T_s e^{-\tau\nu} + T_c (1 - e^{-\tau\nu}). \quad (2.18)$$

The volume emissivity, ϵ_ν , is given by

$$\epsilon_\nu = \frac{n_e}{4\pi} \int P_i(v, \nu) f(v) dv \quad (2.19)$$

where n_e is the electron density, $f(v)$ is the electron velocity distribution and $P_i(v, \nu)dv$ is the total power radiated per unit frequency interval in the collision of an electron of velocity v , with n_i ions,

$$P_i(v, \nu)dv = N_i v Q_r(v, \nu) dv. \quad (2.20)$$

Here the radiation cross section, $Q_r(v, \nu)$, is given by

$$\begin{aligned} Q_r(v, \nu) &= \frac{16}{3} \frac{Z^2 e^6}{m^2 c^3 \nu^2} \int_{b_{min}}^{b_{max}} \frac{db}{b} \\ &= \frac{16}{3} \frac{Z^2 e^6}{m^2 c^3 \nu^2} \ln \left(\frac{b_{max}}{b_{min}} \right). \end{aligned}$$

The logarithmic Gaunt factor, $\ln \left(\frac{b_{max}}{b_{min}} \right)$, depends on the radian frequency, ω , of the bremsstrahlung radiation and the velocity, v , of the electron according to

$$\ln \left(\frac{b_{max}}{b_{min}} \right) = \begin{cases} \ln \left(\frac{\gamma^2 m v^3}{Z e^2 \omega} \right) & \text{for } v < \frac{Z e^2}{h} \text{ and } \omega < \frac{m v^3}{Z e^2} \\ 0 & \text{for } v < \frac{Z e^2}{h} \text{ and } \omega > \frac{m v^3}{Z e^2} \\ \left[\ln \left(\frac{2 \gamma^2 m v^2}{h \omega} \right) - \frac{v^2}{c^2} \right] & \text{for } v > \frac{Z e^2}{h} \text{ and } \omega < \frac{m v^3}{Z e^2} \\ 0 & \text{for } v > \frac{Z e^2}{h} \text{ and } \omega > \frac{m v^3}{Z e^2} \end{cases}$$

where $\gamma = \frac{E}{mc^2}$ does not exceed the order of unity.

The velocity $v = Ze^2/\hbar$ may be related to the temperature $T \approx 3.16 \times 10^5 Z^2$ through the relation $v \approx \left(\frac{kT}{m}\right)^{1/2} \approx 3.89 \times 10^5 T^{1/2}$ and if $f(v)$ is a Maxwellian distribution given by

$$f(v)dv = \left(\frac{2}{\pi}\right)^{1/2} \left(\frac{M}{kT}\right)^{3/2} v^2 \exp\left[-\frac{Mv^2}{2kT}\right] dv \quad (2.21)$$

where M is the mass of the atom then equation(2.19) becomes

$$\epsilon_\nu = \frac{8}{3} \left(\frac{2\pi}{3}\right)^{1/2} \frac{Z^2 e^6}{m^2 c^3} \left(\frac{m}{kT}\right)^{1/2} n_i n_e g(\nu, T) \exp\left(-\frac{h\nu}{kT}\right) d\nu \quad (2.22)$$

where $g(\nu, T)$ is the Gaunt factor

$$\begin{aligned} g(\nu, T) &\approx \frac{\sqrt{3}}{\pi} \ln \left[\left(\frac{2kT}{\delta m}\right)^{3/2} \frac{m}{\pi \delta Z e^2 \nu} \right] \\ &\approx \frac{\sqrt{3}}{\pi} \left[17.7 + \ln \left(\frac{T_e^{3/2}}{\nu}\right) \right] \\ &\approx 1.38 T_e^{0.15} \left(\frac{\nu}{\text{GHz}}\right)^{-0.1} \end{aligned}$$

δ is Euler's constant in the form of $\exp(0.577)$ and T_e is the electron temperature.

The absorption coefficient is given by

$$\kappa_\nu = \frac{\epsilon_\nu c^2}{2h\nu^3} \left[\exp\left(\frac{h\nu}{kT}\right) - 1 \right] \quad (2.23)$$

$$= \left(\frac{n_e n_i}{\nu^2}\right) \left(\frac{8Z^2 e^6}{3\sqrt{3} m^3 c}\right) \left(\frac{\pi}{2}\right)^{1/2} \left(\frac{m}{kT}\right)^{3/2} g(\nu, T). \quad (2.24)$$

For HII regions, an approximation for the absorption coefficient by Altenhoff et al.(1960) is

$$\kappa_\nu \approx \frac{0.08235 n_e^2}{\nu^{2.1} T_e^{1.35}} \quad (2.25)$$

Thus the optical depth is

$$\tau_\nu \approx 0.08235 T_e^{-1.35} \nu^{-2.1} \int n_e^2 ds \quad (2.26)$$

The absorption coefficient for α line emission in local thermodynamic equilibrium is

$$\kappa_L = 1.070 \times 10^7 \Delta n \frac{f_{nn'}}{n} n_e n_i T_e^{-2.5} \exp\left(\frac{E}{kT_e}\right) f(\nu) \quad h\nu < kT_e \quad (2.27)$$

where $f_{nn'}$ is the oscillator strength and E is the energy of the upper quantum level. For hydrogen, $E/kT_e = (1.579 \times 10^6)/n^2 T_e$.

The oscillator strength was suggested by Menzel(1968) as

$$f_{nn'} \cong nM \left(1 + 1.5 \frac{\Delta n}{n}\right) \quad (2.28)$$

where $M = 0.190775, 0.26332, 0.0081056,$ and 0.0034918 for $\Delta n = 1, 2, 3,$ and 4 respectively. The intensity at some frequency within the recombination line is the sum of that in the underlying continuum(I_c) and that from the line(I_L) :

$$\begin{aligned} I &= I_c + I_L \\ &= B_\nu(T_e) [1 - e^{-(\tau_c + \tau_L)}] \end{aligned} \quad (2.29)$$

and the intensity contributed by the line is :

$$I_L = I - I_c = B_\nu(T_e) e^{-\tau_c(1 - e^{-\tau_L})} \quad (2.30)$$

$$\cong B_\nu(T_e) \tau_L \text{ for } \tau_c, \tau_L < 1. \quad (2.31)$$

Under the same conditions, we can write $I_c \cong B_\nu(T_e) \tau_c$ and the ratio of the total energy emitted in the line to that emitted in the underlying continuum is

$$\int_{line} \frac{I_L d\nu}{I_c} = \int \frac{\tau_L d\nu}{\tau_c} \cong \int \frac{\kappa_L d\nu}{\kappa_c}. \quad (2.32)$$

Using equation(2.25) and (2.27) we get

$$\int \frac{I_L d\nu}{I_c} = 1.299 \times 10^5 \Delta n \frac{f_{nn'}}{n} \nu^{2.1} T_e^{-1.15} F \exp \left[\frac{1.579 \times 10^5}{n^2 T_e} \right] \quad (2.33)$$

where $d\nu$ must be in kHz. The factor F accounts for the fraction of the free-free emission due to interactions of He^+ with electrons :

$$F = \left(1 - \frac{N_{\text{He}}}{N_H} \right). \quad (2.34)$$

Observations of radio recombination lines in HII regions have established that N_{He}/N_H is approximately 0.08, which leads to a value for F of 0.92. We can write equation(2.32) in term of temperature(Mezger, 1978) :

$$\begin{aligned} \int \frac{T_L d\nu}{T_c} &= 2.478 \times 10^4 \nu^{2.1} T_e^{-1.15} \\ \left[\frac{\int T_L d\nu}{\text{K} \cdot \text{kHz}} \right] &= 2.478 \times 10^4 \left[\frac{\nu}{\text{GHz}} \right]^{2.1} \left[\frac{T_e}{\text{K}} \right]^{-1.15} \left[\frac{T_c}{\text{K}} \right]. \end{aligned} \quad (2.35)$$

However, the observed brightness temperature is a mixture of thermal and non-thermal radiation,

$$T_b = T_T + AT_N \quad (2.36)$$

where T_T is the thermal contribution, T_N is the non-thermal contribution and A is an absorption factor which depends on the relative disposition of thermal and non-thermal material along the line of sight. In this case, we assume that the thermal and the non-thermal materials are similarly distributed (uniformly mixed), so $A = (1 - e^{-\tau_\nu})/\tau_\nu$. Therefore the observed brightness temperature is

Table 2.1 The four surveys at 408 MHz.

Telescope	Beam width (')	Zone		Reference
		α	δ	
Jodrell 250 feet (Mark I)	48	0^h-12^h Anticenter	$-20^\circ + 60^\circ$	Haslam et al., 1970 MNRAS 147, 405
Effelsberg 100 meter	37	12^h-04^h Northern Sky	$-8^\circ + 48^\circ$	Haslam et al., 1974 A & A Suppl. 13, 359
Parkes 64 meter	51	0^h-24^h Southern Sky	$-90^\circ + 24^\circ$	Haslam et al., 1981 A & A 100, 209
Jodrell 250 feet (Mark IA)	48	0^h-24^h North Polar Cap	$+45^\circ + 90^\circ$	Haslam et al., 1981 A & A 100, 209

$$T_b = T_s e^{-\tau_\nu} + T_e (1 - e^{-\tau_\nu}) + T_N (1 - e^{-\tau_\nu}) / \tau_\nu \quad (2.37)$$

2.3 408 MHz all-sky survey

The basic observational data on which our model of the Galaxy is based is the all-sky survey at 408 MHz. It was the result of four individual surveys. These surveys are summarised in Table 2.1.

All the surveys were made by using the nodding scan technique in which the telescope is fixed in azimuth along the meridian and nods up and down in elevation at a constant rate between the declination limits of the survey. The rotation of the earth provides the Right Ascension coverage. By applying an appropriate offset in

the starting times of the scans from day to day, scan lines were made less than half a beam width apart and each downward scan was crossed by regular upward scans allowing a consistent zero level to be set.

Each of the contributing surveys measured the intensity of the left-hand circular polarised component. The synchrotron emission from a collection of cosmic ray electrons in a given magnetic field is about 70% linearly polarized perpendicular to the direction of the field. The observed radiation is generally less than 10% linearly polarized, however. This is due partly to the superposition of regions of emission in which the field runs in different directions but is mainly due to differential Faraday Rotation of the emission coming from various distances along the line of sight. Although the linearly polarized components of the radio continuum contain information about the magnetic field direction it is very difficult to interpret this from our position in the plane of the Galaxy. Our present model deals only with the total intensity. There is no intrinsic circular polarization in the synchrotron emission so measurements of the left hand circular component are equivalent to total intensity measurements.

The absolute zero levels and brightness temperature scales of the Northern hemisphere surveys were calibrated using the 404 MHz survey of Pauliny-Toth & Shakeshaft (1962). This was an absolutely calibrated survey made of a grid of points with a 7.5 m paraboloid. The grid point temperatures had been measured relative to that of the North celestial pole and the pole temperature was found from a separate series of measurements. The 32° to 40° of Declination overlap between the Parkes and Northern surveys allowed calibration of the former. The data of all the surveys were convolved to the same resolution of 51'. The error of the temperature scale of the final allsky survey is believed to be less than 10 % whilst the absolute zero level has an error of ± 3 K. Positional pointing errors are $\pm 1'$ and are negligible compared with the beam width.

Before the Galactic synchrotron emission can be modelled and fitted to the observations one has to remove extragalactic and thermal contributions. The cosmic background radiation has a temperature of 2.7 K. It is black body radiation and therefore contributes this amount to the Brightness Temperature at 408 MHz. Extragalactic radio sources, unresolved by the survey also provide an isotropic background. Lawson et al. (1987) estimate their contribution as 3.2 K. We have subtracted this total of 5.9 K from the survey values. In the galactic plane this is a rather insignificant contribution but near to the galactic poles where the observed temperature is ~ 20 K it is important.

In contrast the thermal component is important in the plane but contributes little at high latitudes.

2.4 Thermal - nonthermal separation technique

As has been explained in chapter 1 there is a problem near to the galactic plane of distinguishing the thermal and nonthermal components of the radio continuum emission. Because of their different spectra the nonthermal, synchrotron emission dominates at low frequencies while the thermal bremsstrahlung becomes prominent at higher frequencies. The standard method of separation requires accurate absolute measurements of brightness temperature of the continuum emission at high and low frequencies and an a priori knowledge of the spectral index of the nonthermal component.

A new technique has been developed by Broadbent et al.(1989) by using a correlation between the IRAS 60 μm band emission from the galactic disc and the radio continuum emission measured with a similar angular resolution by Reich et al.(1984) at 11 cm and Haynes et al.(1978) at 6 cm. A significant part of the radio continuum emission at these frequencies is from thermal bremsstrahlung and it was known prior to the IRAS survey that discrete HII regions were sources of radio and

infrared continuum emission and that the distribution of far infrared (FIR) emission along the galactic plane was similar in form to the high frequency radio continuum. The surprising fact, first pointed out by Haslam and Osborne(1987), was that the correlation was so detailed. An example of this is shown in Fig. 2.3

It is apparent, however, that there are some discrete radio sources on the top map for which there is no FIR counterpart on the bottom map. The most obvious is the source at $\ell = 34.7^\circ$, $b = -0.4^\circ$. This is the supernova remnant (SNR) W44. There is no reason why a SNR, whose radio brightness is due to synchrotron radiation from enhanced cosmic ray electron density and magnetic field should show any corresponding enhancement in the FIR. A closer examination of the two maps show 12 other discrete sources which are seen only in the radio and these are all catalogued SNRs. This lead to Haslam and Osborne proposing a simple test for distinguishing candidate SNRs from the much more common HII regions on the basis of their much higher radio/FIR brightness ratio. The main part of the nonthermal emission of the galactic disk, however, is the diffuse emission from cosmic ray electrons in the general galactic magnetic field and this should also show no detailed correlation with the FIR emission.

Prior to the IRAS survey it was accepted that the FIR emission from the plane of the Galaxy came from dust heated by starlight. There were discrete sources, identified with individual bright HII regions, and a diffuse component. The latter could be from dust mixed with the ionised gas of the, so-called, extremely low density (ELD) HII regions of Mezger(1978) or from dust grains in molecular clouds heated by invisible O stars within the clouds. As HII regions, resulting from star formation, would be expected to have some spatial correlation with molecular clouds the earlier low resolution surveys were unable to distinguish between the two possibilities. With the 4' resolution of the IRAS survey the close correspondence between the 60 μm band FIR and the 11 cm radio continuum, which has a thermal com-

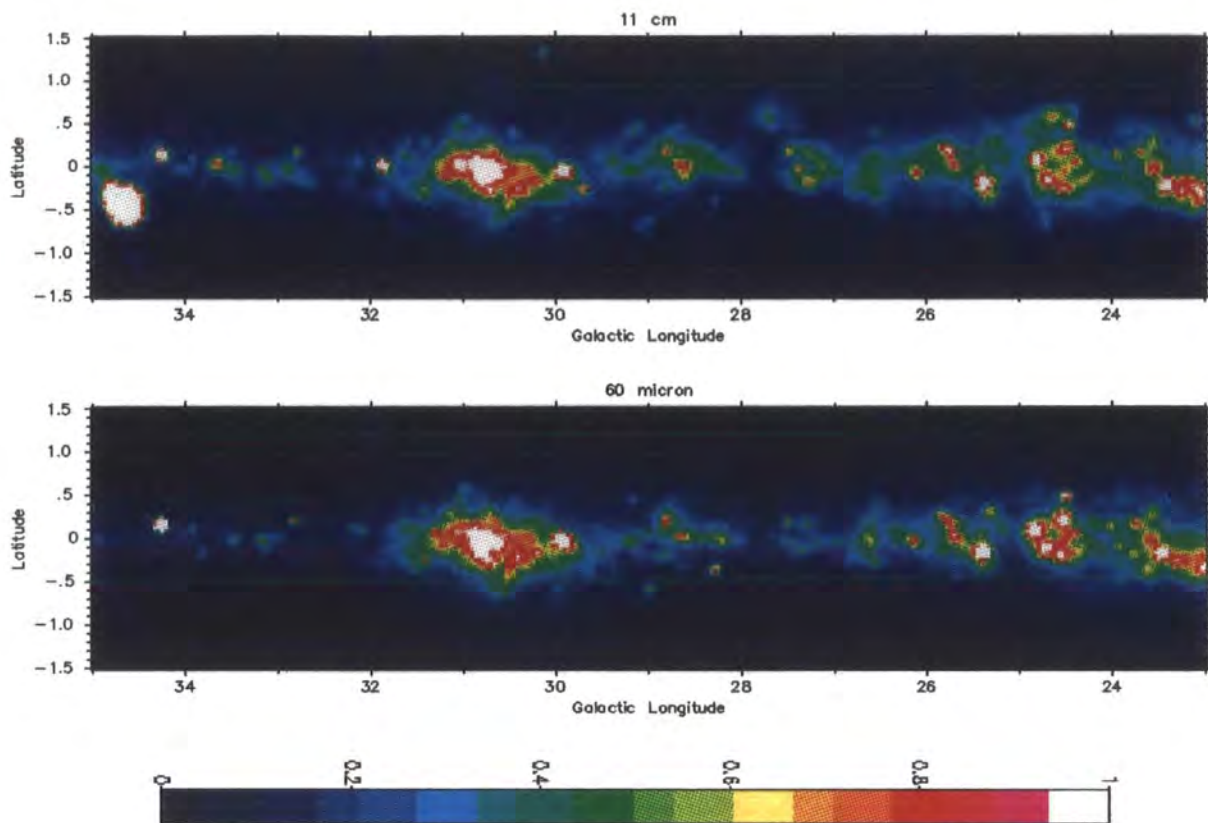


Figure 2.3: Comparison of the distributions of far infrared and radio continuum emission near to the Galactic Plane. The bottom panel shows the $60\ \mu\text{m}$ band emission from the IRAS survey for galactic longitude $35^\circ > \ell > 23^\circ$ and galactic latitude $+1.5^\circ > b > -1.5^\circ$. The colour scale plotted ranges from 0 to $2\ \text{GJy sr}^{-1}$. The maximum intensity is $16\ \text{GJy sr}^{-1}$ at $\ell = 30.8^\circ$, $b = 0^\circ$. The top panel shows the same region as observed at 11 cm wavelength by the Effelsberg radio telescope (Reich et al., 1984). Here the colour scale plotted is from 0 to 10 K in brightness temperature and the maximum is 82.6 K at the same position as the maximum on the infrared map. Both maps have an angular resolution of $4'$. At 11cm the conversion factor from brightness temperature to intensity units is $0.22\ \text{MJy sr}^{-1}\ \text{K}^{-1}$.

ponent from the ELD HII regions, shows that the main part of this FIR must also be from the dust in these regions. Broadbent et al. showed quantitatively that the correlation of the 60 μm FIR and the radio continuum is much stronger than the correlation with the column density of molecular hydrogen as given by the ^{12}CO line emission.

There is also some FIR, but no radio continuum, emission from the dust associated with clouds of neutral atomic hydrogen (HI). At galactic latitudes greater than about 10° , where this is the only FIR component, an empirical relation between the FIR intensity and the hydrogen column density can be established. This gas is local to the sun in terms of galactocentric radius. There is of course HI gas in clouds throughout the plane of the Galaxy. If its FIR emission followed the same relation to column density its contribution to the profile of emission along the galactic plane would follow the dashed line in Fig. 2.4. It is expected however that the emission per HI atom increases with decreasing galactocentric radius. This is partly because the 'metallicity', and hence the ratio of dust to gas, increases. A much larger effect is due to the interstellar radiation field also increasing leading to a higher equilibrium temperature for the HI-associated dust. The lower solid line shows its calculated contribution to the FIR intensity for the model of the interstellar radiation field of Cox et al.(1986). Using the available 21cm surveys of the galactic plane, where the Doppler shift tells the galactocentric radius at which the emitting HI along a given line of sight is located, Broadbent et al. calculated the HI contribution and subtracted it pixel by pixel from the IRAS maps.

It is also necessary to subtract the contribution from dust in the Solar System, i.e. the Zodiacal Light. Here it was assumed as a first approximation that the zodiacal emission is a function only of ecliptic latitude. This function was then determined from the observations at high galactic latitudes, where the zodiacal emission predominates, and applied to the subtraction from the galactic plane maps

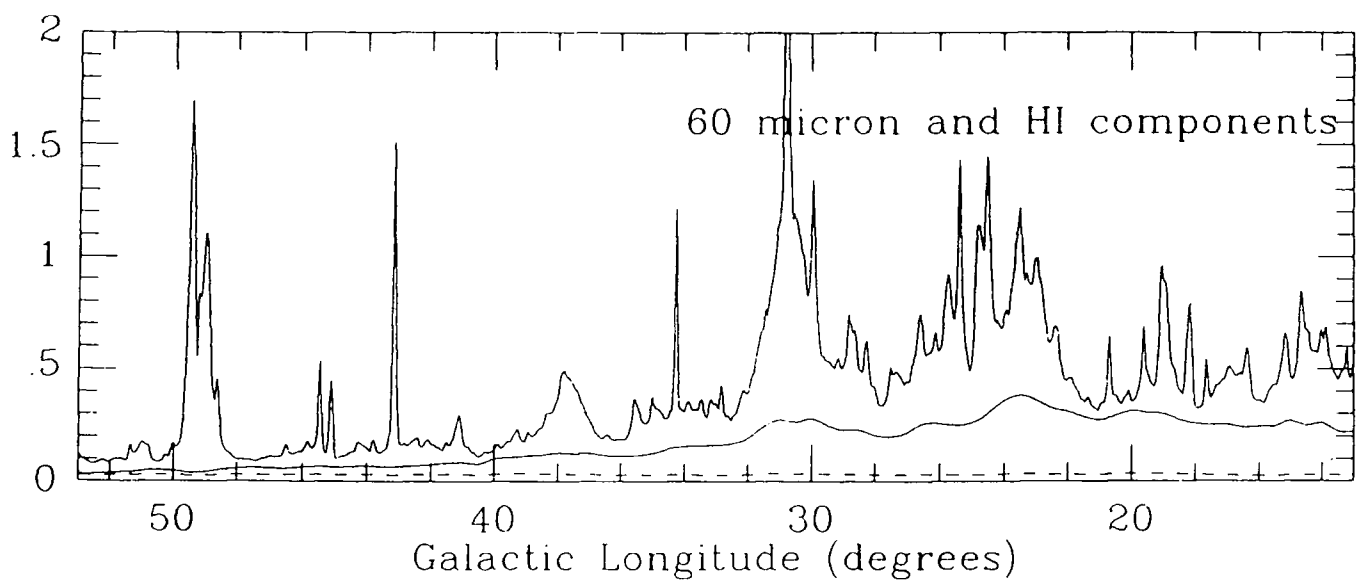


Figure 2.4: Profile of $60\ \mu\text{m}$ IRAS intensity along the galactic plane averaged over $-0.5^\circ < b < +0.5^\circ$. The dashed line shows the contribution of HI-associated dust if it was all at the temperature in the solar neighbourhood. The lower solid line shows the contribution for dust whose variation in temperature with galactocentric radius follows the model of Cox et al.(1986).

where it is generally a minor component. We note that the IRAS team have now released a new set of maps from which the zodiacal emission has been removed according to a multi-parameter model. This is particularly important for studies of the high latitude galactic emission but there may be small changes on a broad scale to some of the galactic plane maps in comparison with the subtraction used here.

Having removed these extraneous contributions the next stage was to find an empirical relation between the radio and FIR emission from the ELD HII regions. This was done by producing scatter plots of the radio versus net FIR emission pixel by pixel for 6° wide sections around the galactic plane, the pixel size being $2.5'$. An example is given in Fig. 2.5. It shows a rather well defined lower envelope to which a straight line could be fitted. The interpretation was that in general a pixel on the radio map would contain both thermal and nonthermal contributions but those points on the lower envelope are from directions where the nonthermal contribution, above a constant background level for that interval of longitude is negligible. The slopes of the lower envelopes were found for the 13 plots of the first quadrant of longitude from the 11cm survey and for the 20 plots from the first and fourth quadrants from the 6cm survey. There was no systematic variation of slope with galactic longitude and the resultant $60 \mu\text{m}$ to 11 cm and $60 \mu\text{m}$ to 6cm intensity ratios were respectively 700 and 810.

The explanation for the correlation between the FIR and the thermal radio emission is that they are both proportional to the recombination rate, r , in the HII regions. For an HII region which is optically thin at frequency ν the emissivity is:

$$\epsilon_\nu(\text{radio}) = 2 \times 10^{-36} T_e^{0.45} \nu^{-0.1} r \quad \text{W cm}^{-3} \text{ Hz}^{-1} \text{ sr}^{-1} \quad (2.38)$$

where T_e is the electron temperature. Most of the Lyman continuum photons involved in the ionization are degraded into $L\alpha$ photons which are absorbed by the dust grains in the HII region and their energy is reradiated in the FIR. There is an enhancement factor, f , termed the infrared excess (IRE) to take account of photons

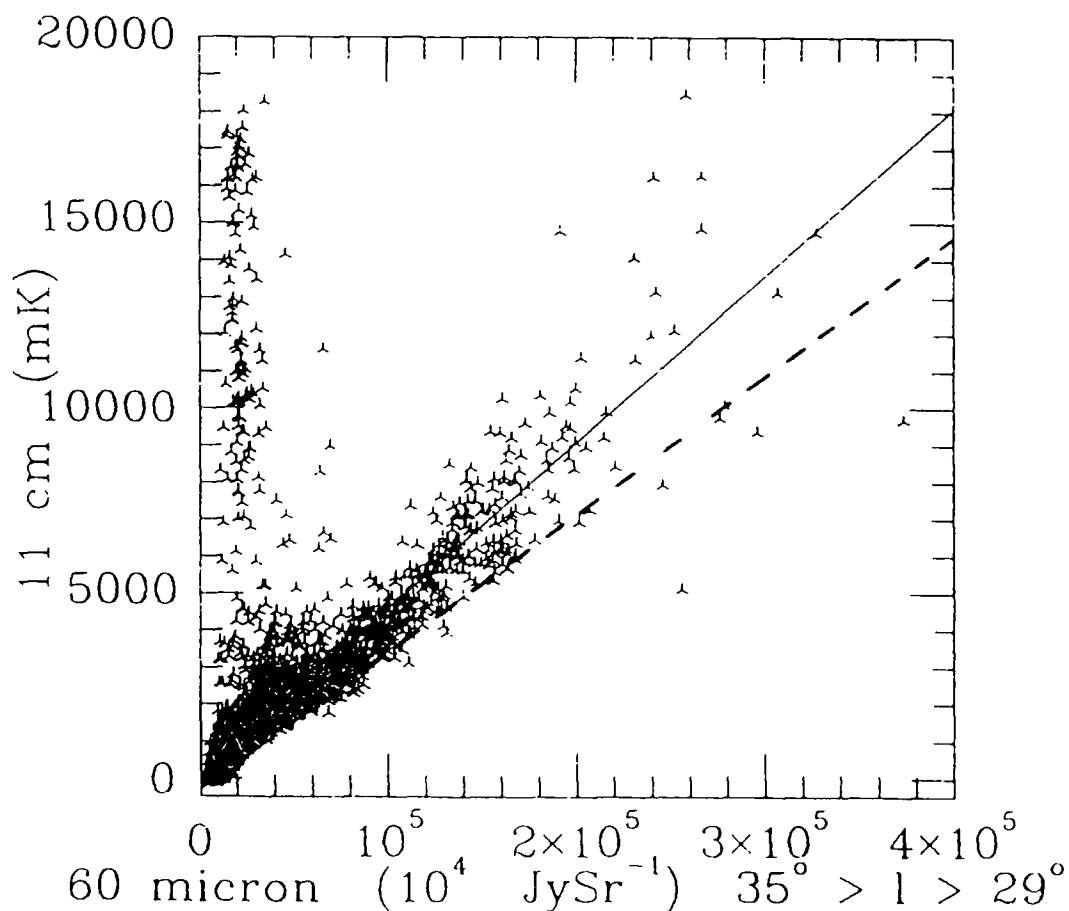


Figure 2.5: Scatter plots of 11 cm brightness temperatures against 60 μm intensities from which the modelled HI-associated component has been subtracted. the region covered is $35^\circ > l > 29^\circ$, $+1.5^\circ > b > -1.5^\circ$, i.e. the left half of the maps of Fig. 2.3. The solid line is the least square fit straight line which has a correlation coefficient 82% but is reduced by points close to the vertical axis due to the bright SNR W44. The dashed line is the fitted lower envelope showing the relation between the thermal component of the radio emission and and the net 60 μm intensity.

of longer and shorter wavelength. The infrared emissivity is therefore

$$\epsilon(\text{IR}) = f r h \nu_{\alpha} / (4\pi) = 1.3 \times 10^{-19} f r \quad \text{W cm}^{-3} \text{sr}^{-1}. \quad (2.39)$$

Using the appropriate emissivity law and grain temperature the emissivity at 60 μm is

$$\epsilon_{\nu}(60\mu\text{m}) = 1.9 \times 10^{-32} f r \quad \text{W cm}^{-3} \text{Hz}^{-1} \text{sr}^{-1} \quad (2.40)$$

With $T_c = 7000$ K the ratio of emissivities is $\epsilon_{\nu}(60\mu\text{m})/\epsilon_{\nu}(11\text{cm}) = 190f$. The implication is therefore that the IRE has a value of 3.7, which is reasonable. The surprising fact is that it appears to be so uniform.

The thermal-nonthermal separation technique was applied to the area within 8° of the galactic plane of the 408 MHz allsky map. The empirical scaling factors were applied to the net 60 μm maps to give the distributions of purely thermal emission at 11cm and 6cm. These were then scaled to 408 MHz using a thermal spectral index of 2.1 which applies to all emitting regions which remain optically thin down to this frequency. This is true except for a few very bright HII regions, for which Shaver and Goss(1970) give directly measured flux densities at 408 MHz. For these the observed flux was used when it was less than those obtained from scaling the FIR emission. Finally the maps were convolved to the 51' resolution of the 408 MHz survey. The results of this are shown as the central maps of Fig. 2.6a and 2.6b. These maps can then be subtracted from the observed maps to give the pure nonthermal emission. Since we are interested in modelling the larger scale distribution of this emission the contributions of all catalogued SNR's within 2° degrees of the galactic plane that are unresolved at 51' have also been subtracted to give the lower maps. The same data are shown as profiles along the galactic plane in Fig. 2.7. One can see that the thermal contribution in the second and third quadrants of galactic longitude is very small except in a few isolated regions.

There are two points to note about the profile for the first and fourth quadrants. First, close to $\ell = 0^\circ$ noncircular motions can lead to wrong values for the

distances of HI clouds so the calculated HI-associated $60 \mu\text{m}$ emission cannot be relied on. Therefore although the estimated thermal contribution to the central peak appears reasonable we do not try to include the region within 5° of the galactic centre in our modelling. Secondly there may still be a few bright HII regions which are not entirely optically thin at 408 MHz and whose contributions are overestimated. If the subtraction of a sharp peak in the thermal component from the observed intensity results in a sharp dip in the nonthermal it is more likely to be due to a problem of optical depth rather than to be a genuine dip.

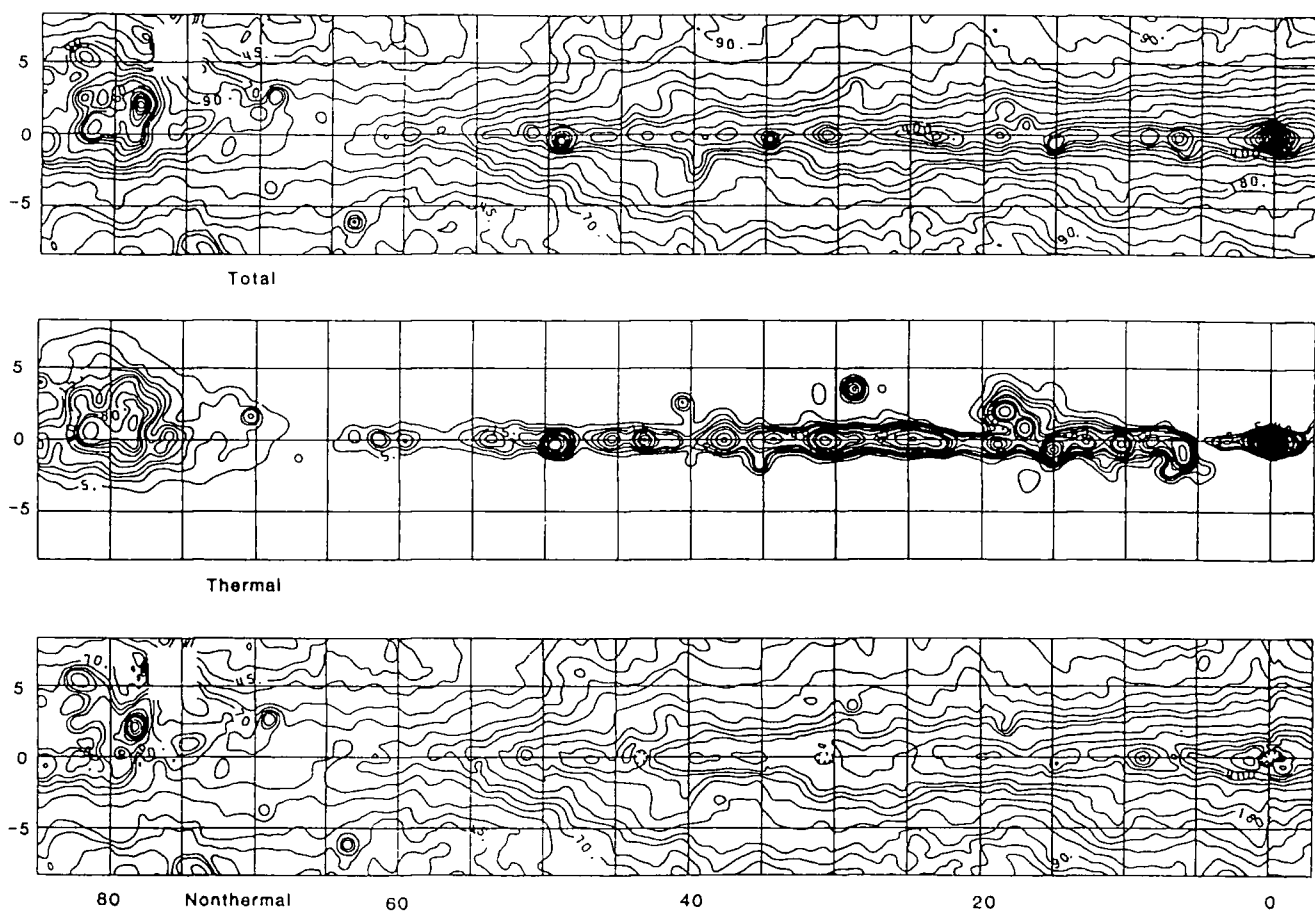


Figure 2.6a: Contour maps of the 408 MHz emission from the galactic disc in the first quadrant of galactic longitude showing thermal non-thermal separation. Upper map: the total brightness temperature observed by Haslam et al.(1982). Middle map: the thermal component deduced from the $60\mu\text{m}$ band IRAS data as detailed in the text. Bottom map: the non-thermal component with known supernova remnants removed. Contour levels for the total and non-thermal maps are from 20 K, by 5 to 50 K, by 10 to 100 K, by 20 to 200 K, by 50 to 400 K, and then by 100 K. Contour levels for thermal map are from 5 K, by 5 to 20 K, by 10 to 60 K, by 20 to 100 K, by 40 to 200 K, and then by 100 K.

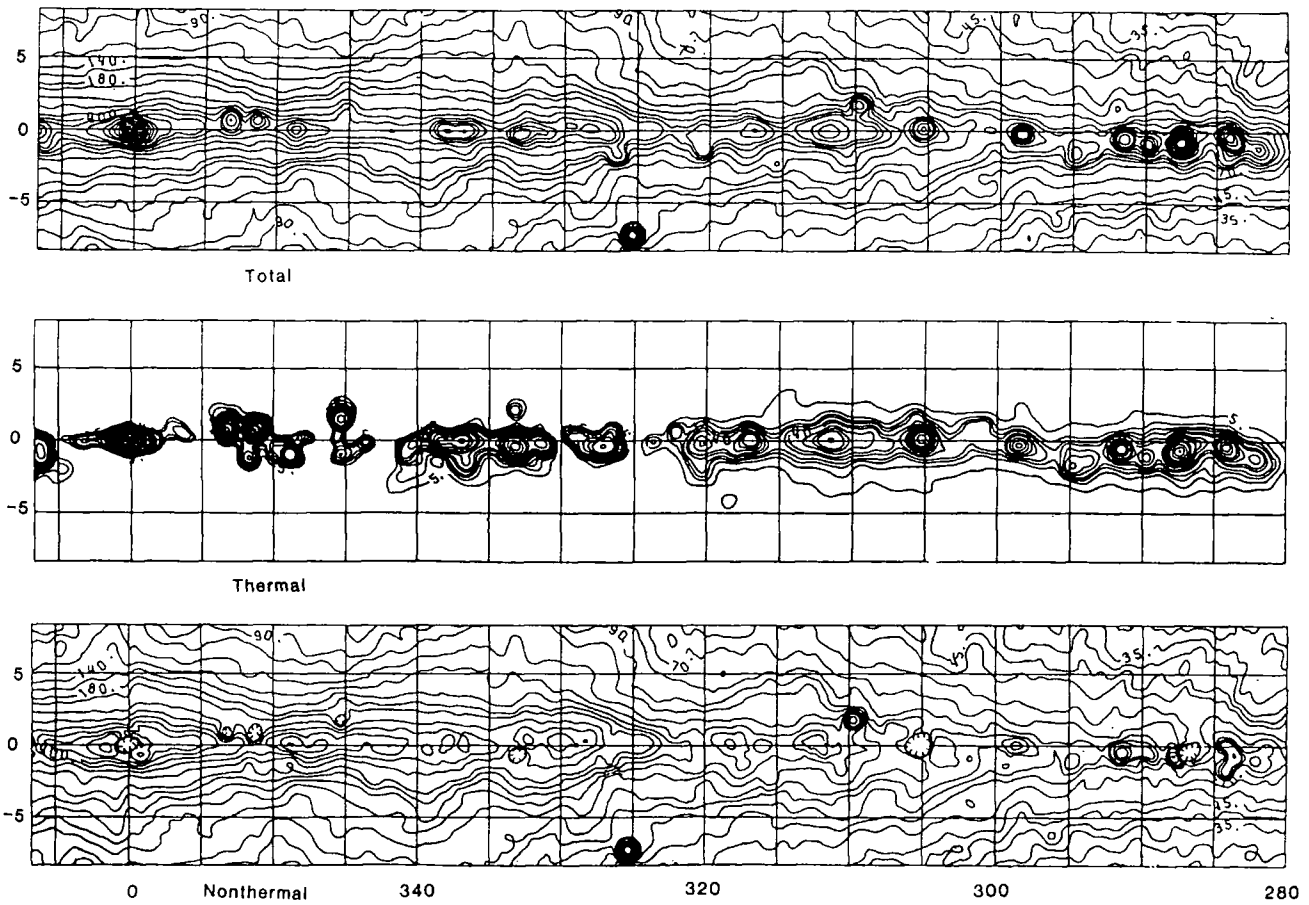


Figure 2.6b: As for Fig. 2.6a but for the fourth quadrant of galactic longitude.

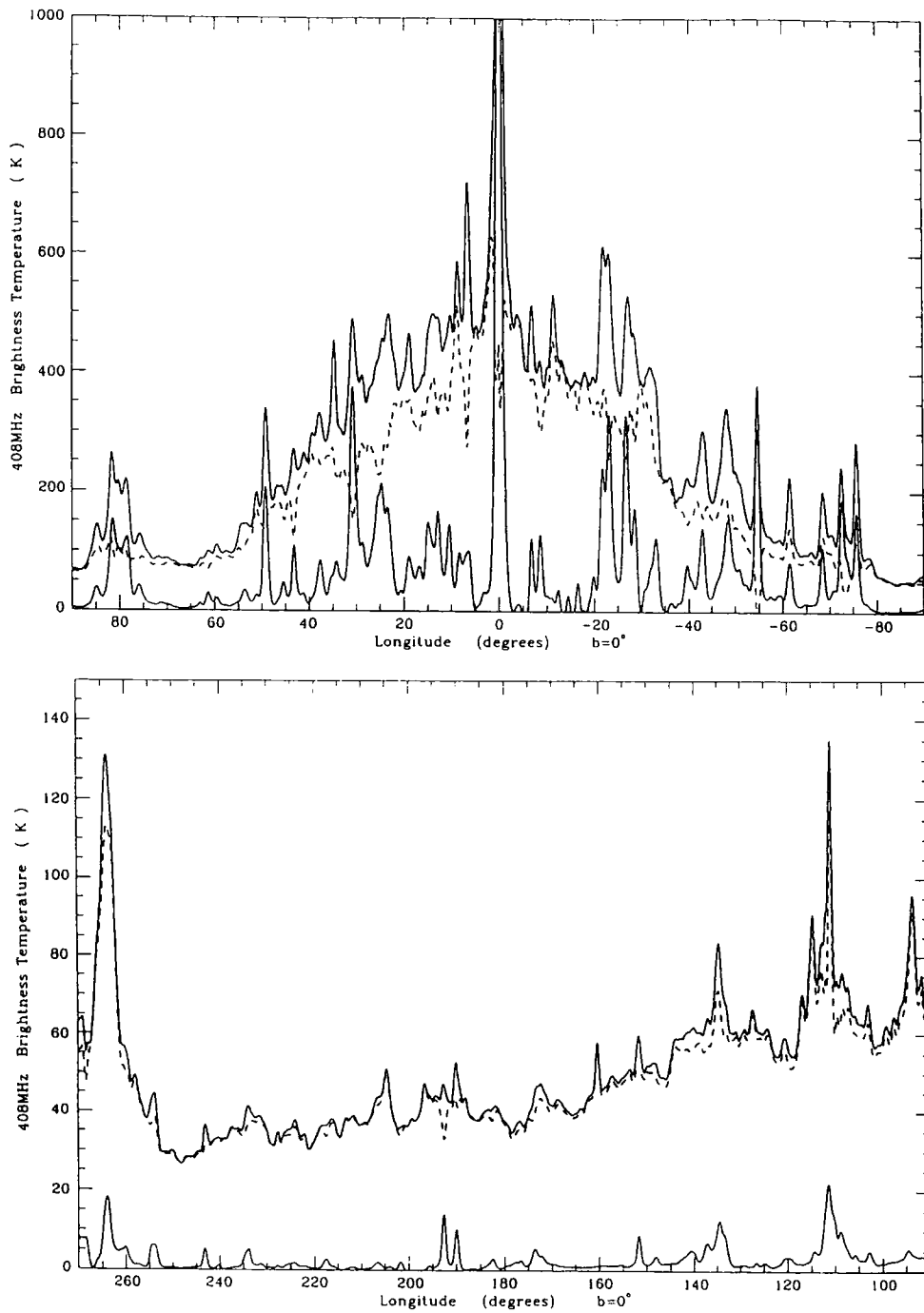


Figure 2.7: The profiles along $b = 0^\circ$ of the 408 MHz emission. Top solid curve: total emission. Dashed curve: non-thermal emission. Lower solid curve: thermal emission.

Chapter 3

Synchrotron emission model

3.1 Introduction

In chapter 2, we have discussed the synchrotron radiation theory and the derivation of the brightness temperature(T_b) along the line of sight at frequency ν . It is given by equation 2.12 :

$$\left[\frac{T_b(\nu)}{\text{K}} \right] = 6.168 \times 10^4 \left[\frac{\nu}{\text{MHz}} \right]^{-2.8} \int_s \left[\frac{N_e(s)}{\text{m}^{-2}\text{sr}^{-1}\text{s}^{-1}\text{GeV}^{-1}} \right] \left[\frac{H_{\perp}(s)}{\mu\text{G}} \right]^{1.8} \left[\frac{ds}{\text{kpc}} \right].$$

From the above equation, we can see that the brightness temperature depends on the electron density $N_e(s)$ and the perpendicular component of the magnetic field $H_{\perp}(s)$ as a function of distance, s , along the line of sight.

As discussed below, the magnetic field can be considered to have two components, a regular component whose direction lies along the spiral arms, parallel to the galactic plane, and an irregular component. It was assumed that the overall distribution of orientation of the latter is isotropic. This means that, to a good approximation, above equation can be rewritten as

$$T_b(\nu) = 6.168 \times 10^4 \nu^{-2.8} \int_s N_e(s) [H_{\perp\text{reg}}(s) + H_{\perp\text{irreg}}(s)]^{1.8} ds \quad (3.1)$$

French(1977) showed that equation 3.1 can be approximately written in the form:

$$T_b(\nu) \approx 6.168 \times 10^4 \nu^{-2.8} \int_s \left(N_e(s) H_{\perp \text{reg}}(s)^{1.8} + N_e(s) H_{\perp \text{irreg}}(s)^{1.8} \right) ds \quad (3.2)$$

In this chapter, we will discuss the parameters which are used for calculating the emission according to this model. Note that all the parameters are now based on a distance of the Sun from the Galactic centre, $R_{\odot} = 8.5\text{kpc}$. All the earlier Durham models including that of Broadbent, which is used as the immediate starting point for the present model, took $R_{\odot} = 10\text{kpc}$ so all lengths have been scaled accordingly.

3.2 The Electron flux density

In equation (3.2) the high energy cosmic ray (CR) electrons, of energy E GeV, which are accelerated by the magnetic field are assumed to have a power law differential intensity spectrum:

$$Flux = N_e(s) E^{-2.6} dE \quad \text{m}^{-2} \text{sr}^{-1} \text{s}^{-1} \quad (3.3)$$

Initially, to simplify the parameterisation, the electron intensity is assumed to have no radial dependence within the plane of the Galaxy. All the variation of emissivity is assigned to the overall radial dependence of the Galactic magnetic field and its modulation by the presence of a spiral arm. In Chapter 5 we consider the independent evidence for a radial gradient in the electron density and its implication for the fitted radial variation of magnetic field strength. We therefore assign the locally measured value to N_e . In the earlier Durham models it was taken that $N_e = 80_{-30}^{+70} \text{m}^{-2} \text{sr}^{-1} \text{s}^{-1} \text{GeV}^{-1}$ from a review by Meyer (1974). Since then there have been increases in the size of the CR electron detectors and in their ability to discriminate against the CR nuclear background, which has about two orders of magnitude higher intensity. A recent measurement was that of Golden et al. (1994) performed in 1989 using a large superconducting magnet spectrometer and

an imaging calorimeter. The results are shown in Fig 3.1 together with those of other experiments published over the previous 10 years. The flattening in the spectrum below 4 GeV is consistent with the effects of solar modulation. For the production of 408 MHz synchrotron radiation equation 2.7 implies that, in a 3 μ G field, the electron energy of interest is around 3 GeV. Taking into account the solar modulation, it can be seen that the above value of N_e still gives a reasonable representation of the local interstellar intensity.

The assumption that the electron flux density does not vary between the arm and interarm regions requires that the electrons diffuse fast compared with the speed of the rotation of the density wave. The density wave takes $\sim 3 \times 10^7$ yr to pass a given point. Measurements of the age of CR nuclei in the galactic disk indicate that they diffuse with a diffusion coefficient $\sim 3 \times 10^{28}$ cm² s⁻¹ and that CR electrons, if they propagate in the same way, therefore diffuse ~ 2 kpc in this time. This is sufficient to move freely from the arm to the interarm region or *vice versa*. Although in the plane the electron flux density is taken to be the same everywhere, out of the plane one would expect there to be a decrease with height above the plane due to diffusive escape of electrons from the Galaxy. In our parameterization of the synchrotron emissivity distribution we assign essentially all of the variation with z , the distance from the Galactic plane to the variation in the electron flux. The exception to this is the decrease in modulation of the magnetic field strength due to compression in the spiral arms with height above the plane.

Phillipps et al. (1981b) in the derivation of a 3-dimensional model of the emissivity distribution by the unfolding technique obtained the following polynomial expression for the z -dependence of N_e

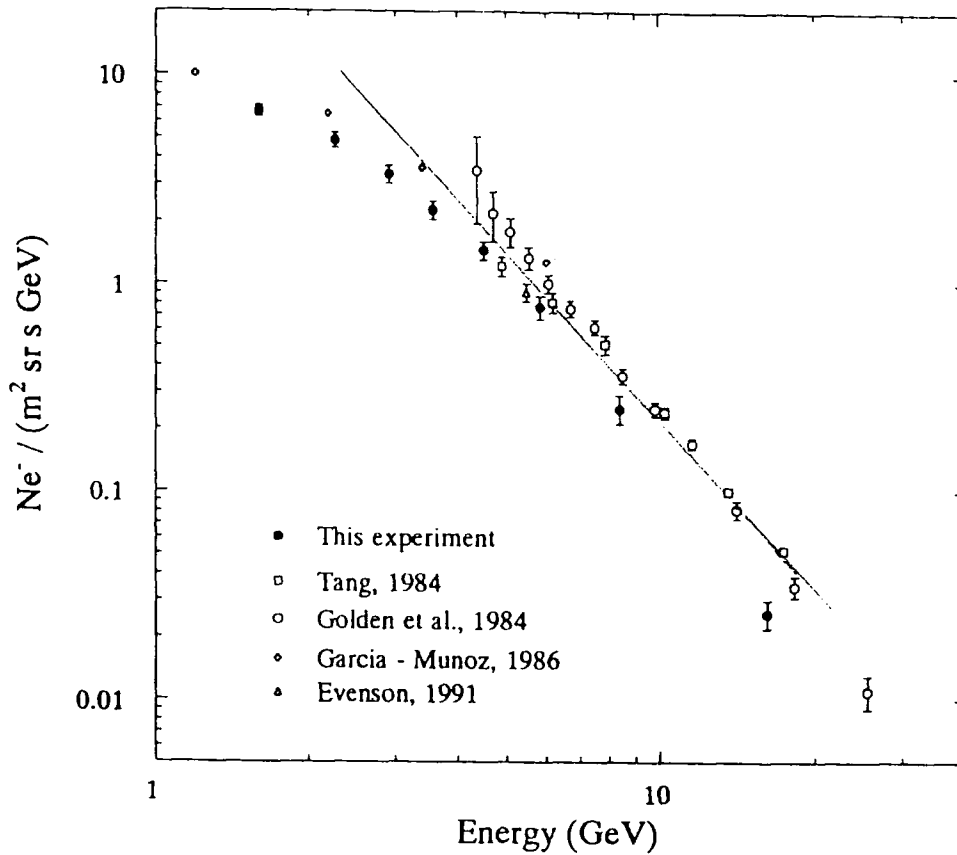


Figure 3.1: A plot of the CR electron intensity at the top of the atmosphere from Golden et al. (1994). The results from experiments over the previous 10 years are also shown. The line shows the spectrum adopted by us for nearby interstellar space, $80_{-30}^{+70} m^{-2} sr^{-1} s^{-1} GeV^{-1}$.

$$N_e \left(\frac{z}{z_0} \right) = 80 \times \begin{cases} 1.063 + 0.9344 \left(\frac{z}{z_0} \right) - 3.551 \left(\frac{z}{z_0} \right)^2 + \\ 2.645 \left(\frac{z}{z_0} \right)^3 - 0.8192 \left(\frac{z}{z_0} \right)^4 + \\ 0.1134 \left(\frac{z}{z_0} \right)^5 - 0.00579 \left(\frac{z}{z_0} \right)^6 & \frac{z}{z_0} \leq 1.1 \\ 0.30788 - 0.01844 \left(\frac{z}{z_0} \right) & 1.1 \leq \frac{z}{z_0} \leq 16.7 \\ 0 & \frac{z}{z_0} \geq 16.7 \end{cases} \quad (3.4)$$

when $R_\odot = 10$ kpc. This represents a 'thick disk' surrounded by an extensive, low emissivity 'halo'. The synchrotron emitting halo does not, however, have the quasi-spherical shape that is normally assumed for the material halo. Such a spherical form would result in higher brightness temperatures at $|b| \sim 45^\circ$ towards the inner part of the Galaxy than is observed. Instead they proposed that the halo and thick disk mirrors the thinner gaseous disk in having a scale height that decreases towards the galactic centre. The above expression therefore contains an R -dependent scaling factor, z_0 , normalised to unity at R_\odot :

$$z_0 = 0.591 - 0.0652R + 0.0106R^2$$

However this polynomial has its maximum value at $z/z_0 = 0.15$ kpc which leads to a small dip in the latitude profile cut at $z = 0$. As we go on to investigate the absorption in the plane at low frequencies it is best to remove this artifact in the model. Thus we have modified this form in order to give a flat top by setting $N_e = 80 \times 1.063$ if $z/z_0 < 0.34105$ as seen in Fig 3.2

This has a significant effect on the fine scale $(1/4)^\circ$ calculation out to $|b| \sim 1^\circ$. For the 408 MHz modelling, Δb was 1° and the data were convolved to 51° HPBW. When this is done with the new model :

1) the reduction in the convolved $\Delta b = 1^\circ$ profile is too small to see at $b = 0$ therefore the fit to the observation is the same (Fig 3.3).

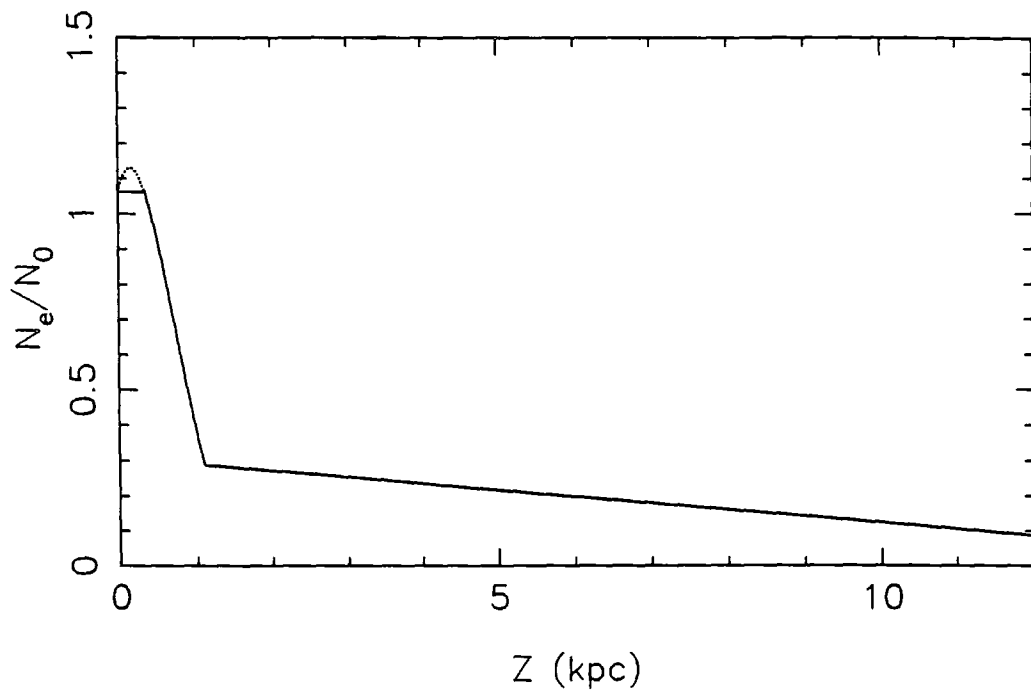


Figure 3.2: The distribution of electron flux density with height above the plane at the solar galactic radius, $R_{\odot} = 10$ kpc. The dot line uses equation 3.4. The solid line shows the modifying form of N_e .

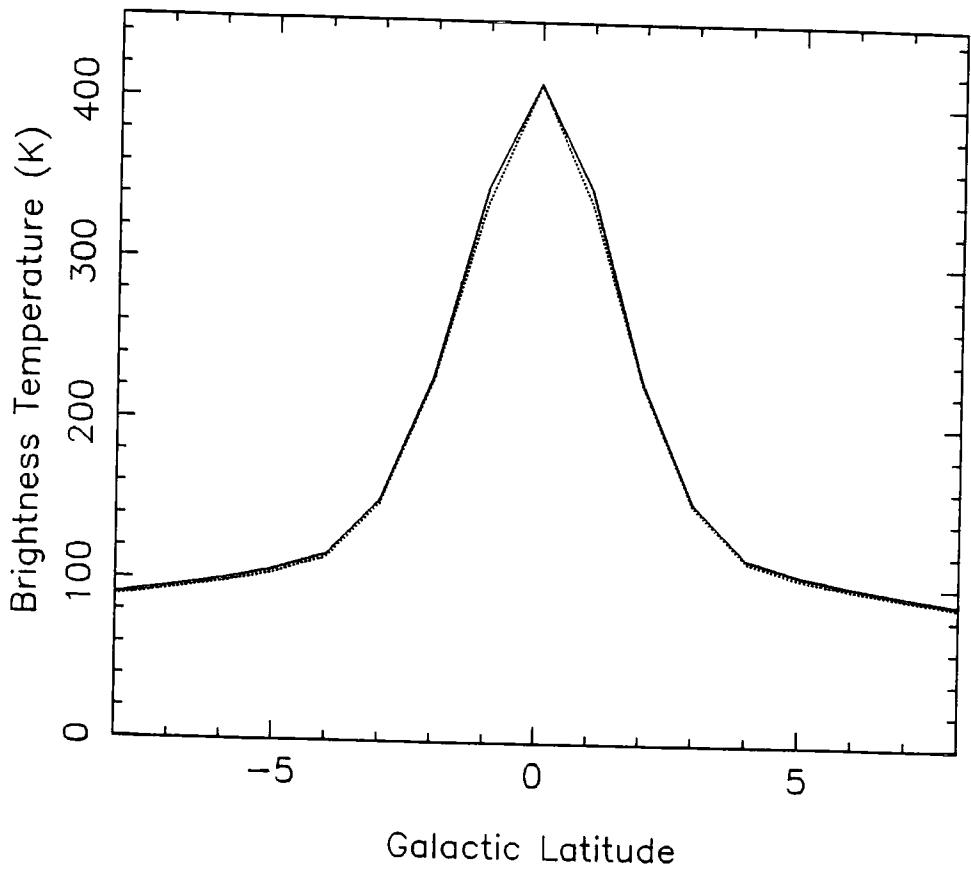


Figure 3.3: The convolved profile of latitude at $l = 0^\circ$, solid line used equation 3.4 and dot line shows the value after modifying the form of N_e (equation 3.5).

2) the changes in the latitude profile are $< 1\%$ so there is no significant change to the latitude cut fits.

The distribution of electron flux density, with this change and the rescaling to $R_{\odot} = 8.5\text{kpc}$ becomes

$$N_e \left(\frac{z}{z_0} \right) = 80 \times \begin{cases} 1.063 & \frac{z}{z_0} \leq 0.2899 \\ 1.063 + 1.099 \left(\frac{z}{z_0} \right) - 4.915 \left(\frac{z}{z_0} \right)^2 + \\ 4.307 \left(\frac{z}{z_0} \right)^3 - 1.569 \left(\frac{z}{z_0} \right)^4 + \\ 0.256 \left(\frac{z}{z_0} \right)^5 - 0.015 \left(\frac{z}{z_0} \right)^6 & 0.2899 \leq \frac{z}{z_0} \leq 0.935 \quad (3.5) \\ 0.30788 - 0.0217 \left(\frac{z}{z_0} \right) & 0.935 \leq \frac{z}{z_0} \leq 14.195 \\ 0 & \frac{z}{z_0} \geq 14.195 \end{cases}$$

where

$$z_0 = 0.591 - 0.0767R + 0.0147R^2$$

3.3 The Galactic magnetic field

3.3.1 Measurements of the field

The first indication of the properties of the galactic magnetic field was obtained from studies of the polarization of starlight. Hiltner (1951) observed correlations on a large angular scale on the sky of the polarization vectors of stars. The polarization is a few percent. This had to be due to the alignment of elongated grains in the interstellar medium. Preferential absorption of the E-vectors of the incident light at visual wavelengths took place parallel to the major-axis of the grains.

The alignment mechanism proposed by Davis and Greenstein was paramagnetic relaxation. The variation in direction of the internal field lags the variation

in direction of the external field producing a torque which tends to align the short axis with the axis of rotation and to make this parallel to H . Thus the grain has its long axis perpendicular to H and the resultant polarization is parallel to the projection on the sky of the magnetic field direction. The polarization of a given star gives the direction of the \perp component averaged along the line of sight. The deduced field strength depends on the assumed magnetic properties of grains so these observations do not give a measure of the magnitude of H . If grains were pure graphite the field strength would need to be $\sim 50\mu\text{G}$ - much higher than obtained by other methods. Ellis and Axon (1978) examined a collected catalogue of stellar polarization data for stars within 2 kpc of the sun and concluded that the field generally pointed towards (or away from) $l \sim 60^\circ$. It was apparent, however, that there were irregularities in the field and that such objects as the North Polar Spur caused perturbations in the field.

A direct method of measuring magnetic fields in objects emitting line radiation is Zeeman Splitting. In magnetic fields of the magnitude of those in the interstellar medium, however, the splitting is very small, $\Delta\nu = 2.8\text{Hz}/\mu\text{G}$. In practice this means that measurements can only be made in the 21 cm line in cold HI clouds and in the 18 cm OH line in molecular clouds. One cannot therefore use this for measuring the general magnetic field. The denser clouds generally have higher fields and if one assumes that the mechanism causing this was the compression of a 'frozen in' field as the cloud contracts one can infer the original value. Trolland and Heiles (1986) extrapolated their observations to an average gas density of 1 atom cm^{-3} and obtained a field strength of $5 \mu\text{G}$.

The best way of measuring the galactic magnetic field is by measuring the Faraday rotation of radio emission from a linearly polarized source. For radiation of wavelength, λ , coming a distance, d , through a plasma of thermal electron density,

$n_e(s)$, the angle of rotation, θ , of its polarization vector is

$$(\theta/\text{radians}) = 0.81(\lambda/\text{m})^2 \int_0^d (n_e(s)/\text{cm}^{-3} H_{\parallel}(s)/\mu\text{G}) (ds/\text{pc})$$

By making measurements at a number of wavelengths one obtains the Rotation Measure,

$$\text{RM} = \theta/\lambda^2 = 0.81 \int_0^d n_e H_{\parallel} ds$$

The first measurements were of radio galaxies and a large number of these have now been measured (e.g. Simard-Normandin and Kronberg, 1980). The interpretation is difficult for low galactic latitudes, however, because of the integrated effect of varying fields over long path lengths to the 'edge' of the Galaxy and the uncertainty in $n_e(s)$ over this distance.

The measurement of the RMs of pulsars is more informative, however, as one can also find the Dispersion Measure, DM, from the variation of arrival time of the pulse with frequency. This is directly related to $n_e(s)$ by $\text{DM} = \int_0^d n_e(s) ds \text{ cm}^{-3} \text{ pc}$. Therefore $\langle H_{\parallel} \rangle = 1.232 \text{ RM/DM}$ gives the weighted mean field independent of any assumptions concerning n_e . A model of the distribution of n_e in the Galaxy such as that of Taylor and Cordes(1993), discussed in Chapter 4 allows an estimate of the distance over which the mean has been taken.

An early analysis of pulsar RMs was performed by Manchester (1974). He made a least squares fit of longitudinal field for those within 2 kpc of the sun and obtained a direction towards $l = 90^\circ \pm 11^\circ$ and $H = 2.2 \pm 0.4 \mu\text{G}$. Later studies have added more pulsars out to greater distances and have obtained evidence for a reversal of field direction in the next inner spiral arm of the Galaxy. The interpretation is complicated, however, by the clear indication that there is a strong irregular component to the field. The most recent work is by Chi and Wolfendale (1990), who have concentrated on obtaining the 'local' field within 1.5 kpc of the sun. For the interarm region, where the sun is located, between the inner Sagittarius arm and the outer Orion Spur they obtain a field strength for the regular component

of $H_{\text{reg}} = 3.2 \pm 1.0 \mu\text{G}$ directed towards $l = 57 \pm 14^\circ$. We adopt this value, i.e. $H_{\text{reg}\odot} = 3.2 \mu\text{G}$. As we see later the direction is also in agreement with our spiral arm model.

All the above observations indicate a substantial irregular component of the magnetic field. A number of different analyses indicate $B_{\text{irreg}} \sim B_{\text{reg}}$ with a typical scale size of 50 to 100 pc. The ratio between the magnitudes of the regular and irregular components of the field is an important parameter when considering how the distribution of synchrotron emission appears from our viewing point within the galactic disk. For a given overall radial variation of the magnetic field strength the contribution of the regular field to the total emissivity will be more strongly peaked towards small galactic longitudes than that of the irregular field because the regular field will be running more nearly perpendicular to the line of sight there. The spiral arms, however, will be much more apparent in the irregular component's emission. The line of sight through an arm reaches a maximum near to the tangential point where the perpendicular component of the regular field will be at a minimum. We have therefore to regard the ratio, F , of regular to irregular field strength as a free parameter of the model.

3.3.2 Alignment of magnetic field in the arms

We assume that the ratio of the regular and irregular field, F , is constant over the Galaxy in the interarm regions but in the arms one would expect it to change. In the absence of any other effects one would expect the irregular component to undergo a certain degree of alignment along the direction of the arm, the extent of which depends on the compression in the arm. French calculated the effective component of the regular field perpendicular to the line of sight in terms of the regular component, the compression ratio and the ratio, F , of the regular to irregular field in the uncompressed state. The equation(3.2) then becomes :

$$T_b(\nu) = 6.168 \times 10^4 \nu^{-2.8} \int_s \left(N_e(s) [\rho_c(s) H_{\text{reg}}(s) \sin\theta]^{1.8} + 0.6861 N_e(s) \left[\frac{\rho_c(s) H_{\text{reg}}(s)}{F} \right]^{1.8} Y(s) \right) ds \quad (3.6)$$

where

$$Y(s) = 1 - 0.477 \left(\frac{\rho_c^2 - 1}{\rho_c^2} \right) \cos^2\theta. \quad (3.7)$$

and ρ_c is the ratio of the density of the gas at a certain point to the density that it would have in the uncompressed state. It has been assumed that the variation of H_{reg} is independent of z and all variations in that direction are included in the electron density and the demodulation of the compression factor, ρ_c , in a spiral arm.

3.3.3 Gas compression factor in spiral arms

The Two-armed Spiral Shock model had a definite prediction for the compression profile across the spiral arm with a sharp rise of density on the inner edge followed by an exponential fall. For example at the solar radius the compression factor could be represented by $\rho_c = 4.1 \exp(-13.7a/A) + 0.7$ where A is the radial separation between the two arms adjacent to the point being considered and a is the distance from the inner arm. When such a compression profile was applied to the early model of Brindle et al. (1978) the predicted peaks at the tangential points of the arms were much sharper than in the observed profile. As pointed out in Chapter 1, further developments in the understanding of the state of the interstellar medium now cast considerable doubt on this model.

As an alternative Roberts and Hausman(1984) assumed that each cloud was a particle in a N-body system orbiting the galactic centre and undergoing inelastic collisions with other clouds. The collisions between the clouds is assumed to be the dominant star formation mechanism. Modelling shows that galaxy-wide shocks formed and the clouds became concentrated in spiral arms. Broadbent calculated

the Gaussian function to fit with the profile of the variation of number density of clouds with spiral phase at a galactocentric radius of 8 kpc as shown in Fig 3.4 by assuming that the width of the arm is the number of degrees between the first points either side of the peak where the density is equal to the average cloud density and taking this to be equivalent to 1 kpc in distance. The Gaussian function has a peak value of 2.5, implying that the maximum compression is 3.5:1, and $\sigma = 0.207\text{kpc}$. Hence, ρ_c after rescaling to $R_\odot = 8.5\text{kpc}$ can be written in the form:

$$\rho_c = CRf(z)\exp(-0.5a^2/0.031) + 1 \quad (3.8)$$

where a is the distance to the nearest arm, inner or outer.

$$CR = \begin{cases} 2.5 & R \leq 8.5\text{kpc} \\ (12.75 - R)0.5 & 12.75 \geq R \geq 8.5\text{kpc} \end{cases} \quad (3.9)$$

The term, $f(z)$, accounts for the variation of compression of the field with distance, z from the plane. The magnetic field increases the effective square dispersion speed of the gas and damps down the compression in the density waves, i.e. the forcing mechanism for the density wave has to overcome an extra pressure. If, as the latitude variation of the synchrotron radiation indicates, the scale height of the magnetic field is considerably greater than that of the gas, the damping effect of the field on the compression will increase rapidly with z . The result of a simple calculation of this effect, due to Brindle et al. (1978), which does not pretend to be an accurate quantitative description is as follows. If one assumes that the magnetic field, the sound speed, C_s , and the velocity of entry into the shock, U are all constant for heights above the plane up to several hundred parsecs the strength of the shock is given by

$$\{[(5V_A^2 + 6C_s^2 + 2U^2)^2 + 32U^2V_A^2]^{1/2} - (5V_A^2 + 6C_s^2 + 2U^2)\}/2V_A^2$$

The Alfvén velocity, V_A , increases with z and the gas density decreases. Taking $H = 3\mu\text{G}$ for the uncompressed field, $U = 35 \text{ km s}^{-1}$, $C_s = 7 \text{ km s}^{-1}$ and the variation of gas density of Schmidt(1956), the compression will be reduced to a half at $z = 200\text{pc}$ and is essentially zero beyond 425 pc . For ease of calculation the following polynomial has been fitted to $f(z)$, the damping factor by which the compression in the plane should be multiplied

$$f(z) = \begin{cases} 1 + 0.908z - 23.529z^2 + 37.35z^3 & z \leq 0.425\text{kpc} \\ 0 & z \geq 0.425\text{kpc} \end{cases} \quad (3.10)$$

The calculations of synchrotron emission based on expressions 3.8, 3.9 and 3.10 for ρ_c gives a better fit to the observational data at 408 MHz compared to the earlier parameterisation.

3.3.4 Large-scale radial variation of magnetic field

It is believed that the galactic magnetic field is generated by dynamo action due to a combination of differential rotation and cyclonic motion in the same way that the magnetic fields of stars and planetary bodies are generated. The galactic dynamo theory is not sufficiently advanced to be able to predict details but it is likely that the radial variation of field strength will be such that it rises to a peak within a few kpc of the galactic centre and then falls as $\exp(-R^2)$.

In the Kearsley (1983) model the following equation was used(for $R_0 = 10\text{kpc}$):

$$H_{\text{reg}}(R) = H_0 \left(1 - \exp\left(\frac{-R^2}{4}\right) \right) \exp\left(-\left(\frac{R^2}{R_0^2}\right)\right) \quad (3.11)$$

where R_0 is a free parameter and H_0 is a constant which gives the observed field strength at the position of the Sun. Therefore it is necessary to fix the value F and R_0 by means of a normalization procedure. Two points along the galactic plane

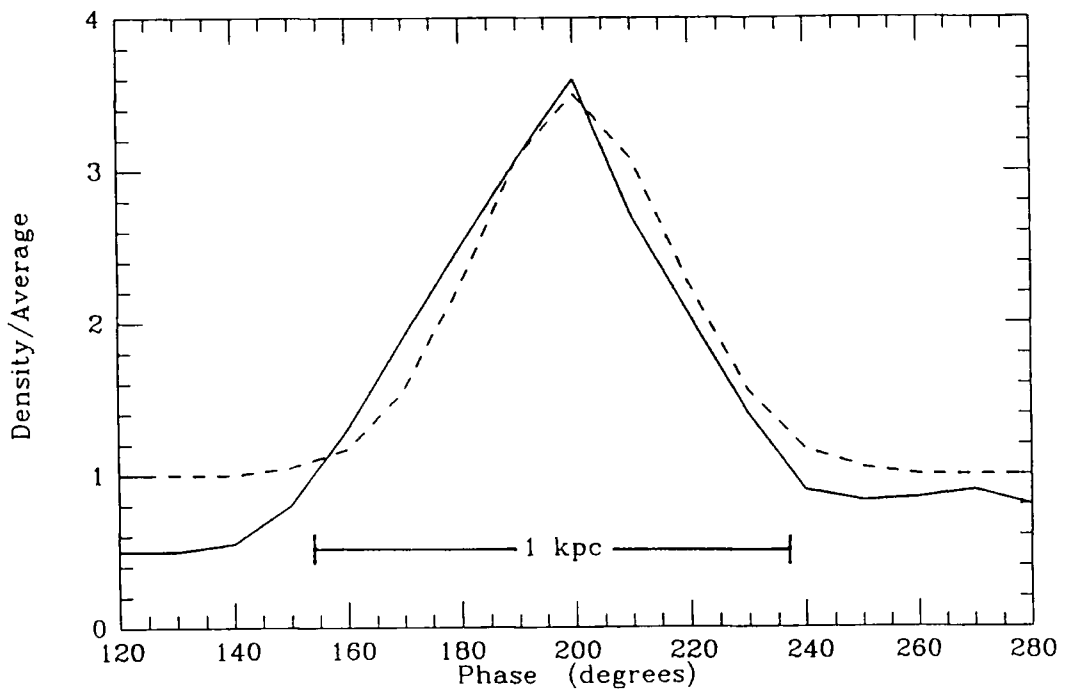


Figure 3.4: The solid line shows the variation of gas cloud density with phase across a spiral arm at 8 kpc by Roberts and Hausman(1984). The density of clouds is expressed relative to the average and marked underneath the curve is the full width of the arm amounting to the linear distance of 1 kpc. The dash line is a Gaussian fit and has $\sigma = 0.207\text{kpc}$.

were chosen, one is at $l = 180^\circ$ and the other is near the galactic centre but not at an emission peak otherwise it would depend on the chosen model of the variation of the compression across the arm much more than on the variation of quantities on a Galaxy-wide scale. R_0 and F are not calculated directly but via the value R_0^2 and $\text{RATIO} = F^{1.8}/0.6861$. At both longitudes, for a given value of R_0^2 , we found the value of RATIO to produce the exact observed temperature. Thus two curves can be drawn of RATIO vs R_0^2 , one for each longitude. The values at which these two lines cross are the values which give the exact observed temperatures at both longitudes and will produce normalized temperatures for other positions in the sky.

From the above equation, we can see that the radial decrease in the uncompressed field was constructed to fall off as $\exp(-R^2/R_0^2)$ at large R and this also gives a zero magnitude at the centre. This model failed to fit the observational data at longitude range $20^\circ < l < 330^\circ$. so it had been suggested that the variation should be much steeper towards the centre of the Galaxy. Thus, the form of the radial variation for $R_0 = 8.5\text{kpc}$ became :

$$H_{\text{reg}}(R) = H_0(1 - \exp(-2.768R^2))\left(\exp - \left(\frac{R}{R_0}\right)^2 + \exp - \left(\frac{R}{R_1}\right)^4\right) \quad (3.12)$$

The additional term, $\exp(-(R/R_1)^4)$ was introduced to make the field fall off more rapidly compared with the earlier one. This new form has a much higher and sharper peak, as seen in Fig 3.5. From the figure, the two distributions behave the same way beyond about 3.8 kpc.

This new form has another free parameter, R_1 . Therefore a new method of normalizing the predictions has been adopted to get all three parameters, R_1 , R_0 and RATIO . This has been renormalised by setting $R_0 = 11.2\text{kpc}$ (taken from the Kearsy model) for determining the values of R_1 and RATIO which produced $T_b = 34\text{K}$ at $l = 180^\circ$ and $T_b = 370\text{K}$ at $l = 10^\circ$. The fitted values are $R_0 = 11.2\text{kpc}$, $R_1 = 1.91\text{kpc}$ and $\text{RATIO} = 0.692$, so $H_{\text{reg}}/H_{\text{irreg}} = 0.66$. H_0 is chosen to give the

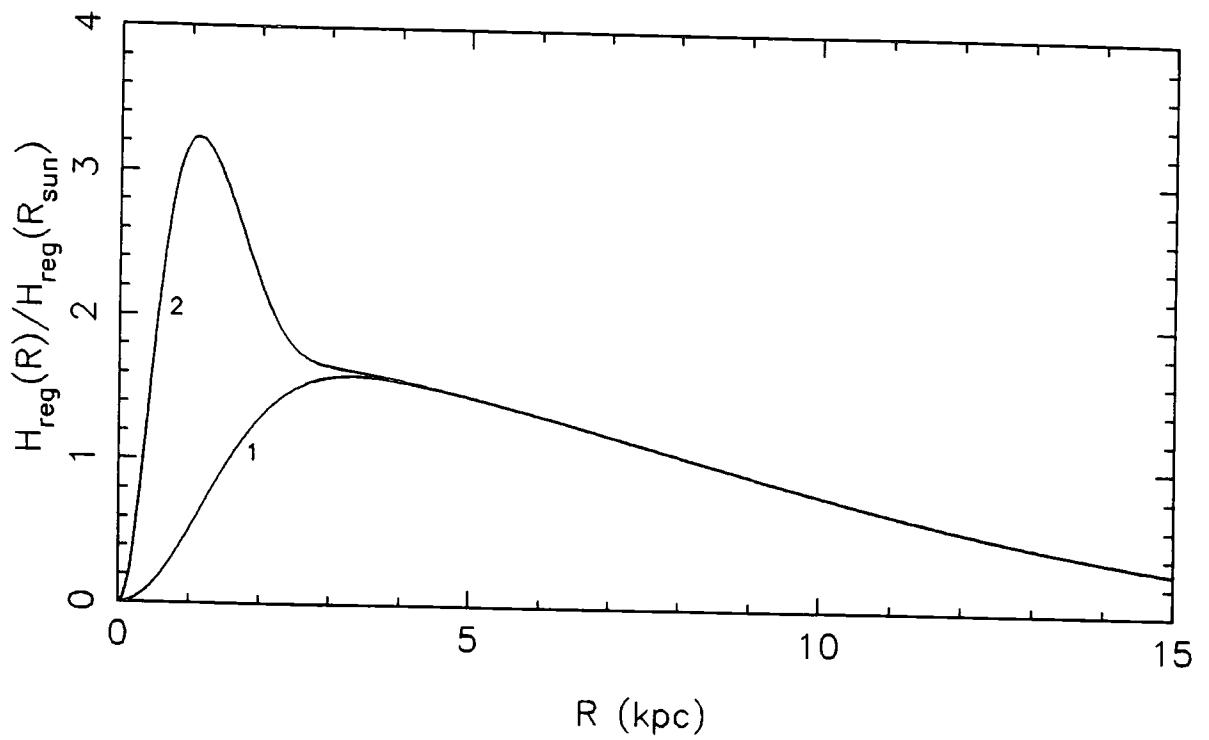


Figure 3.5: Radial variation of the magnitude of the regular component of magnetic field, $H_{\text{reg}}/H_{\text{reg}\odot}$. 1) of the form used by Kearsy (equation 3.11) but scaled R_{\odot} to 8.5 kpc. 2) used in equation 3.12.

observed value of $3.2 \mu\text{G}$ at the Sun.

3.3.5 The spiral arm pattern

Having determined the underlying variation of magnetic field strength with galactocentric radius and having set up our model of how the spiral arms will modulate the emissivity the final step is to find the spiral arm pattern that best fits the observed galactic plane profile. Here we are able to build on work that has been done over a considerable period by the Durham group. The starting point was the combined model of Georgelin's HII region arms and Verschuur's map of neutral hydrogen that was used by French and Osborne (1976) to fit the 'observed' profile at 150 MHz of Landecker and Wielebinski(1970). Kearsy(1983) was able to refine this by moving and reconnecting the arms within the uncertainties of the original maps when the 408 MHz survey data became available. After removing the thermal features from the observed profile Broadbent, in her thesis was able to obtain the best fit so far to the synchrotron profile. In the outer half of the Galaxy we have no reason to further modify her final spiral arm pattern but there is now some independent evidence for the structure of the inner part of the Galaxy that needs to be taken into account here.

Blitz(1993) has shown that there is actually a bar running across the Galactic centre as evidenced by the asymmetry in the near infrared emission from stars and the kinematics of the gas in central bulge. We therefore have refined the spiral structure of the Galaxy by including the bar with the geometry indicated by Blitz in the centre part of the Galaxy as shown in Fig 3.6. We do not attempt to model the bar itself in synchrotron emission for two reasons. Firstly because the orientation of the bar is such that it falls almost entirely in the region $|l| < 5^\circ$ where the thermal and non-thermal separation technique cannot be applied and secondly because there is no prediction about the orientation and regularity of the magnetic field in the bar. Because the bar is at a small angle to the line of sight, one has the

paradoxical situation that a strong effect of the bar in lining up the magnetic field along it might result in a deficit in the synchrotron emission as observed from the sun. On the other hand, from the evidence of bars in other barred-spiral galaxies, we can assume that the ends of the bar are connected to the spiral arms. We have therefore adjusted the inner end of the arms accordingly and adjusted their shapes to restore best agreement with the observed profile. The result is shown in Fig. 3.6 where each arm is given a number. The positions of the arms labelled with these numbers are tabulated in Table 3.1. ϕ_0 is the angle at the inner end of the arm and $\Delta\phi$ is its angular extent. Each column in the table contains the distances of the arm from the galactic centre, in units of 0.85kpc, at angles :

$$\phi_n = (\phi_0 - 15n)^\circ \quad \text{where } n = 0, 1, 2, \dots, 24.$$

All the expressions introduced to model the distribution of emissivity in the Galaxy are listed in Table 3.2 together with the chosen values of their parameters. When they are used together with the spiral arm pattern of Fig. 3.6 the model of the 2-dimensional distribution of Brightness Temperature in l and b can be calculated. The final step was to convolve this to the 51' HPBW of the observations. Fig. 3.7 shows the cut along $b = 0^\circ$ and the corresponding observed nonthermal profile from which we have removed the contributions of all catalogued supernova remnants which are smaller than the HPBW of the survey. We have also blacked in the sharp minima in the profile due to the over subtraction of bright HII regions in our thermal separation procedure. One sees that the modelled profile follows the observed one quite closely but that the former is smoother than the latter. Our explanation for this is that the actual synchrotron emissivity along the spiral arms is clumpy and that our model represents an average over the clumps. Three regions on the profile where there is a particular observed excess of emission over that of the model are worth mentioning. That in the longitude range $86^\circ > l > 77^\circ$ is the remaining contribution of the Cygnus complex after the subtraction of a relatively

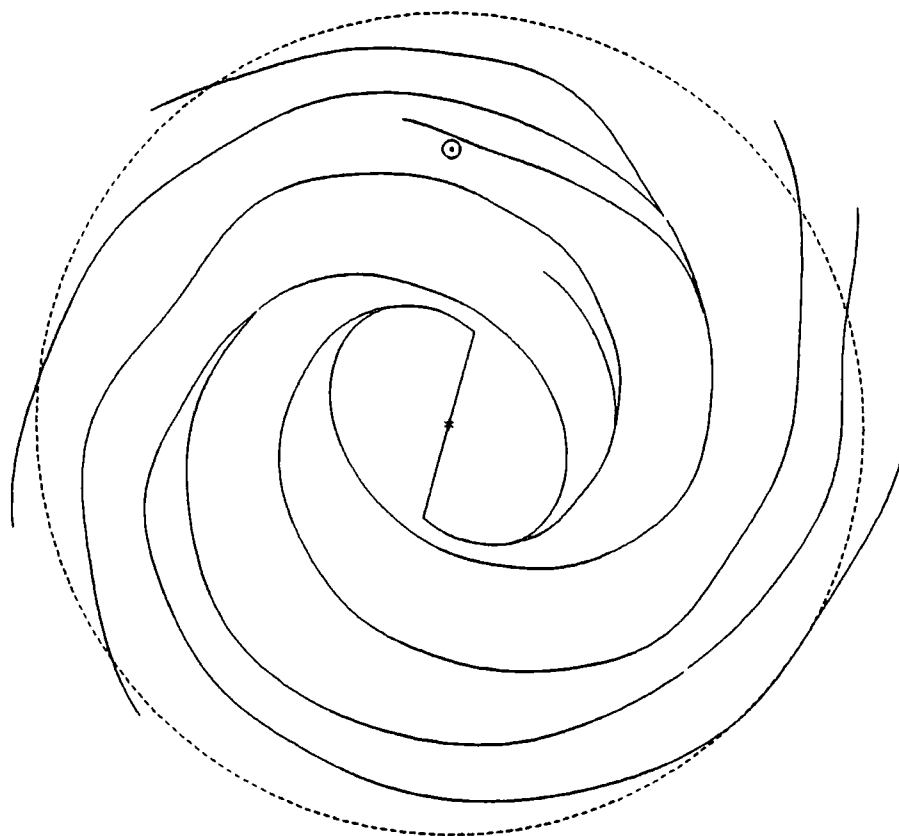


Figure 3.6: The final spiral arm pattern. The position of the Sun, between the inner, Sagittarius arm, and the outer, Orion spur, is marked by ☉

Table 3.1: Positions of arms corresponding to Fig 3.6

ARM	1	2	3	4	5	6	7	8	9	10	11
ϕ_0	15	330	150	300	300	135	45	45	65	90	195
$\Delta\phi$	330	285	285	165	210	75	90	150	75	60	255
$R(\phi)$	3.00	4.16	4.16	6.89	6.89	10.54	9.31	9.31	8.63	5.14	3.00
	3.40	4.20	4.46	7.53	7.61	10.97	10.24	9.40	8.80	5.23	3.40
	3.80	4.05	4.59	7.91	8.50	11.60	11.22	9.61	8.54	5.31	3.80
	4.16	3.80	4.89	8.33	9.69	12.07	11.48	10.03	8.46	5.48	4.16
	4.46	3.55	5.14	8.84	10.20	12.58	11.99	10.58	8.71	5.61	4.20
	4.63	3.35	5.48	9.35	10.71	14.41	12.45	10.88	9.61		4.05
	4.80	3.25	5.78	9.56	10.97		13.39	11.22			3.80
	5.10	3.25	6.16	9.69	11.26			11.90			3.55
	5.40	3.35	6.59	9.90	11.65			12.33			3.35
	5.65	3.60	6.89	10.11	11.94			13.09			3.25
	5.95	3.95	7.48	10.24	12.37			13.90			3.25
	6.42	4.42	8.03	10.54	12.75						3.35
	6.84	5.10	8.69		12.75						3.60
	7.31	5.95	9.08		13.26						3.95
	7.91	6.80	9.08		14.07						4.51
	8.59	7.61	9.73								5.36
	9.27	7.99	11.01								6.19
	9.44	8.37	11.65								6.89
	9.86	8.80	12.37								
	10.54	9.31	13.22								
11.14											
12.45											
13.85											

Table 3.2: Summary of all the parameters that used for predicting synchrotron emission of the Galaxy

Quantity	Equation/Description/Value	Eqn.
Brightness temperature	$T_b(\nu) = 6.168 \times 10^4 \nu^{-2.8} \int N_e(s) [\rho_c(s) H_{\text{reg}}(s) \sin\theta]^{1.8} + 0.6861 N_e(s) \left[\frac{\rho_c(s) H_{\text{reg}}(s)}{F} \right]^{1.8} Y(s) ds$	3.6
Irregular field realignment in arms	$Y(s) = 1 - 0.477 \left(\frac{\rho_c^2 - 1}{\rho_c^2} \right) \cos^2\theta$	3.7
Gas compression factor across an arm	$\rho_c = CRf(z) \exp(-0.5a^2/0.031) + 1$ $CR = \begin{cases} 2.5 & R \leq 8.5 \text{ kpc} \\ (12.75 - R)0.5 & 12.75 \leq R \leq 8.5 \text{ kpc} \end{cases}$	3.8
Compression demodulation with z	$f(z) = \begin{cases} 1 + 0.908z - 23.529z^2 + 37.35z^3 & z \leq 0.425 \text{ kpc} \\ 0 & z \geq 0.425 \text{ kpc} \end{cases}$	3.10
Flux of electrons	$\text{Flux} = N_e(s) E^{-\gamma} dE$ $N_{e\odot} = 80 \text{m}^{-2} \text{s}^{-1} \text{sr}^{-1} \text{GeV}^{-1}$	3.3
Spectral index: Energy Frequency	$\gamma = 2.6$ $\alpha = (\gamma + 3)/2 = 2.8$	
Electron flux density	$N_e \left(\frac{z}{z_0} \right) = 80 \times \begin{cases} 1.063 & \frac{z}{z_0} \leq 0.29 \\ 1.063 + 1.099 \left(\frac{z}{z_0} \right) - 4.915 \left(\frac{z}{z_0} \right)^2 + 4.307 \left(\frac{z}{z_0} \right)^3 - 1.569 \left(\frac{z}{z_0} \right)^4 + 0.256 \left(\frac{z}{z_0} \right)^5 - 0.015 \left(\frac{z}{z_0} \right)^6 & 0.29 \leq \frac{z}{z_0} \leq 0.94 \\ 0.30788 - 0.0217 \left(\frac{z}{z_0} \right) & 0.94 \leq \frac{z}{z_0} \leq 14.20 \\ 0 & \frac{z}{z_0} \leq 14.20 \end{cases}$ $z_0 = 0.591 + 0.0767R + 0.0147R^2$	3.5
Regular field	$H_{\text{reg}}(R) = H_0 (1 - \exp(-2.768R^2)) \left(\exp - \left(\frac{R}{R_0} \right)^2 + \exp - \left(\frac{R}{R_1} \right)^4 \right)$ $H_{\text{reg}\odot} = 3.2 \mu\text{G}$	3.12
Normalization parameter	scale lengths: $R_0 = 11.0 \text{kpc}$ $R_1 = 1.91 \text{kpc}$ $\text{RATIO} = 0.692 \Rightarrow F = \frac{H_{\text{reg}}}{H_{\text{irreg}}} = (0.6861 \text{RATIO})^{1/1.8} = 0.66$	

large thermal component. In our model the junction of arms 7 and 8 is in this direction. The observed emission in the direction $30^\circ > l > 27^\circ$ partly fills in the predicted trough in the profile due to a long line of sight in the interarm region. In this direction there lies the bifurcation of the spur 10 from the main arm 9. In the region of $l = 330^\circ$ the observed excess is in the direction which includes the splitting of arms 1 and 2. We suspect that there is some mechanism, not included in our model, which produces this enhanced emissivity near to a point where arms split. This may be due either to an increase of overall magnetic field strength or simply to a relative increase in the irregular component of the field due to turbulence.

3.3.6 Field irregularities in arm and interarm regions

In the model considered so far the irregular magnetic field component undergoes a degree of alignment along the arm due to compression of the frozen in field as the density wave acts on the interstellar gas. This was accounted for by the $Y(s)$ term in equation 3.6. Irregularities in the field will be generated by supernova explosions, and the stellar winds of young O and B type stars. These are more common in the spiral arms than in the interarm regions so it is possible that the alignment factor is reduced or even reversed.

One can search for evidence for this in the synchrotron emission from other spiral galaxies of a similar type to our own. There is a small number of these that are near enough that the beam size of the radio telescope is less than the typical spiral arm separation. It is believed that the Hubble Type and Luminosity Class of our Galaxy is SbcII although there is some uncertainty because it is viewed from the inside. M81 is a two-armed spiral galaxy classified SabI-II. The best radio continuum mapping has been done by Krause et al.(1989) using the Effelsberg telescope at 6.5 cm and the VLA at 20 cm. At the latter wavelength the resolution is 0.7×1.1 kpc in the plane of the Galaxy. The two main spiral arms are clearly seen in total intensity

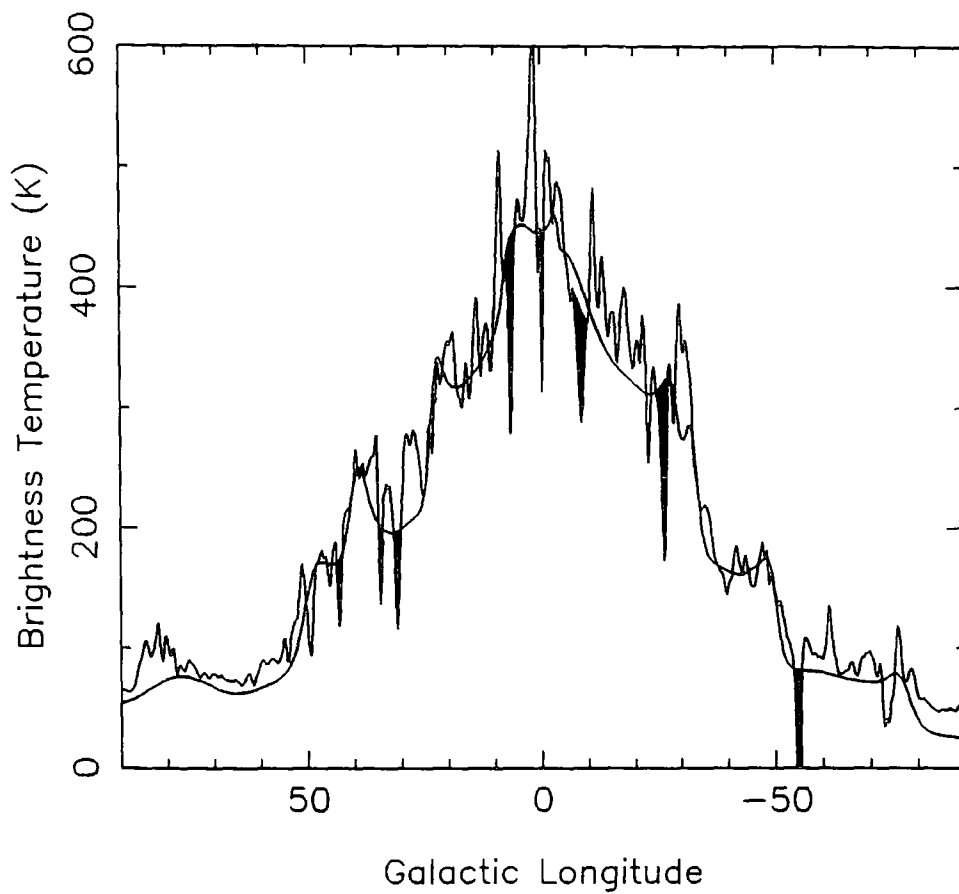


Figure 3.7: The profile along the galactic plane of the observed and predicted synchrotron emission at 408 MHz. The smoother line shows the predicted. Local minima in the observed nonthermal emission due to over subtraction of high luminosity HII regions are shown blacked in.

and the polarization vectors indicate that the regular component of the field runs along the arms. However the degree of polarization has its greatest values in the interarm regions. In the southwest interarm the deduced mean magnitudes of the two components of the field are $H_{\text{reg}} = 4.5 \pm 1.0 \mu\text{G}$ and $H_{\text{irreg}} = 4.0 \pm 1.0 \mu\text{G}$, while in the northeast interarm they are $H_{\text{reg}} = 3.5 \pm 1.0 \mu\text{G}$ and $H_{\text{irreg}} = 5.5 \pm 1.0 \mu\text{G}$. The implication is that for this galaxy there is a greater degree of turbulence in the arms. The galaxy M51 is classified ScI. Horellou et al (1992) have studied this at 18cm and 20.5cm using the VLA with a resolution of 2 kpc. Again the total emission peaks along the optical spiral arms and the degree of polarization is generally weak suggesting appreciable turbulence of the magnetic field in the arms. However, for this galaxy the most pronounced minima in polarization occur in the interarm regions implying alignment of field by compression in the arms.

It is not clear from the above whether the field alignment factor $Y(s)$ should be applied to our Galaxy. We have tried therefore removing this factor. It is necessary, in order to retain a good fit with the overall longitudinal variation of emission, to adjust the ratio of the regular to the irregular component and the values of R_0 and R_1 .

We can see in Fig 3.8 and Fig 3.9 that removing the parameter $Y(s)$ from the calculation, gives a significantly worse fit although we have adjusted the free parameters in order to give the same value of observed temperature 370 K at longitude $l = 10^\circ$ and 34 K $l = 180^\circ$. The removal of the parameter $Y(s)$ gives much higher values at the emission peaks corresponding to directions where the arms are viewed tangentially than in the observed profile. We conclude that in our Galaxy the alignment of the field by compression in the arms is not removed by additional turbulence there and we shall continue to include the parameter $Y(s)$ in the calculation of the 408 MHz emission and the calculation of the synchrotron emission with absorption at decameter wavelength that is discussed in the next chapter.

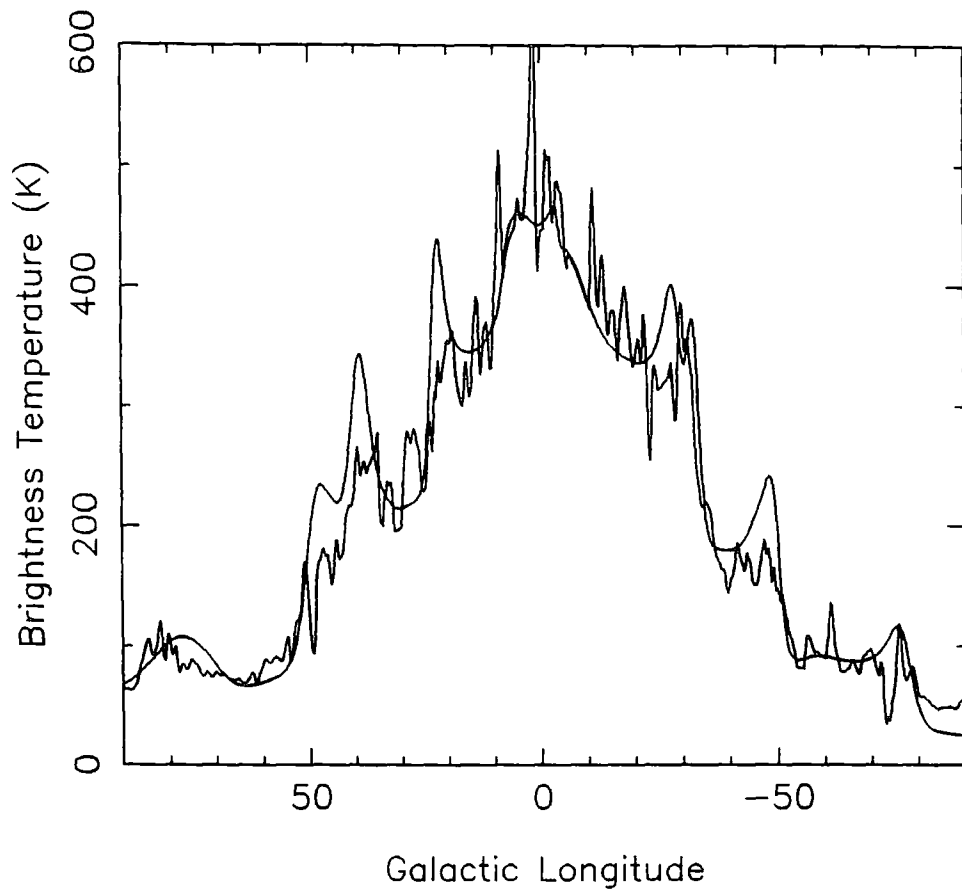


Figure 3.8: The profile along the galactic plane of the observed and predicted synchrotron emission at 408 MHz. The smoother line shows the predicted after removing $Y(s)$ and refitting by setting $R_1 = 11.0$ kpc. The new value for R_0 is 1.89 kpc and F is 0.697.

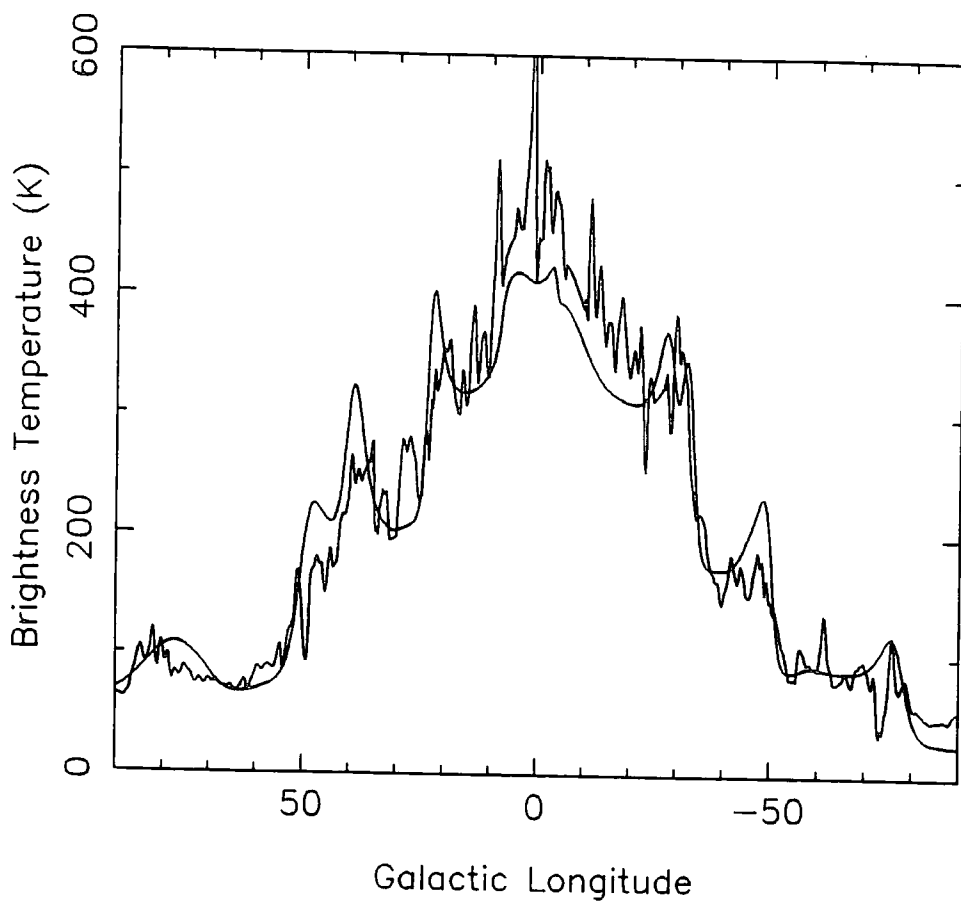


Figure 3.9: As for Fig. 3.8 but with the predicted line fitted by setting $R_0 = 1.91$ kpc. The new value for R_1 is 11.77 kpc and F is 0.698.

Chapter 4

The Absorption model

In chapter 3, we discussed the synchrotron emission model and described how we refined it to get a better fit with the observational data at 408 MHz. At this frequency there is very little absorption in the interstellar medium. As we know, at lower frequencies, the free-free absorption due to thermal electrons becomes significant. The thermal electrons in the interstellar medium absorb some synchrotron emission along the line of sight. Here we develop our synchrotron model to include the effect of absorption at lower frequencies (34.5 MHz and 29.9 MHz have been chosen) in order to obtain direct information on the line of sight distribution of the emissivity and some indication of the relative positions of the peaks of synchrotron radiation and ionised hydrogen emission.

Reynolds(1984) suggested that instead of two major phases, (i.e. cold clouds in a warm intercloud medium) the atomic component of the interstellar medium is composed of four phases: (1) cold($T \sim 80$ K), dense, and largely neutral hydrogen, HI, clouds (cold neutral medium or CNM); (2) a warm($T \leq 8000$ K) HI, surrounding the cold clouds in an envelope or distributed through much of space as an "intercloud medium" (warm neutral medium or WNM); (3) a warmer ($T \sim 8000$ K), ionized hydrogen medium (warm ionized medium or WIM); and 4) a hot($T \sim 10^6$ K), highly ionized but low density medium (hot ionized medium or HIM). The

CNM is distributed in relatively dense clouds that occupy an insignificant fraction of the interstellar volume. In contrast, the WNM is widely distributed and fills a substantial fraction of interstellar volume. The distribution of CNM and WNM can be found from HI 21cm emission data. The distribution of the WIM appears to be widely spread, constituting $\sim 30\%$ of the mass of diffuse gas. Kulkarni and Helies(1987) showed that most of interstellar thermal electrons come from the WIM whose 3-dimensional distribution can be deduced by studying (1) pulsar dispersion measures, (2) optical $H\alpha$ and radio recombination line emission and (3) low-frequency radio absorption. From studies of the diffuse soft X-ray emission and OVI UV absorption, it appears that a large fraction of interstellar space is occupied by the HIM. However, there is no consensus on the filling factor of the HIM.

In this chapter we model the distribution of thermal electrons by studying the distribution of radio recombination line emission as a function of Galactic longitude and velocity but first we consider the available low frequency surveys.

4.1 Low frequency surveys

At frequencies below ~ 50 MHz, the brightness temperature of the synchrotron emission from the Galaxy is nearly everywhere higher than the electron temperatures of the ionized gas clouds of the Galaxy. These clouds behave like absorbers for the low frequency radiation passing through them. Especially at frequencies around 30 MHz, the absorption of the radiation by the ionized gas throughout the disc of the Galaxy can be observed because the absorption is important but we can still see the transmission of radiation from the inner part of the Galaxy. However at frequencies below about 15 MHz, the absorption is almost complete. Hence, surveys at frequencies ~ 30 MHz can provide information on the pattern of the disc better than the former one which can provide only information within

a few kiloparsec of the Sun. There are two surveys at 34.5 MHz and 29.9 MHz which we have chosen for comparison with our model. In order to understand the reliability of the deduced absorption one needs to consider the angular resolution and the method of the calibration of the surveys so this is dealt with next.

4.1.1 The 34.5 MHz GEETEE survey

The 34.5 MHz survey was made by Dwarakanath and Uday Shankar(1990), using the Gauribidanur Radio Telescope located at $13^{\circ}36'12''$ N near Bangalore in India, the GEETEE array. The antenna system is in the shape of letter T and consists of 1000 East-West aligned full wavelength dipoles. There are 4 rows of 160 dipoles along a 1.4 km East-West arm and 90 rows, of 4 dipoles each, down a 0.45 km long South arm. In the actual survey only one of the East-West rows was used together with 88 of the North-South rows. The array is used as a transit instrument and in theory the whole of the visible sky could be surveyed in 24 hours. In fact 15 days of observations were recorded to check the repeatability of the measurements. The instrumental zenith is at Declination 14.1° and the survey covers the Declination range -50° to $+70^{\circ}$ and the complete 24 hours of Right Ascension. The synthesized beam has a half power beam width (HPBW) of $26' \times 42'$ sec ($\delta - 14.1^{\circ}$) and the survey can thus be convolved to the $51'$ circular beam of the 408 MHz survey for comparison. The effective area of this telescope is approximately $20,000 \text{ m}^2$. The mean sky brightness is about 10,000 K and the minimum detectable flux density is of the order of 10 Jy with an integration time of 24 s and a bandwidth of 400 kHz. To calibrate the brightness temperature scale of the survey the bright radio galaxy Cygnus A was used whose absolute flux density at 34.5 MHz is known to 5%.

We are grateful to Drs. Dwarakanath and Uday Shankar for providing us with the survey in digital form. This consisted of 72 maps, each covering 2 Hr of

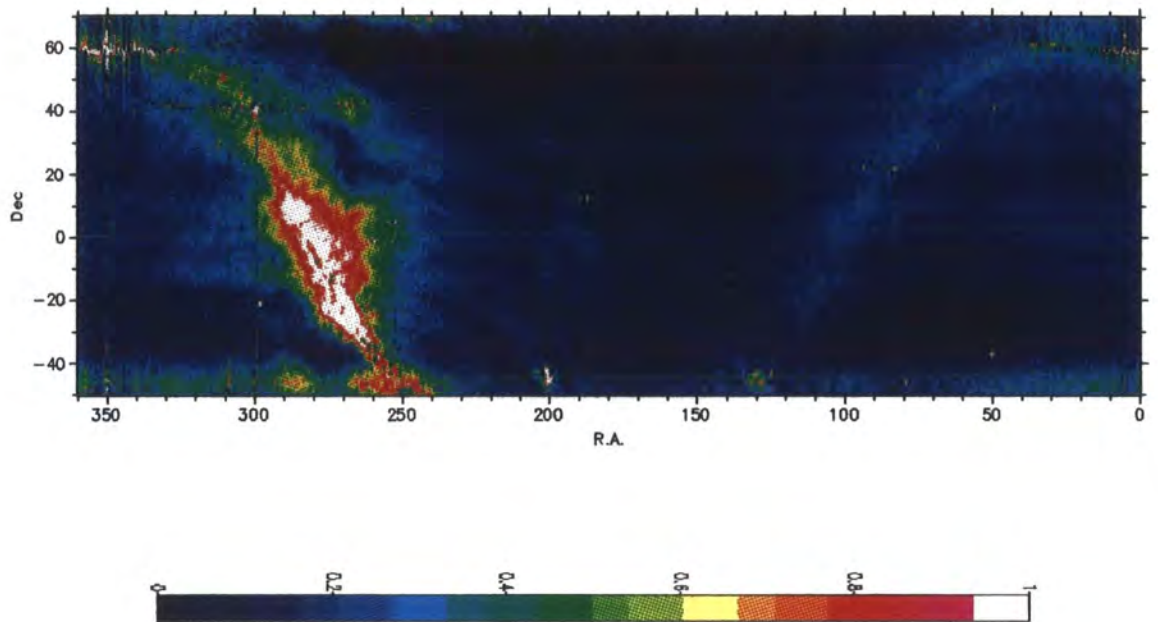


Figure 4.1: The 34.5 MHz survey of Dwarakanath and Uday Shankar made with the GEETEE Array(The Gauribidanur Radio Telescope), plotted in celestial coordinates. The declination range covered is from -50° to $+70^\circ$. The range of brightness temperature plotted is from 0 to 80,000 K.

R.A. and 20° of Dec. The result of our mosaicing these together is shown in Fig. 4.1. The bright emission of the Galactic plane along the first quadrant of Galactic longitude can be followed from the Galactic centre at R.A. = 265.0° , Dec. = -28.9° to $l = 90^\circ$ at R.A. = 317.6° , Dec. = $+48.1^\circ$. Falling across this however are the residual sidelobes of the Cygnus A source at R.A. = 299.4° , Dec. = $+40.6^\circ$. Those of the even brighter Cas A supernova remnant at R.A. = 350.3° , Dec. = $+58.5^\circ$ cover more of the plane towards the anticentre. The authors of the survey point out some other artifacts that can also be seen on this figure. These are the areas of extended emission centred around R.A. = 265° , Dec. = $+42^\circ$ and R.A. = 255° , Dec. = $+30^\circ$ which do not appear on surveys at higher frequencies. Horizontal banding can be seen between Dec. $\pm 15^\circ$ on some of the darker parts of the map. The bright features below Dec. -40° are mostly spurious although the Vela nebula at R.A. = 130° is real. The spurious areas of extended emission could be related to problems with the low spatial frequency calibration. This was done by extrapolation from the longer baseline calibration given by the Cygnus A point source.

In order to attempt to remove these effects we used the 38 MHz survey of Milogradov-Turin and Smith (1973) and Milogradov-Turin (1984). This was made with the Jodrell Bank 75 m Mk I telescope. At this frequency the beam width is 7.5° . This is far too large to give any information about absorption features along the Galactic plane but it is expected to be reliable for large angular scale features. We were able to use a digitised version of their published contour map that had been prepared by Lawson et al. (1987) for their study of the spectral index of the radio continuum emission. This is shown in Fig. 4.2. It extends down to Dec. -25° and so includes almost all of the first quadrant of Galactic longitude.

To compare the two maps we convolved the GEETEE map to a circular 7.5° beam and divided all the pixels by a constant 1.27 to convert to the equivalent brightness temperature at 38 MHz. By dividing this map, pixel by pixel, in the

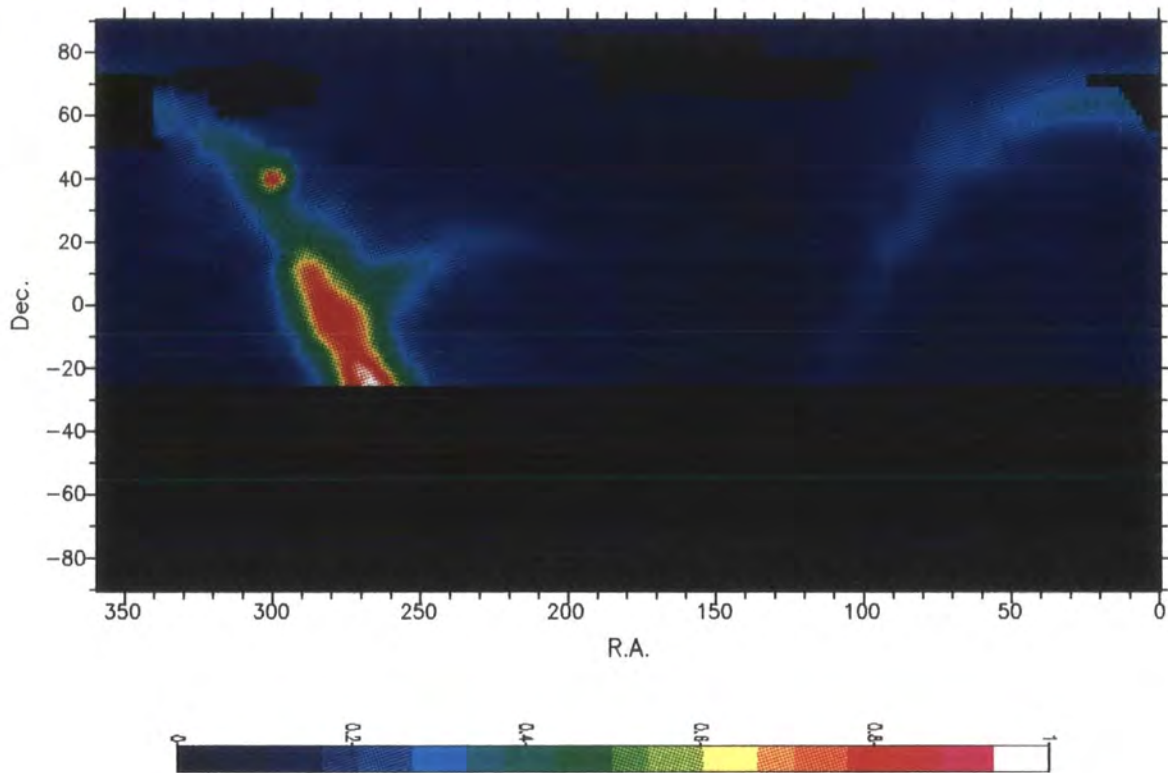


Figure 4.2: The 38 MHz survey of Milogradov-Turin and Smith made with the Jodrell Bank Mk I radio telescope. The declination range covered is from -25° to $+90^{\circ}$. The range of brightness temperature plotted is from 0 to 50,000 K.

region of overlap by the observed 38 MHz map we obtained a map of correction factors. When we divided the original GEETEE map by this we obtained a 'corrected' GEETEE map as shown in Fig. 4.3. This map shows the same fine detail as the original but would agree with the Jodrell Bank map if it were convolved to the same beam size and converted in frequency assuming a uniform spectral index. For the small difference in frequency this is not a critical assumption. Along the Galactic plane the absorption would have been rather weaker at the higher frequency but the much larger beam size would have made this negligible.

One sees in Fig. 4.3 that most of the spurious features have gone away or have been much reduced. The arc of the 'North Polar Spur', identified with the shell of a nearby, old, supernova remnant can be more clearly seen also.

Fig. 4.4 shows the same map, replotted in Galactic coordinates to show the details of the first quadrant of Galactic longitude. The range of brightness temperatures plotted has been adjusted to show the details of the absorption near to the Galactic plane. A comparison of these absorption regions with the contour plot of separated thermal emission at 408 MHz in Fig. 2.6a shows qualitative agreement. We shall use this map, convolved to the 408 MHz beam of 51' to deduce the 'observed' absorption.

4.1.2 The 29.9 MHz Fleurs survey

This survey was made by Jones and Finlay (1974). The published part of the survey covers the area $225^\circ < l < 30^\circ$ and $-10^\circ < b < +10^\circ$ observed at Fleurs Observatory N.S.W. (latitude 33.86°S). The aerial used for the 29.9 MHz survey consisted of an East-West array of 212 colinear half-wave dipoles which gave a fan beam along the meridian. This fixed array was used in conjunction with two movable arrays which were placed symmetrically to the north and south of the EW array at a total of 50 different spacings in order to obtain resolution in the North-

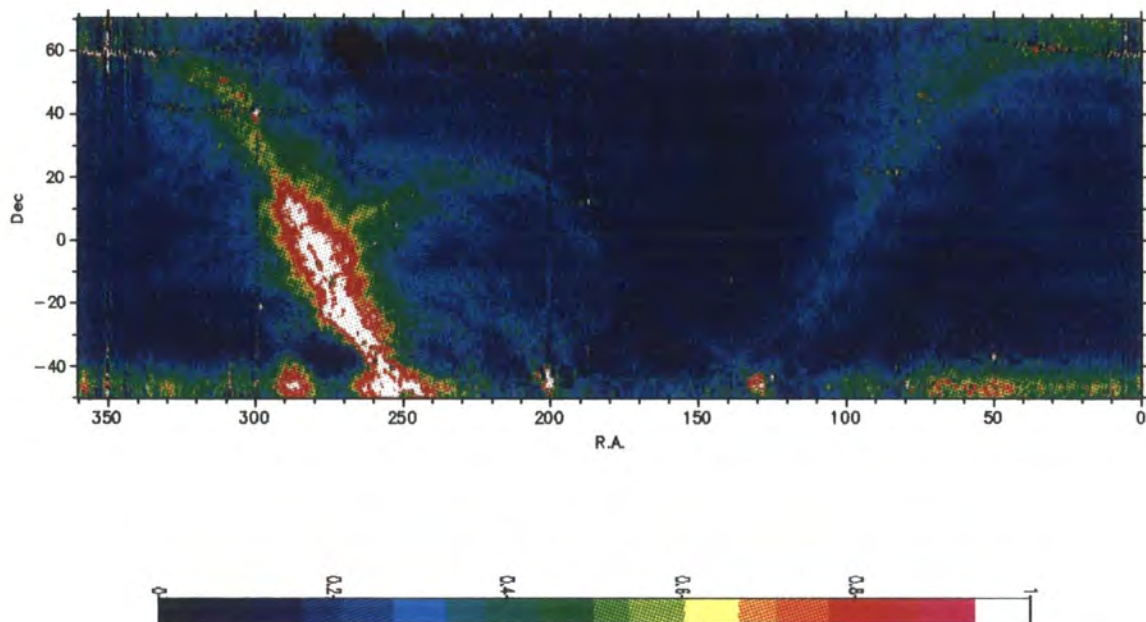


Figure 4.3: The 34.5 MHz survey of Dwarakanath and Uday Shankar after we had corrected some of the large angular scale anomalous areas of emission by the use of 38 MHz map. The range of brightness temperatures plotted is from 0 to 50,000 K.

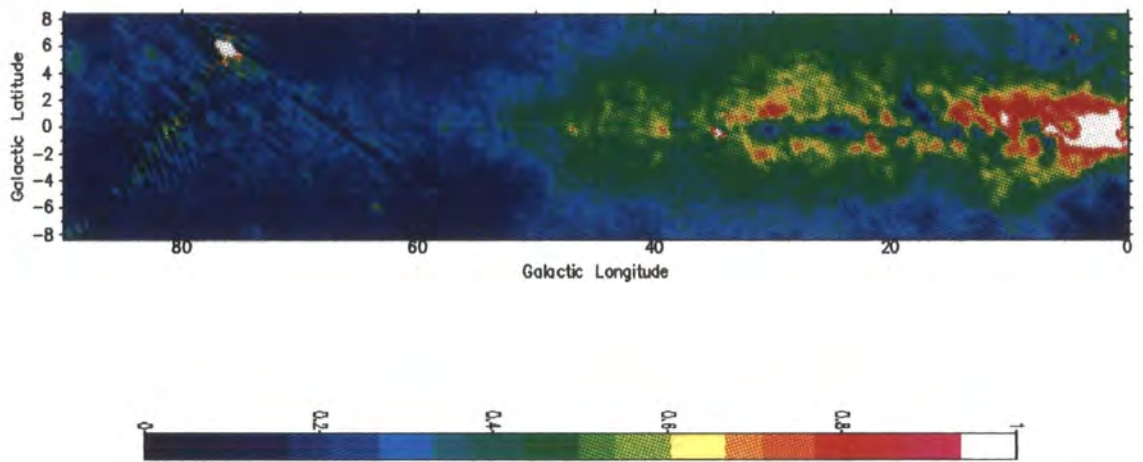


Figure 4.4: The 34.5 MHz brightness temperature of Fig.4.3 replotted in Galactic coordinates for the first quadrant of Galactic longitude. The latitude range is $\pm 8.33^\circ$. The range of brightness temperature plotted is from 0 to 100,000 K.

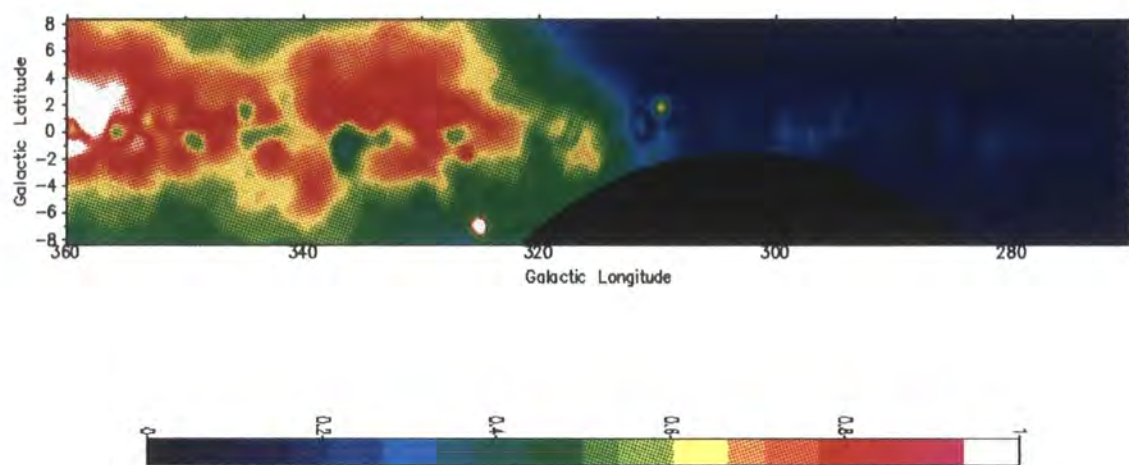


Figure 4.5: The fourth quadrant of Galactic longitude of 29.9 MHz as digitised by us from the published contour map of Jones and Finlay(1974). The range of brightness temperature is from 0 to 250,000 K. The black region is further south than $\text{dec.} -64^\circ$, the limit of the survey.

South direction using aperture synthesis. Each of these movable arrays consisted of three half-wave dipoles. The HPBW of the synthesized beam was $48' \times 48'$ sec ($\delta + 33.86^\circ$). The temperature scale was calibrated with reference to the bright source Hydra A. Because of interaction between the EW array and the NS elements when at the close spacing position the central 2λ portion of the former had to be removed. This means that the corresponding broad scale component of the sky map would be missing. The authors describe how the restoration of this component was attempted using a low resolution 30 MHz survey made with the Parkes 64 m dish.

This being an old survey no original digital data were available so we made our own digitisation of the published contour maps. Fig. 4.5 shows the 4th quadrant of Galactic longitude plotted from this digitisation. The range of Galactic longitude which is of interest to us is from 297° to 355° this covers a Dec. range from -33° to -62° . This in turn means that the HPBW in Dec. varies between $48'$ and $54'$. Overall then the effective resolution of this survey is very similar to that of the 408 MHz survey and no further convolution is required.

4.2 The distribution of ionized hydrogen

In order to calculate the absorption of the synchrotron radiation the distribution of the mean square density of thermal electrons, $\langle n_e^2 \rangle$, along a line of sight through the Galaxy must be known. It can be deduced from the brightness temperature of an appropriate recombination line as a function of frequency. In the second chapter (equation 2.35), we have shown that

$$\begin{aligned} \int T_L(\nu) d\nu &= 2.478 \times 10^4 \nu^{2.1} T_e^{-1.15} T_c \\ \tau &= 0.08235 T_e^{-1.35} \nu^{-2.1} \int n_e^2 dr \\ T_c &= \tau T_e \end{aligned}$$

where T_L is the recombination line temperature, T_c is the thermal continuum temperature and T_e is the electron temperature.

When gas travelling at a velocity v with respect to the observer radiates a line frequency ν_L , the frequency is shifted to

$$\nu = \nu_L \left(1 - \frac{v}{c}\right) \quad (4.1)$$

and

$$\frac{d\nu}{\nu_L} = \frac{dv}{c}$$

Equation 2.35, can then be written as

$$\left[\frac{n_e^2}{\text{cm}^{-6}} \right] = \left[\frac{T_L}{\text{K}} \right] \frac{dv}{dr} \times 1.633 \times 10^{-9} \times \left[\frac{\nu_L}{\text{MHz}} \right] \times \left[\frac{T_e}{\text{K}} \right]^{1.5} \quad (4.2)$$

If we take $T_e = 7000$ K which is deduced by Mezger(1978) for ELD HII regions then the above equation becomes :

$$\left[\frac{n_e^2}{\text{cm}^{-6}} \right] = 9.5639 \times 10^{-4} \left[\frac{T_L}{\text{K}} \right] \frac{dv}{dr} \times \left[\frac{\nu_L}{\text{MHz}} \right] \quad (4.3)$$

It has been common to assume that the motions of the gas around the galactic centre are circular and the angular velocity, $\Omega(R)$, is a decreasing function only of distance, R , from the galactic centre. The distance from an observer to the emitting region is r . The observer is at the distance, R_o , from the galactic centre and rotating about the centre with an angular velocity Ω_o . The radial velocity, v , measured by the observer is the Doppler-shifted velocity of the gas along the line of sight minus the component of the observer's motion, $\Omega_o R_o$, as shown in Fig 4.6. This difference is

$$v(R, l) = \Omega R \cos(90^\circ - l - \theta) - \Omega_o R_o \cos(90^\circ - l)$$

$$= \Omega R(\sin\theta\cos l + \cos\theta\sin l) - \Omega_0 R_0 \sin l$$

where l is the galactic longitude (at $b = 0^\circ$) of the line of sight in equation and θ is galactocentric azimuth. Fig 4.6 shows that $R\sin\theta = r\sin l$ and $R\cos\theta = R_0 - r\cos l$, thus the radial velocity can be written as

$$v(R, l) = R_0 [\Omega - \Omega_0] \sin l. \quad (4.4)$$

If the function $R_0[\Omega - \Omega_0]$ is known, in principle, distances along the line of sight in the galactic plane can be attributed to each measured velocity. IAU commission 33 recommended the use of the standard values, distance of the Sun from the galactic centre, $R_0 = 8.5$ kpc and the linear velocity $\Theta_0 = \Omega_0 R_0 = 220$ km/s.

From equation 4.3, we have the relationship between electron density, line frequency and the line temperature from which we can find the value of dv/dr from the radial velocity in equation 4.4. From Fig. 4.6, we can find the relationship between R_0 , R , and r as written in the following equation:

$$R^2 = R_0^2 + r^2 - 2rR_0\cos l \quad (4.5)$$

From this relationship, at any longitude we can find two values of r which we call 'near' and 'far' distances that have the same galactocentric distance R . It means that these two points will appear at the same position in $l - v$ diagram. From the above equation, we then get dv/dr by using the chain rule:

$$\begin{aligned} \frac{dv}{dr} &= \frac{dv}{d\Omega(R)} \frac{d\Omega(R)}{dR} \frac{dR}{dr} \\ \frac{dv}{d\Omega(R)} &= R_0 \sin l \\ \frac{d\Omega(R)}{dR} &= f'(R) \end{aligned} \quad (4.6)$$

$$\frac{dR}{dr} = \frac{(r - R_0 \cos l)}{R}$$

therefore

$$\frac{dv}{dr} = \frac{R_0 \sin l (r - R_0 \cos l)}{R} f'(R) \quad (4.7)$$

Clemens(1985) fitted a polynomial of the following form to the rotation curve in Fig 4.7 with the coefficients shown in Table 4.1.

$$\Omega(R) = \begin{cases} \sum A_i R^i, & \text{where } R < 0.09 R_0 \\ \sum B_i R^i, & 0.09 R_0 < R < 0.45 R_0 \\ \sum C_i R^i, & 0.45 R_0 < R < 1.6 R_0 \\ D_0, & R > 1.6 R_0 \end{cases} \quad (4.8)$$

Of the Hydrogen recombination lines that fall within the parts of the radio spectrum reserved for radio astronomy the H166 α is the most appropriate for the observation of the relatively low density ionised gas with which we are concerned. Currently surveys are available only for $b = 0^\circ$.

In the northern galactic plane we have used the data observed by Lockman(1976), and shown in Fig 4.8.

This covers the area of longitude $358^\circ \leq l \leq 50^\circ.5$. (There is little emission at larger longitudes except for the region of the Cygnus complex, which we cannot deal with because of the problem of the strong source Cygnus A). These data were taken with the 42 m telescope of the NRAO with HPBW of 21' at the recombination line frequency 1.425 GHz and velocity resolution of 5.48 km s⁻¹. (Note that Lockman used T_L as an antenna temperature, therefore the value of the emission has to be multiplied by 1.32).

In the southern galactic plane we use the survey of Cersosimo et al.(1989), shown in Fig 4.9. This covers the area $298^\circ \leq l \leq 4^\circ$. The data were taken by using the 30 m diameter antenna of the IAR with HPBW 34' at the same frequency and a velocity resolution of 15.8 km s⁻¹.

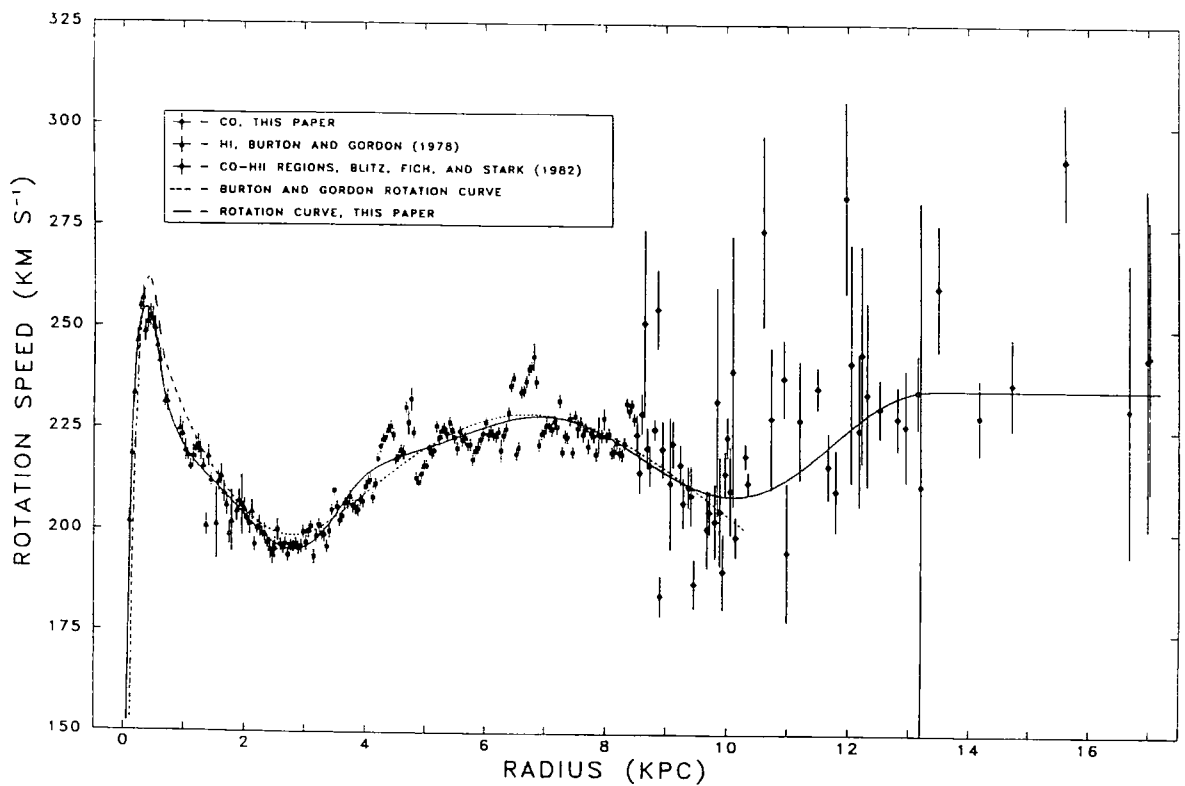


Figure 4.7: Plots of the rotation speed versus galactocentric radius (Taken from Clemens, 1985). The solid line correspond to the polynomials in equation 4.8.

Table 4.1: Coefficients of the Rotation Curves

Coefficient	$R < 0.09R_0$
A_0	0.00
A_1	+3069.81
A_2	-15809.80
A_3	+43980.10
A_4	-68287.30
A_5	+54904.00
A_6	-17731.00
$0.09R_0 < R < 0.45R_0$	
B_0	+325.0912
B_1	-248.1467
B_3	+231.8701
B_4	-110.7353
B_5	+25.0730
B_6	-2.1106
$0.45R_0 < R < 1.6R_0$	
C_0	-2342.6564
C_1	+2507.6039
C_2	-1024.0688
C_3	+224.5627
C_4	-28.4080
C_5	+2.0697
C_6	-0.0805
C_7	+0.0013
$R > 1.6R_0$	
D_0	234.88

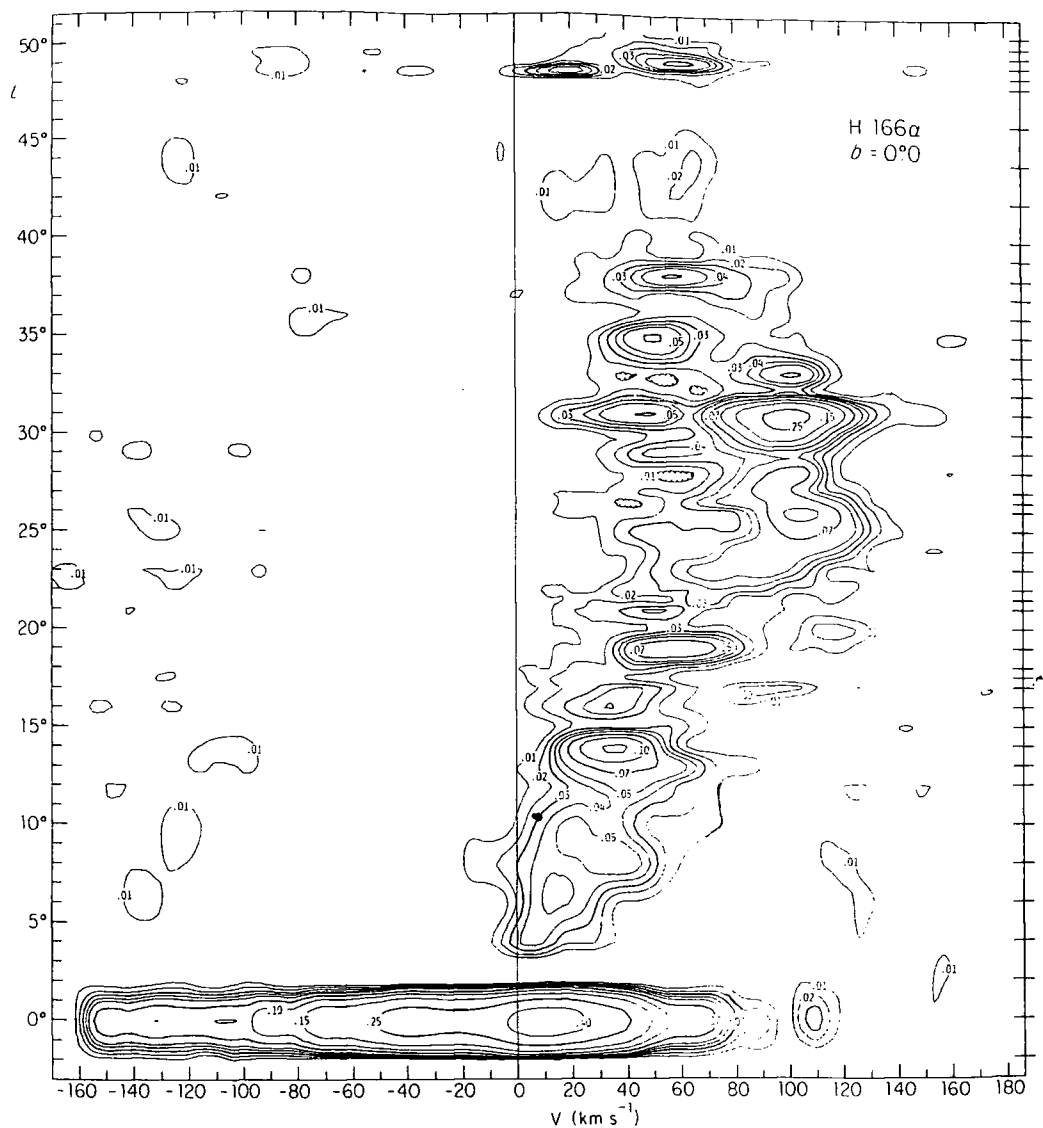


Figure 4.8: Distribution of recombination line ($H166\alpha$) emission in the first quadrant of Galactic longitude as measured by Lockman(1976). The emission is given terms of Antenna Temperature in velocity-longitude coordinates. Contours are drawn every 0.01 K from 0.01 K to 0.05 K and at 0.07, 0.10, 0.15, 0.25, and 0.40 K.

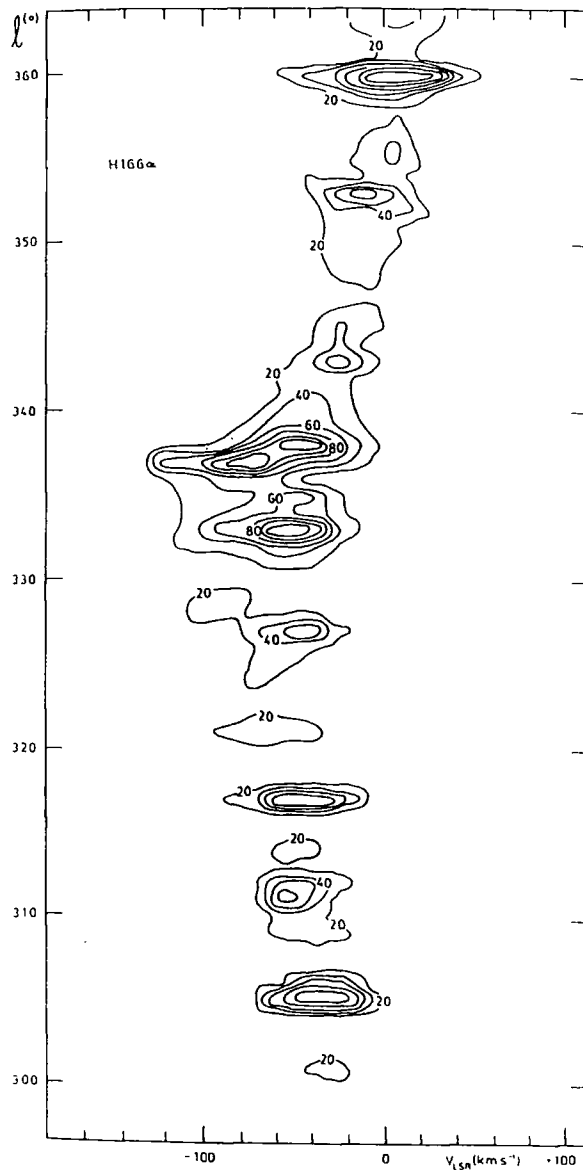


Figure 4.9: Distribution of recombination line (H166 α) emission in the fourth quadrant of Galactic longitude as measured by Cersosimo(1989). The emission is given terms of brightness temperature in velocity-longitude coordinates. The contour interval is 0.02 K.

In principal the rotation curve together with the above relations allows these distributions of recombination line brightness temperature as a function of l and v to be converted to a map of the distribution of $\langle n_e^2 \rangle$ in the Galactic plane. Such a distribution is shown in Fig 4.10 where the rotation curve of Clemens under the assumption of purely circular motion of gas about the Galactic centre is used to convert velocity to distance. Note that we have ignored the emission within 5° of the Galactic centre as this clearly shows considerable non-circular motion. For each longitude equal contributions to the brightness temperature are assumed to be made from gas at the far and near points that have the same velocity along the line of sight. It is apparent, however from this figure that the velocity resolutions of the recombination line surveys are not sufficient to assign the gas to spiral arms of realistic width. The faintness of the emission is the reason why such a broad velocity resolution was chosen.

From $H\alpha$ pictures of other Sbc galaxies, we would expect the main part of the HII emission of the Milky Way galaxy to be concentrated in arms with FWHM ≈ 0.5 kpc. Therefore we have assumed that for each longitude, the emission comes from the spiral arm nearest to the position which is indicated by its velocity. And we also assumed that the mean electron density is highest in the centre of the arms and gradually declines according to a Gaussian distribution with FWHM = 0.5 kpc when it is far from the centre. We therefore need additional information about the position of the spiral arms of thermal electrons. One model that we can take is that the arms coincide with the peaks of the spiral arms of synchrotron emissivity that we have already deduced in Chapter 3. We shall label this the 'synchrotron spiral arm' model. The distribution of $\langle n_e^2 \rangle$ according to this model is shown in Fig. 4.11.

It is certainly the case that for some galaxies, such as M51, the nonthermal radio spiral arms coincide with the arms picked out by HII regions. For others

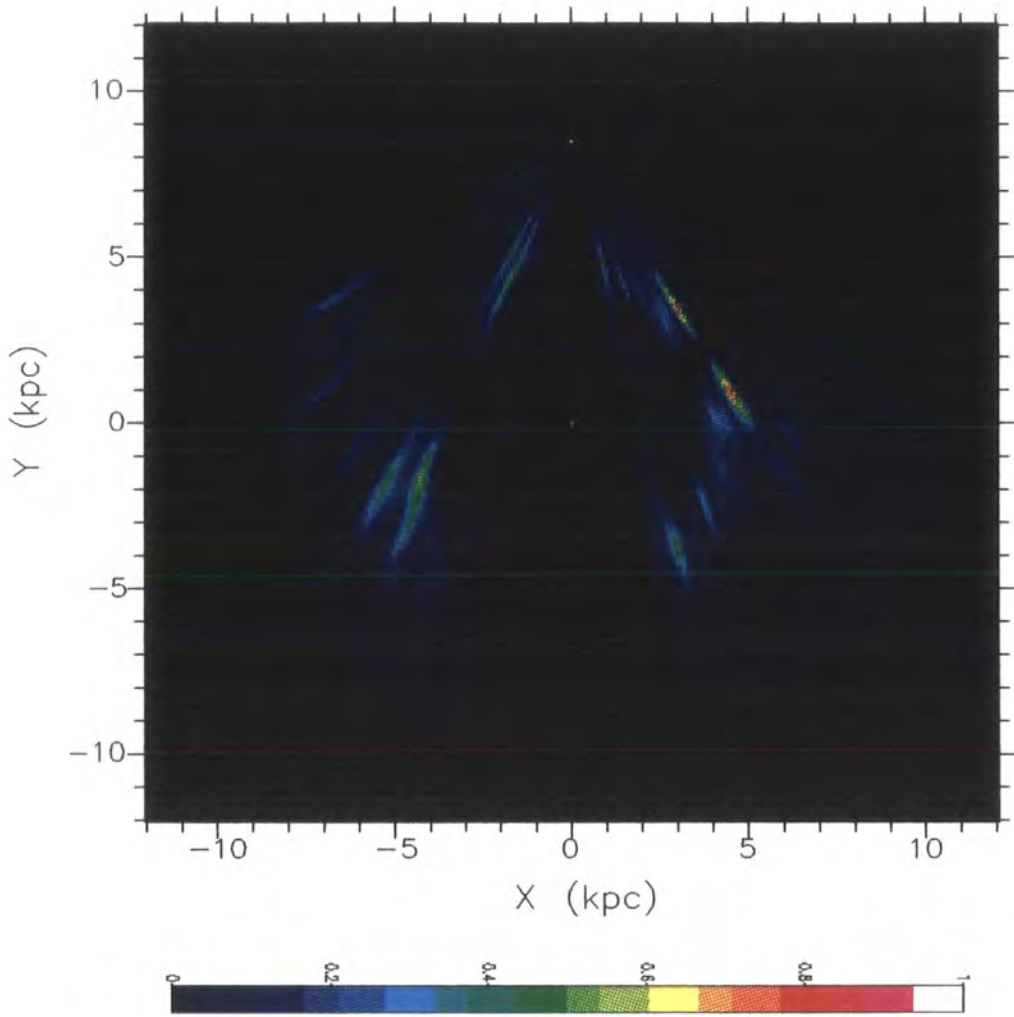


Figure 4.10: The distribution of mean square electron density, $\langle n_e^2 \rangle$, derived from the longitude-velocity distribution of H166 α emission by way of the Galactic rotation curve. The range of density is from 0 to 3 cm^{-6} . The position of the Galactic centre is [0,0] and the Sun is [0,8.5].

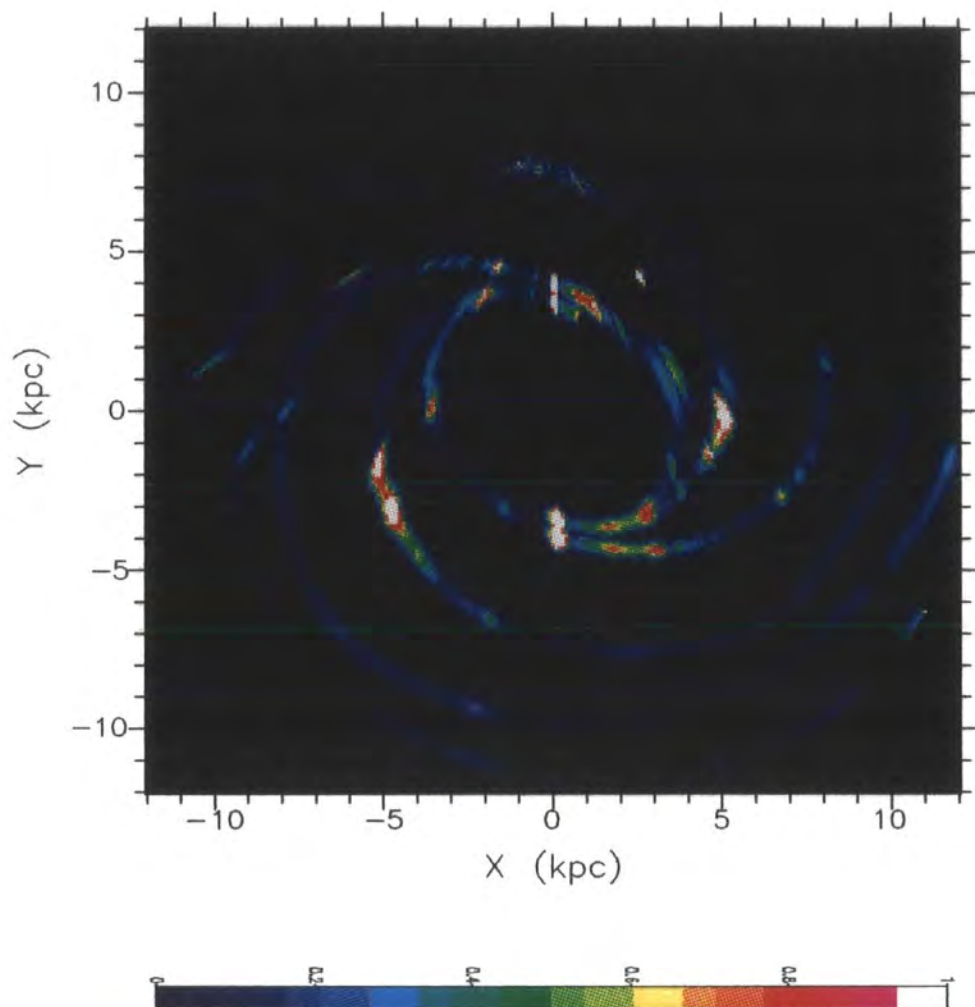


Figure 4.11: The distribution of mean square electron density, $\langle n_e^2 \rangle$, derived as for Fig.4.10 but with the constraint that the electrons fall within the 'synchrotron spiral arms'. The range of density is from 0 to 3 cm^{-6} .

it is not so clear. As an alternative model we take it that the relevant arms are the spiral arms in the distribution of thermal electron density, n_e , as derived from pulsar dispersion measures by Taylor and Cordes(1993), referred to from now on as TC.

4.3 The distribution of electron density according to TC

Taylor and Cordes(1993) have modelled the distribution of mean electron density, $\langle n_e \rangle$, to fit the dispersion measures of pulsars for which there is independent information on their distances. Currently there are upwards of 550 known pulsars. Of these there are constraints on the distance for about 70. These constraints are generally the presence or absence of 21 cm absorption lines in their radio continuum spectra at velocities corresponding to those of HI spiral arms along the line of sight. If the absorption line is present the pulsar lies beyond the arm, if absent it lies in front.

TC started from the same Georgelin and Georgelin spiral arm pattern that was the starting point for our synchrotron arms. In the TC model, arm 3 has been moved slightly inward in regions inside the Sun, as shown in Fig 4.12, to correspond with the improved measurements of Downes et al.(1980) and also arm 4 has been extended at the outer end according to data by Caswell and Haynes(1987). The coordinates of the spiral arms are shown in table 4.2. Fig. 4.12 shows $\langle n_e \rangle$ distributed according to this pattern.

The electron density at any point according to the TC model(Fig 4.13) is the sum of contributions from four components; 1) an outer disk(n_1), 2) the inner galaxy(n_2), 3)the spiral arms(n_a) and 4)the Gum nebula(n_g):

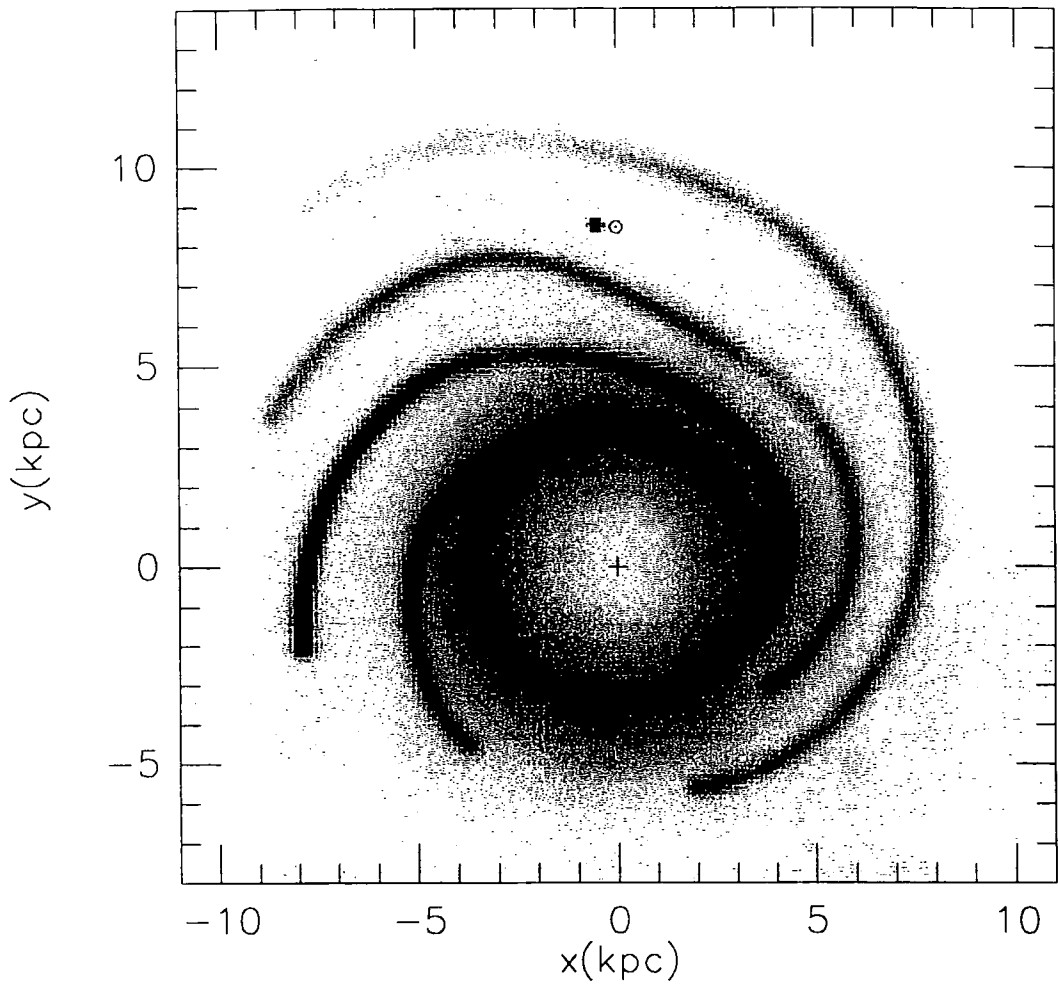


Figure 4.12: Grey-scale picture of the distribution of mean thermal electron density $\langle n_e \rangle$ in the Galactic plane as modelled by Taylor and Cordes(1993) from pulsar dispersion measures. The maximum density in the arms is $\sim 0.18 \text{ cm}^{-3}$: the density near the sun is $\sim 0.019 \text{ cm}^{-3}$.

Table 4.2: Coordinates of the spiral arms in TC model

ARM 1		ARM 2		ARM 3		ARM 4	
θ	r (kpc)	θ	r (kpc)	θ	r (kpc)	θ	r (kpc)
164°	3.53	63°	3.76	52°	4.90	20°	5.92
200°	3.76	120°	4.56	120°	6.27	70°	7.06
240°	4.44	160°	4.79	170°	6.49	100°	7.86
280°	5.24	200°	5.70	180°	6.95	160°	9.68
290°	5.36	220°	6.49	200°	8.20	180°	10.37
315°	5.81	250°	7.29	220°	8.89	200°	11.39
330°	5.81	288°	8.20	252°	9.57	223°	12.08

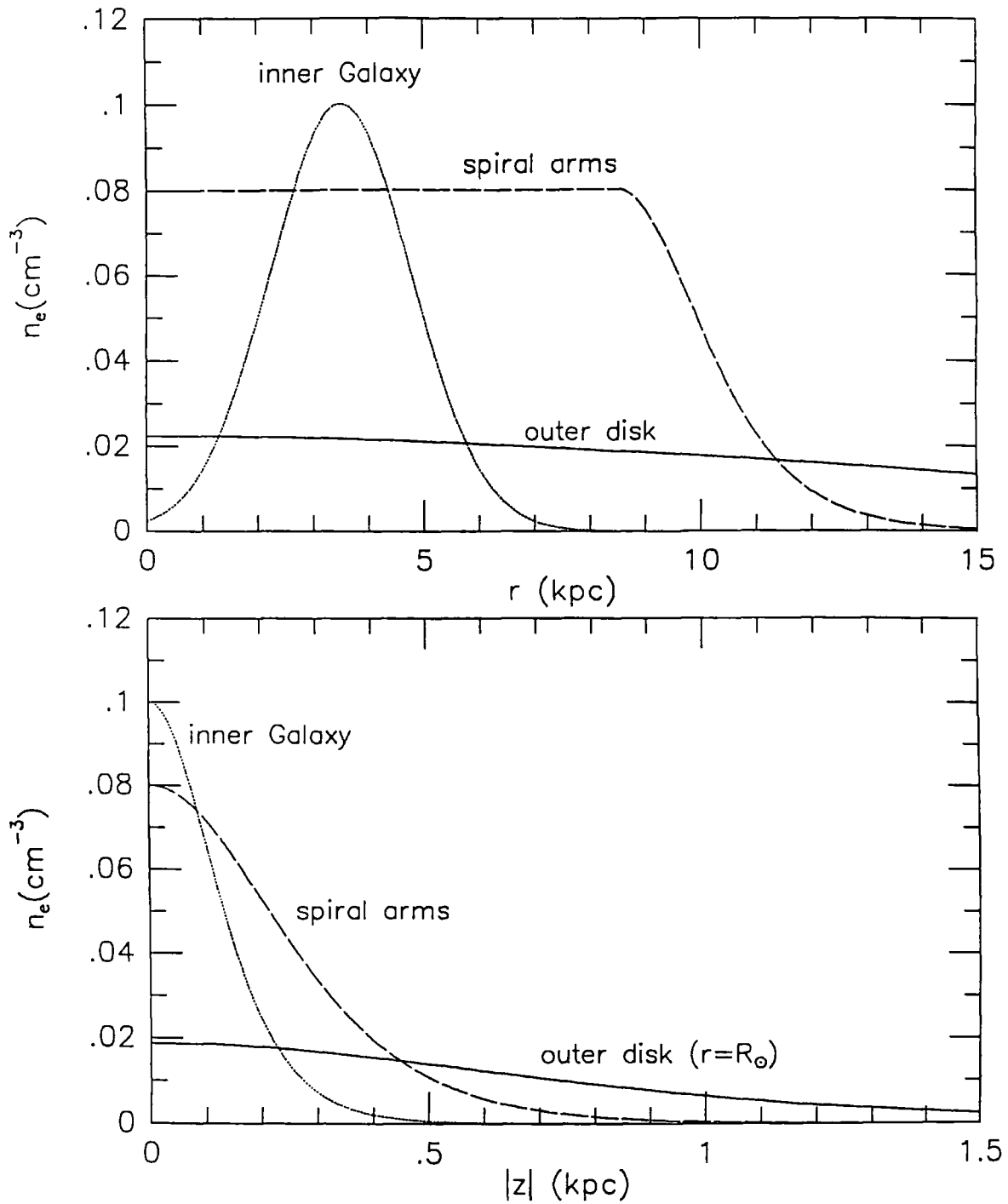


Figure 4.13: Mean thermal electron density as functions of galactic radius, r , and distance from the galactic plane, z as modelled by Taylor and Cordes(1993).

$$n_e(x, y, z) = n_1 g_1(r) \operatorname{sech}^2(z/h_1) + n_2 g_2(r) \operatorname{sech}^2(z/h_2) + n_a \operatorname{sech}^2(z/h_a) \sum_{j=1}^4 f_j g_a(r, s_j) + n_G g_G(u) \quad (4.9)$$

where $r = (x^2 + y^2)^{1/2}$ is the galactocentric distance projected onto the plane, h_i is the scale height for component i and scale factors f_j are defined by

$$f_1 = f_4 = 1 \quad (4.10)$$

$$f_2 = \begin{cases} 1 & , \theta < 215^\circ \\ 1 + (\theta - 215^\circ)/20^\circ & , 215^\circ < \theta < 235^\circ \\ 2 & , \theta > 235^\circ \end{cases} \quad (4.11)$$

$$f_3 = \begin{cases} (3 + \cos[2\pi(\theta - 120^\circ)/40^\circ])/4 & , 120^\circ < \theta < 160^\circ \\ 1 & , \text{elsewhere} \end{cases} \quad (4.12)$$

Here θ is an angle measured counterclockwise from the negative y direction. And the functions g_1, g_2, g_a and g_G are defined by

$$g_1(r) = \operatorname{sech}^2(r/A_1) / \operatorname{sech}^2(8.5/A_1) \quad (4.13)$$

$$g_2(r) = \exp \left\{ - \left[\frac{(r - A_2)}{1.8} \right]^2 \right\} \quad (4.14)$$

$$g_a(r, s_j) = \begin{cases} \exp[-(s_j/w_a)^2] \operatorname{sech}^2[(r - A_a)/2.0] & \text{for } r > A_a \\ \exp[-(s_j/w_a)^2] & r \leq A_a \end{cases} \quad (4.15)$$

$$g_G(u) = \begin{cases} \exp[-((u - 0.13)/0.05)^2] & , u > 0.13 \text{ kpc} \\ 1.0 & , u \leq 0.13 \text{ kpc} \end{cases} \quad (4.16)$$

where s_j is a distance on the plane from the nearest point on the axis of spiral arm j and u is the distance from the Gum Nebula. And other parameters are shown in Table 4.3.

Table 4.3: Parameters of the electron density model taken from Taylor and Cordes(1993)

Parameter	Estimated value	Adopted value
$n_1 h_1 (\text{cm}^{-3} \text{kpc})$	0.0165 ± 0.0006	0.0165
h_1 (kpc)	0.88 ± 0.06	0.88
A_1 (kpc)	≥ 20	20
F_1	$0.36^{+0.30}_{-0.10}$	0.4
$n_2 (\text{cm}^{-3})$	0.10 ± 0.03	0.1
h_2 (kpc)	0.15 ± 0.05	0.15
A_2 (kpc)	3.7 ± 0.3	3.5
F_2	43^{+30}_{-13}	40
$n_a (\text{cm}^{-3})$	0.084 ± 0.008	0.08
h_a (kpc)	0.3 ± 0.1	0.3
w_a (kpc)	0.3	0.3
A_a (kpc)	8.5	8.5
F_a	6^{+5}_{-2}	6.0

From table 4.3, we can see the parameter F is a fluctuation parameter which differs widely for the various galactic components, increasing nearly 100 times from outer to the inner of the galaxy. It is not so clear how to obtain these fluctuation parameters so we cannot use this electron density distribution directly to obtain the distribution of mean square electron density. In other words $\langle n_e \rangle$ from the dispersion measures cannot be directly used to find $\langle n_e^2 \rangle$ because there is a factor which we call the 'filling factor', f , involved. The true electron density, $n_e(s)$, is related to the mean electron density, $\langle n_e(s) \rangle$:

$$\langle n_e(s) \rangle = f(s)n_e(s) \quad (4.17)$$

and similarly

$$\langle n_e^2(s) \rangle = f(s)n_e^2(s) \quad (4.18)$$

The relationship between $\langle n_e \rangle$ and $\langle n_e^2 \rangle$ in terms of the filling factor as:

$$f(s) = \frac{\langle n_e(s) \rangle^2}{\langle n_e^2(s) \rangle} \quad (4.19)$$

For lines of sight towards the inner parts of the Galaxy the values of $\langle n_e^2 \rangle$ required to account for the thermal continuum emission are in general much larger than the squares of the $\langle n_e \rangle$ values got from pulsar dispersion measures. Thus the filling factor $f(s)$ is clearly $\ll 1$ and varies from place to place.

We cannot therefore use the TC model for the $\langle n_e \rangle$ distribution directly to predict the absorption. Instead we simply use the spiral arm pattern of TC to define the positions of the arms of ionised gas and assign $\langle n_e^2 \rangle$ derived from the recombination line brightness temperature to the nearest arm as indicated by its Doppler shift. The resulting distribution, the 'TC spiral arm' model is shown in Fig. 4.14

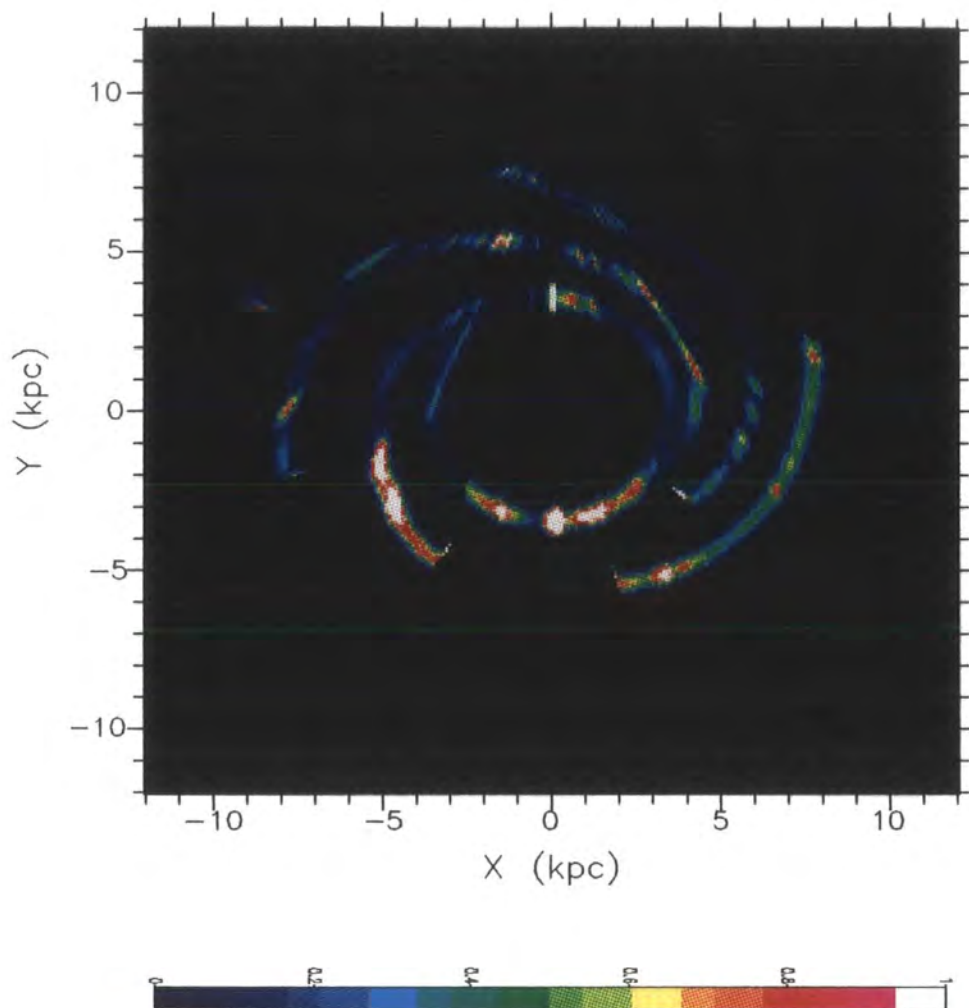


Figure 4.14: The distribution of mean square electron density, $\langle n_e^2 \rangle$, derived as for Fig.4.10 but with the constraint that the electrons fall within the 'TC spiral arms'. The range of density is from 0 to 3 cm⁻⁶.

4.4 The predicted and observed absorption

4.4.1 Calculation of the predicted absorption

It follows from sections 4.2 and 4.3 that we have two models for the distribution of $\langle n_e^2 \rangle$ along lines of given l and are able to calculate brightness temperatures in those directions taking into account absorption. The recombination line surveys are restricted to $b = 0$ and give no information on the 3-dimensional distribution of $\langle n_e^2 \rangle$ so our comparison can only be with the profile along the plane. We still need, however, to convolve the predictions to a 51' HPBW so a calculation of, at least an approximate, 2-dimensional variation of absorption is needed. To do this we assume that $\langle n_e^2 \rangle$ varies with distance, z , from the plane as $\text{sech}^2(z/h)$ where $h = 0.08$ kpc. This represents the distribution of molecular gas in the inner Galaxy to which the ionised gas that we are considering is expected to be related. We note that such a distribution has a FWHM of 140 pc, which means that the beams used in the two recombination line surveys would lie within the ionised gas layer over the full path length in the Galaxy. We implicitly assumed this in our derivation of $\langle n_e^2 \rangle$ from the recombination line brightness temperatures.

To calculate the brightness temperature with absorption we divide the chosen line of sight into steps of length $\Delta s = \frac{0.05}{\cos b}$ kpc. We start the calculation at the furthest point on the line of sight. The brightness temperature after the n th step then follows from equation 2.37 as

$$T_n = T_{n-1} \exp(-\Delta\tau) + T_e(1 - \exp(-\Delta\tau)) + \Delta T \frac{(1 - \exp(-\Delta\tau))}{\Delta\tau} \quad (4.20)$$

where the optical depth of the step is

$$\Delta\tau = k \frac{\langle n_e^2 \rangle \Delta s}{\text{cm}^{-6} \text{ kpc}}$$

with $k = 0.6243$ and 0.8431 for 34.5 MHz and 29.9 MHz respectively. The first term on the RHS gives the intensity from the previous step, attenuated by the step. The

second and third terms give the thermal and nonthermal components of emission from the step in the presence of absorption. At ~ 30 MHz and with $T_e = 7000$ K the synchrotron emission from the step $\Delta T \gg T_e \Delta \tau$ so the second term is much smaller than the third.

To obtain the corresponding relation for negligible absorption let $\Delta \tau \rightarrow 0$ then $T_n = T_{n-1} + \Delta T$. After the final step the ratio of the brightness temperature with absorption to that without gives the effective transmitted fraction which may be compared with observation.

Fig. 4.15 shows the relative contributions from points along a particular line of sight to the brightness temperatures, with and without absorption, in that direction. From the upper line one can see how much of the emission comes from the arm regions and how much from the interarms. From the lower line it is apparent that, for that particular line of sight, the detailed structure of the arms beyond ~ 10 kpc has only a minor effect on the total brightness temperature.

The same information is contained in Figs. 4.16 and 4.17 but this time for all longitudes in the inner Galaxy. Fig. 4.16 is the 'no absorption' case. It can be noted that in directions where the line of sight from the sun meets a spiral arm tangentially the apparent brightness of the arm is reduced. This is the effect of the regular field component which lies along the line of sight at that point and therefore gives a minimal contribution to the synchrotron emission as observed from the sun. This effect would not be present, of course, for an observer viewing the Galaxy face on where the regular field would always be perpendicular to the line of sight

From Fig. 4.17, the picture with absorption, one can judge how much the details of the more distant spiral arms contribute to the predicted absorption.

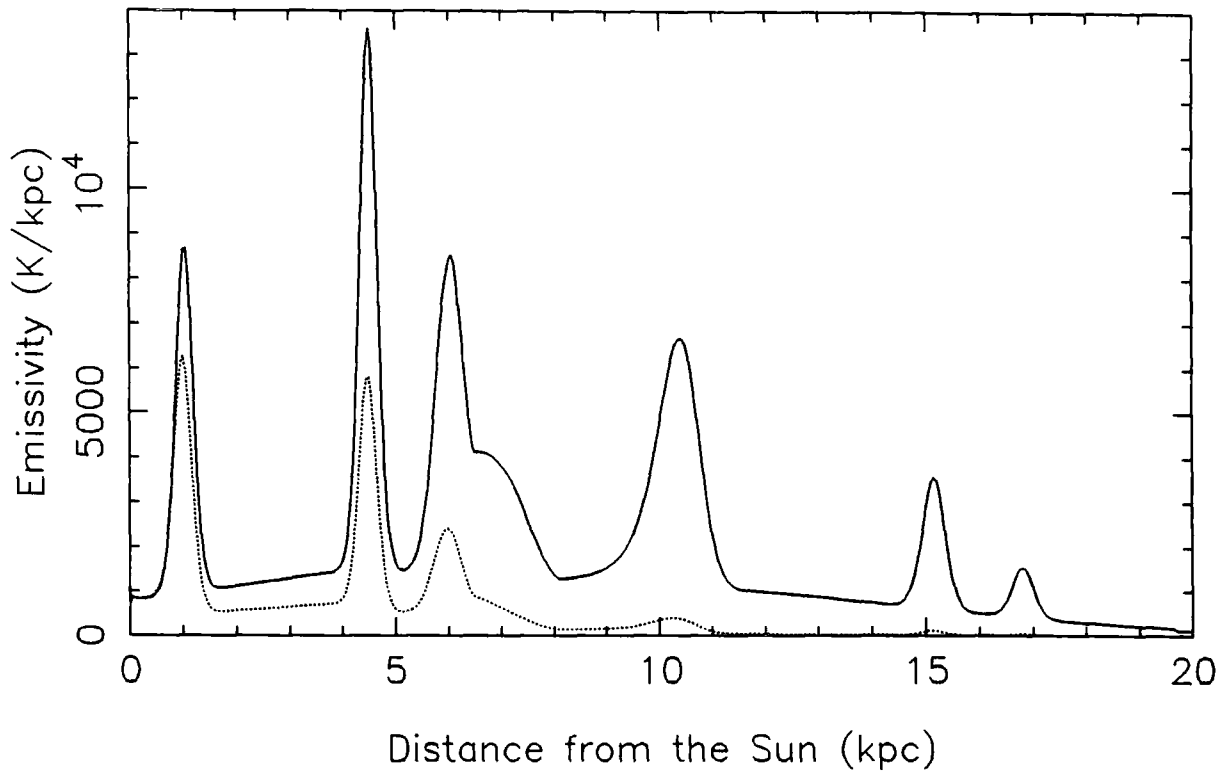


Figure 4.15: An example of the contributions of points along the line of sight $l = 330^\circ$, $b = 0^\circ$ to the total brightness temperature in that direction. The upper line shows the contributions with no absorption. The lower line shows the contribution after absorption at 29.9 MHz by thermal electrons distributed according to the 'synchrotron spiral arms' model.

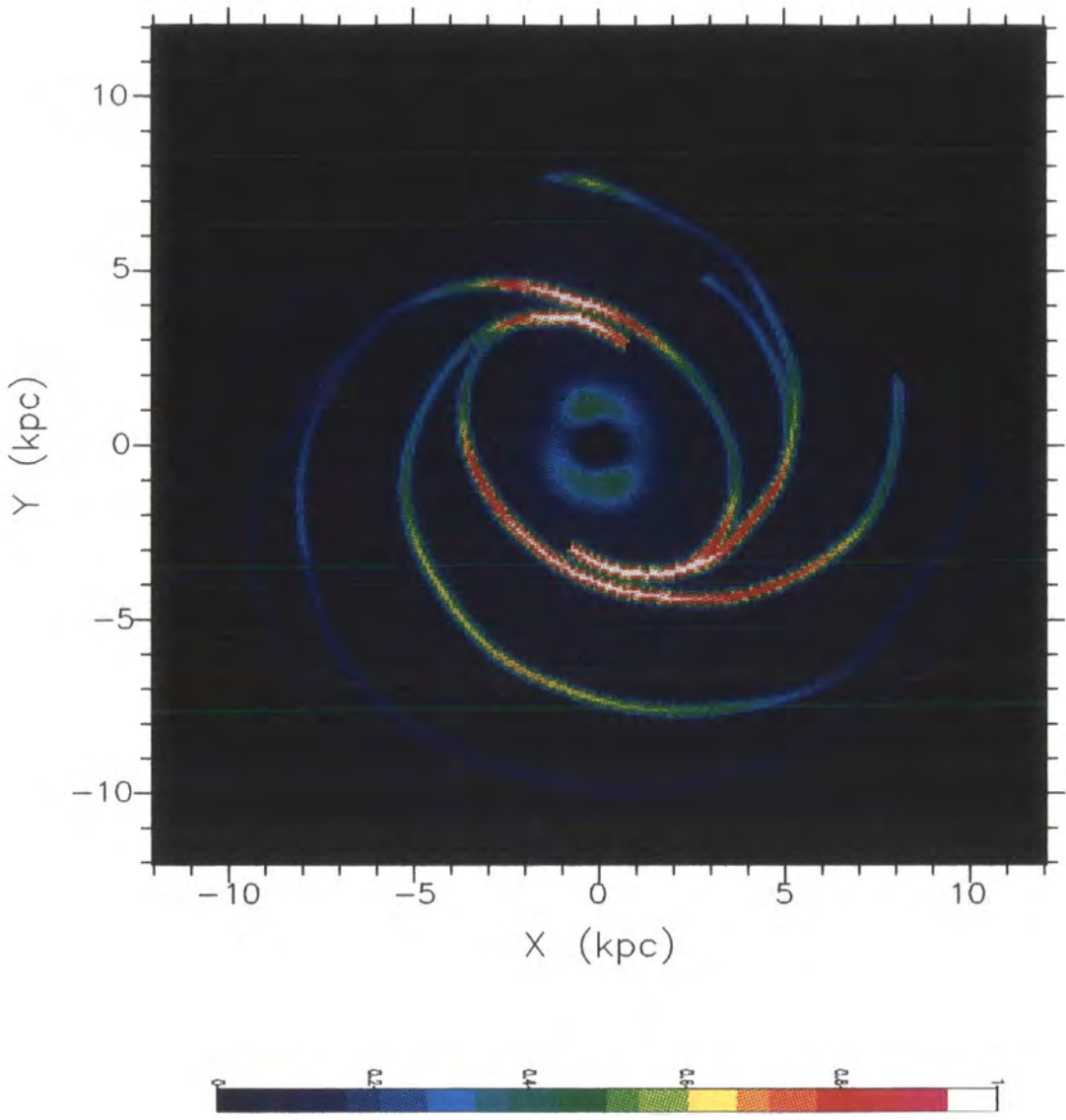


Figure 4.16: The contributions of points along the line of sight to the predicted longitude profile of brightness temperature as observed from the Sun's position. The range of the emissivity is from 0 to 10000 K/kpc.

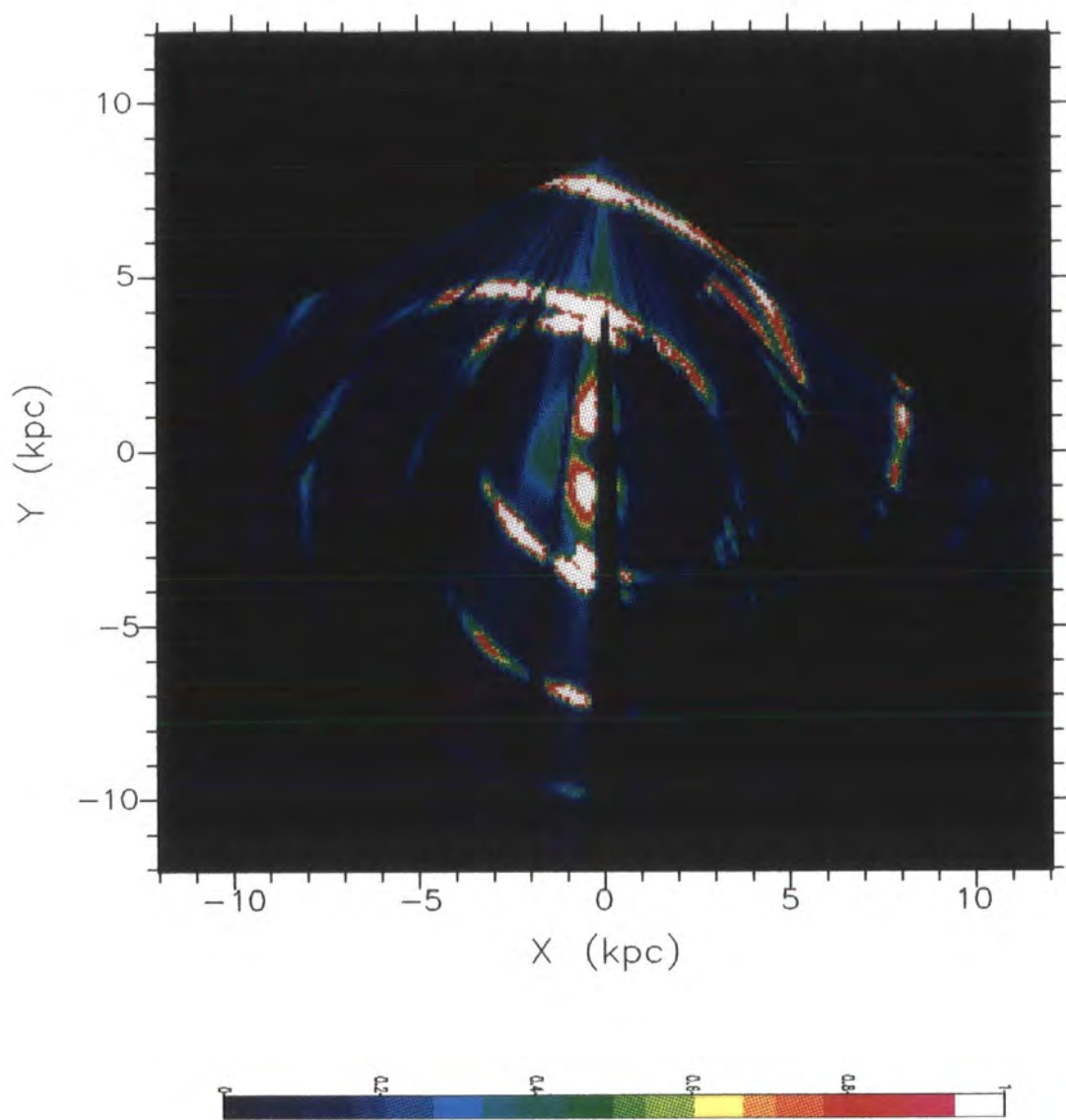


Figure 4.17: As for Fig.4.16 but with the inclusion of absorption by thermal electron distributed according to the 'synchrotron spiral arms' model. The range of the emissivity is from 0 to 2000 K/kpc.

4.4.2 Comparison with the 'observed' absorption

We now come to the comparison of the predicted and observed absorption. Of course it is not possible to turn off the absorption for the low frequency observations. What we have to do is to predict what the observations would look like if there was only the nonthermal component with no absorption. For this we use the nonthermal component of the 408 MHz emission as obtained in Chapter 2 and scale it to the equivalent brightness temperature at 34.5 or 29.9 MHz. We have to assume that the brightness temperature spectral index of the nonthermal component is uniform over the region of interest, which is equivalent to assuming that the cosmic ray electron spectral index is constant over that region. To determine this brightness temperature spectral index we make use of the fact that the thermal emission in quadrants 1 and 4 of Galactic Longitude is confined to within 5° in latitude of the Galactic plane, as can be seen in Figs. 2.6a and 2.6b. This means that, for $|b| > 5^\circ$, there is no thermal component and no absorption and the ratio of low and high frequency brightness temperatures gives the required index.

For the first quadrant the longitude range of interest is $5^\circ < l < 50^\circ$, the region covered by the recombination line survey, excluding that within 5° of the galactic centre where non-circular velocities are too large. In this region we take the ratio of the 34.5 MHz and the 408 MHz nonthermal brightness temperatures and find that its mean value for $7.0^\circ < |b| < 8.3^\circ$ is 423. We therefore multiply the whole of the 408 MHz nonthermal brightness temperature map by this value in order to obtain a prediction of what the observed unabsorbed brightness temperatures would be at 34.5 MHz. Finally by dividing this into the directly observed 34.5 MHz map, after convolution to a HPBW of $51'$ and taking the cut along $b = 0^\circ$ we obtain the 'observed' transmission of 34.5 MHz continuum emission as shown by the solid lines in the two plots in Fig. 4.18. The ratio of 423 implies an effective Temperature spectral index between 408 and 34.5 MHz of 2.45.

The same procedure is applied to the 29.9 MHz data in the 4th quadrant. In this case the longitude range of interest is $300^\circ < l < 355^\circ$ and the mean ratio of the 29.9 MHz and the 408 MHz nonthermal brightness temperatures for $7.0^\circ < |b| < 8.3^\circ$ is 1280. The resulting 'observed' transmission of 29.9 MHz continuum emission is shown by the solid lines in the two plots in Fig. 4.19. The ratio of 1280 implies an effective Temperature spectral index between 408 and 29.9 MHz of 2.73. We do not believe that the spectral indices are really so different in the two quadrants and attribute this to differences in the absolute calibration of the two surveys. As we have already applied a correction to the calibration of the 34.5 MHz map to give agreement with the 38 MHz survey we believe that the fault lies in the calibration of the older 29.9 MHz survey. If this simply affects the overall temperature scale it does not change the values of the 'observed' transmission that we have derived.

The dotted lines in Figs 4.18 and 4.19 are the predicted transmissions discussed in the previous section with the pair of plots in each figure. One can see that there is agreement in the general level of the predicted and observed transmissions and the maxima and minimum usually occur at the same longitudes. This confirms that the absorption model of the synchrotron emissivity in the Galactic plane is broadly correct. There is not a great deal of difference between the predictions of the 'synchrotron spiral arms' model and the 'TC spiral arms model' and there is no overall best fit. For instance in the region $35^\circ < l < 40^\circ$ the 'synchrotron' appears favoured while for $28^\circ < l < 35^\circ$ the 'TC' model fits better. In some regions one sees that neither of the predicted lines agree very well with the observed one. We shall discuss in the final chapter some of the simplifying assumptions and other factors that may cause this. The main effect on the predicted absorption, however, is likely to be our having to deal with the distance ambiguity by assuming that the H166 α emission comes from the near and far points equally. This is a reasonable assumption overall but can give the wrong result at any particular longitude. If all of this

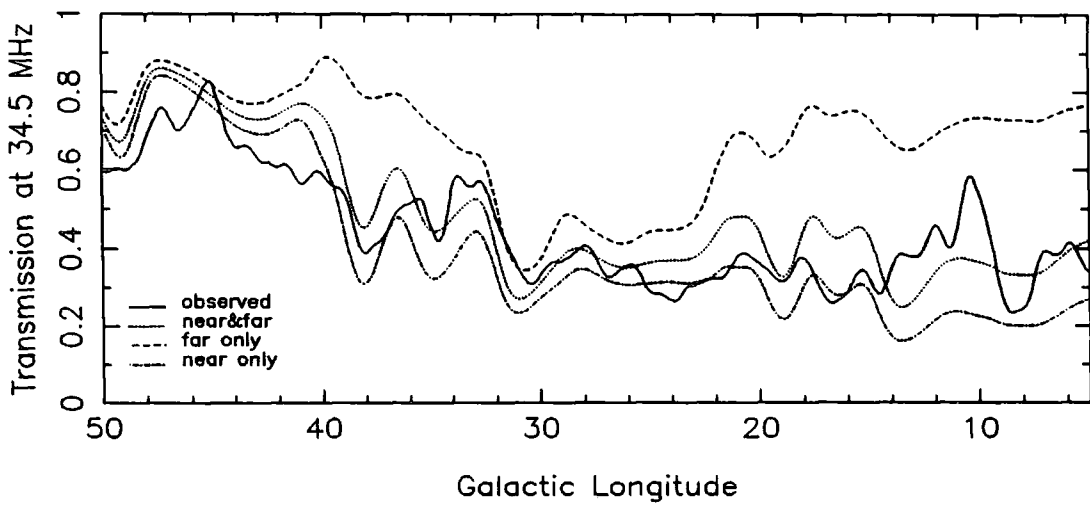
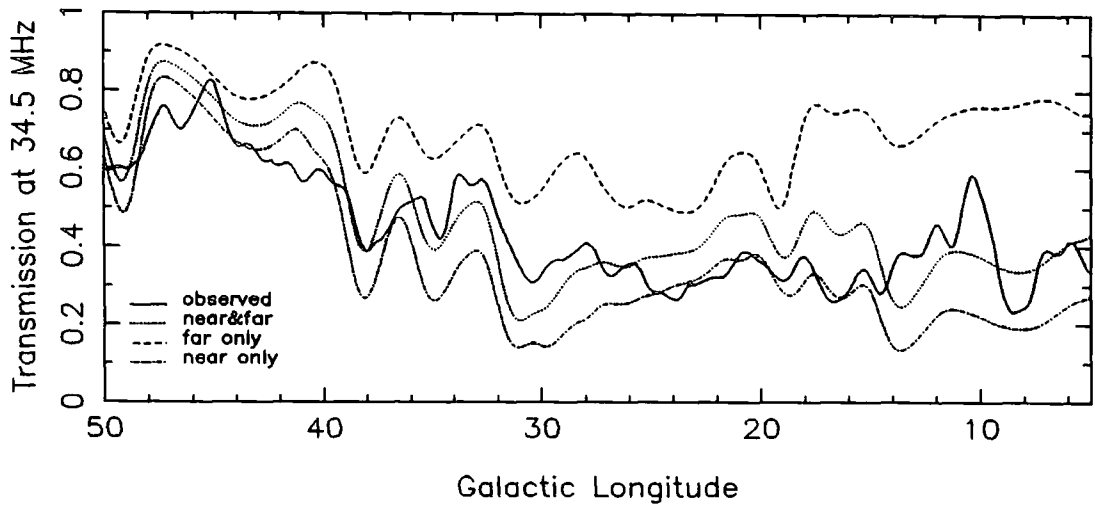


Figure 4.18: The 'observed' transmission of 34.5 MHz continuum emission (solid line) compared with the predicted transmission. Three cases are shown concerning the treatment of the distance ambiguity in converting recombination line Doppler shift to the distance of thermal electrons: (i) all at the far distance (dashed line), (ii) half at the far and half at the near distance (dotted line), (iii) all at the near distance (dash-dot line). The upper plot is for thermal electron following the 'synchrotron spiral arms' model. The lower one is for the 'TC spiral arms' model.

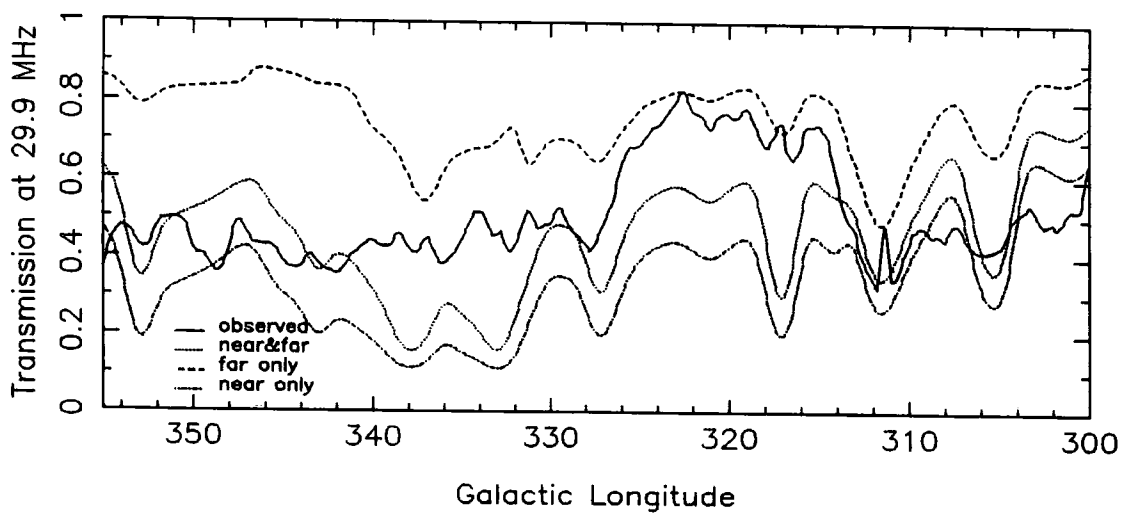
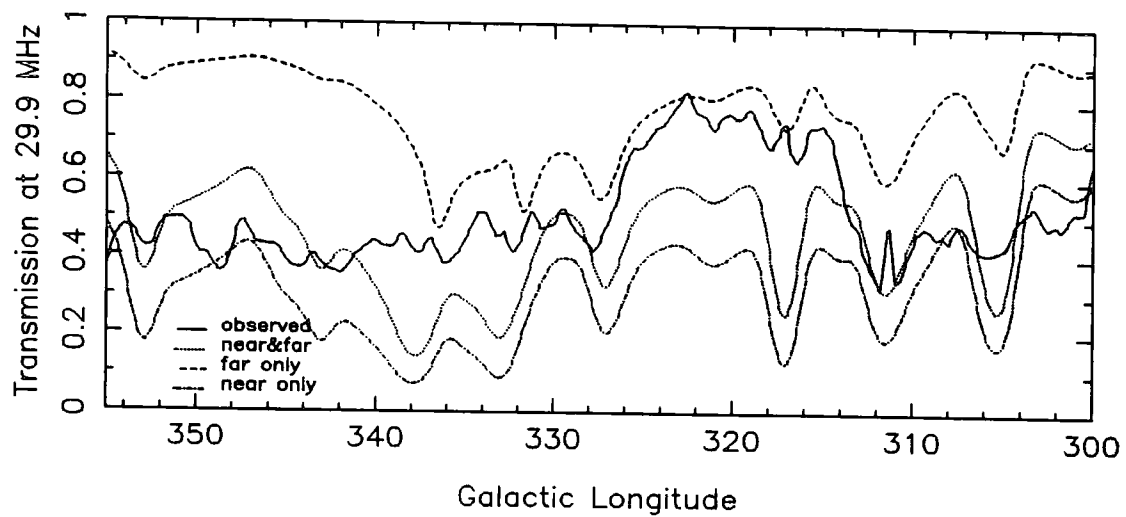


Figure 4.19: The 'observed' and predicted transmission as for Fig.4.18 but concerning the 29.9 MHz emission.

emission in fact comes from the near point the absorption will be stronger than if it all comes from the far point. To show the full range of possible absorptions at each longitude we have reconstructed the two distributions of $\langle n_e^2 \rangle$ first with all of the ionised emission at the far points and secondly with all of the ionised hydrogen at the near points. We have then recalculated the transmission. The results are shown as the dashed and dash-dot lines respectively in the two figures. In general then the 'observed' transmission lies between the predicted transmissions for the near and far cases.

Chapter 5

Conclusion

5.1 Summary

In this final chapter we summarise our results, discuss some of the overall properties of the Galaxy and consider possible future developments.

The derivation of our model of the distribution of synchrotron emissivity in the Galaxy is described in Chapter 3. The model is defined by the expressions and parameters given in Table 3.2 with the spiral arm structure plotted in Fig. 3.6 and tabulated in Table 3.1. One should make clear that as this is based on a radio survey which has HPBW of 51' it can represent detail down only to a scale size of typically 130 pc. This is roughly the thickness of the molecular gas layer in the inner Galaxy but is considerably smaller than the deduced thickness of the synchrotron emitting disk. We had started with a model derived by Broadbent which was then modified in a number of ways. Firstly we adopted the, now standard, distance to the Galactic center of 8.5 kpc. Then we took into account the new evidence of a Galactic bar (Blitz, 1993). We did not try to model the synchrotron emission from the bar itself because the thermal and non-thermal separation technique cannot be applied so close, in angular distance, to the Galactic centre as the region of the bar and also the prediction of how the magnetic field alignment at the center of the Galaxy is affected by the bar is not clear. The bar does, however, have implications

for the geometry of the spiral arms as they approach the Galactic centre and this was taken into account.

In view of the evidence from some nearby external galaxies to the contrary, we tested our model's assumption that the magnetic field suffers a net alignment along the spiral arms by compression (the Y-factor of equation 3.7). With this factor omitted, however, the profiles of the arms viewed tangentially gave a significantly worse fit to the observations than for the original model. The fit could have been restored to a certain extent by reducing the compression in the arm but then one would have the problem of accounting for the observed contrast of star formation rate between the arm and interarm regions. We conclude that for our Galaxy the disruption of the magnetic field by supernova explosions and the stellar winds of O stars does not overcome the alignment due to compression.

Our model is symmetric above and below the Galactic plane and does not include Loops I, II and III, as designated by Berkhuijsen et al. (1971), which are taken to be old supernova remnant shells of the order of 100 pc in diameter but sufficiently nearby to subtend large angles at the sun. The North Polar Spur, which forms part of the arc of loop I is the most prominent of these features and can be seen extending from the Galactic plane at around Dec. $+10^\circ$ to $+20^\circ$ in Fig. 4.3. No account was taken of the warp of the Galactic disk as observed in the HI gas layer outside the solar galactocentric radius. As shown by Phillipps et al. (1981b) because of the fall off in synchrotron emissivity outside the sun this has a minor effect on the latitude profiles of emission in the second and third quadrants of longitude. As no arms are viewed tangentially in these quadrants the longitude profile is rather insensitive to changes in the positions of arms there. This together with the fact that we normalise the model to fit the observed emission in the anticentre direction meant that it was unnecessary to make any adjustment to the position of the arms outside the sun from those in the Broadbent model.

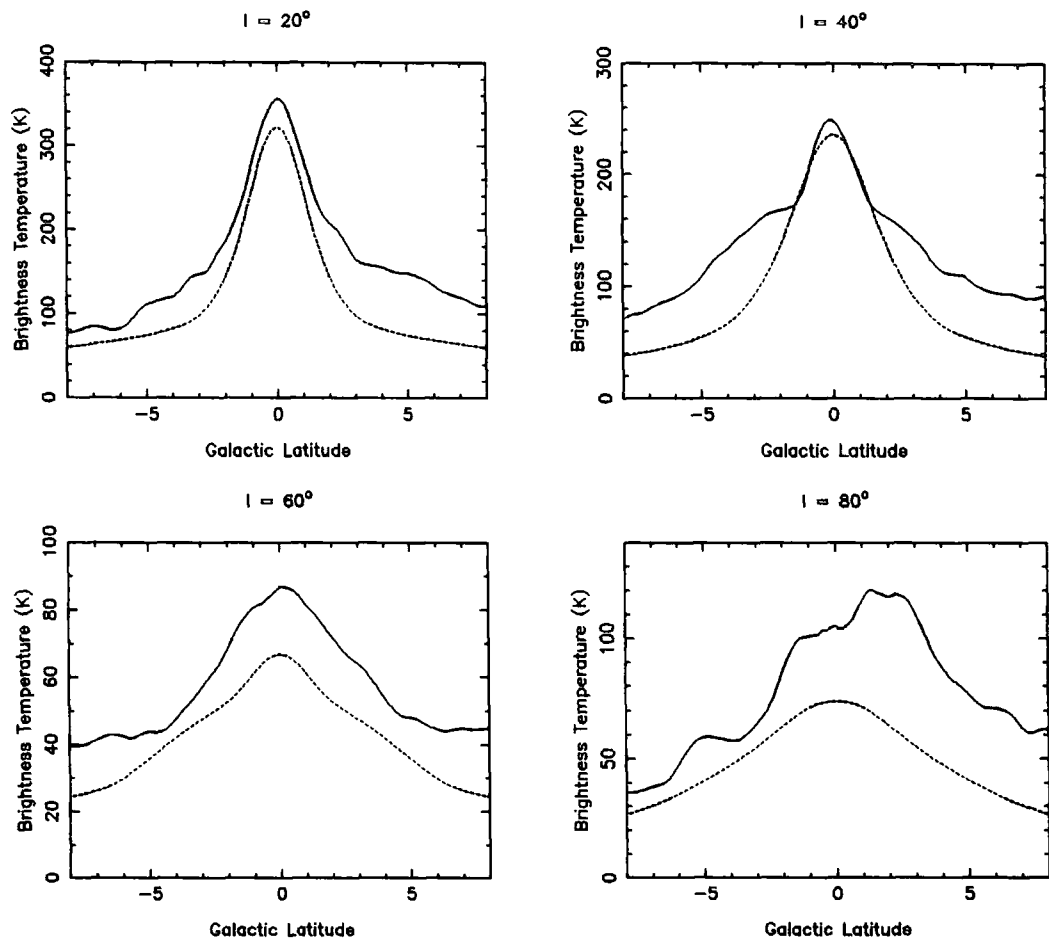


Figure 5.1: Latitude cuts across the Galactic plane showing the observed non-thermal emission at 408 MHz (solid line) and that predicted by our model (dotted line). (Continued on next page.)

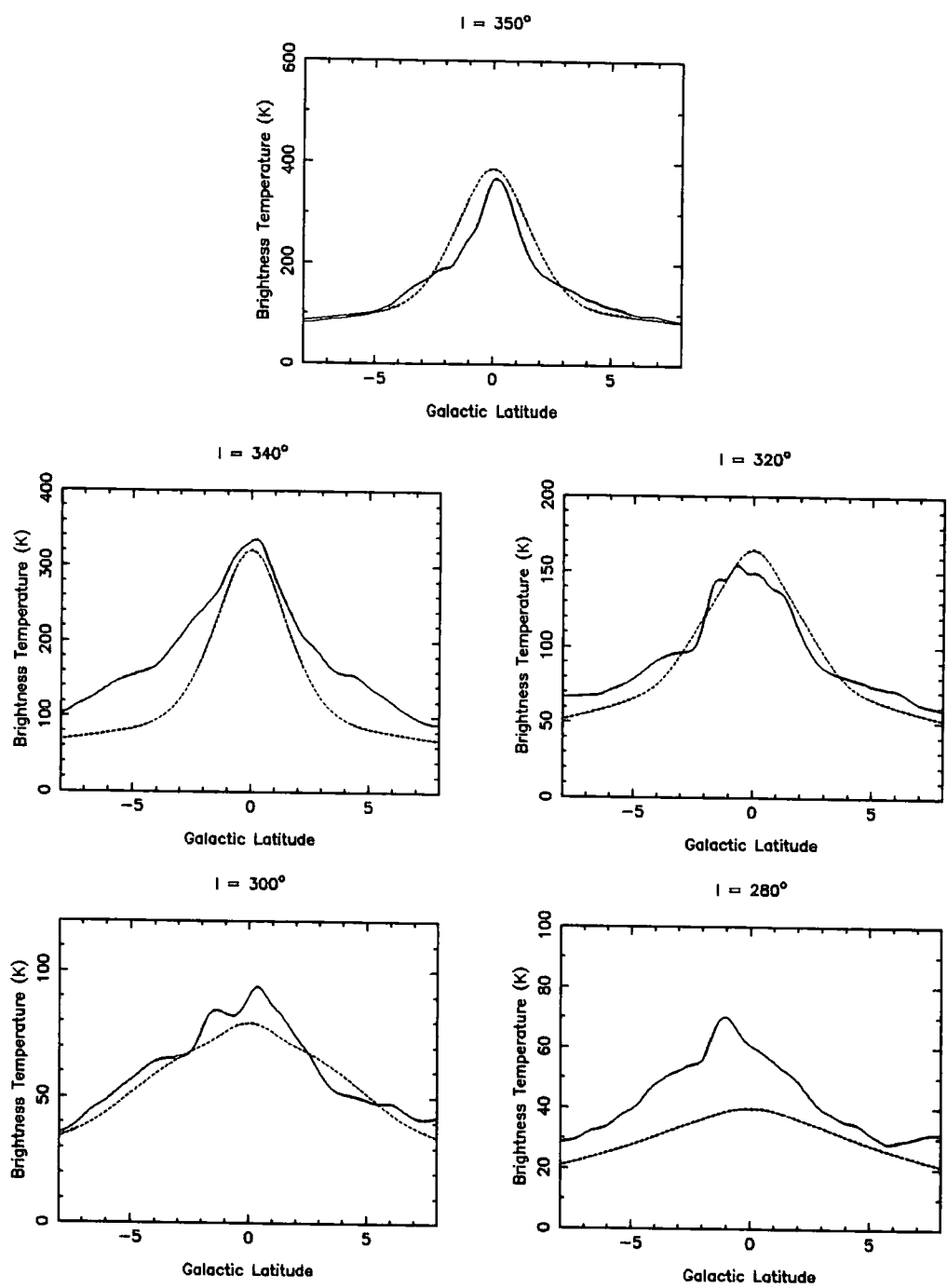


Figure 5.1: *contd.*

Fig. 5.1 shows latitude cuts of observed and modelled nonthermal emission in the first and fourth quadrants of Galactic longitude, spaced at 20° intervals of Galactic longitude (except that a cut at $l = 350^\circ$ is substituted for that at $l = 0^\circ$). There are some features on these cuts which are not included in the model. In the $l = 280^\circ$ cut the extra emission centred on $b = -1^\circ$ is due to the edge of the Vela supernova remnant. The circle of emission from the loop I supernova remnant crosses the plane near $l = 340^\circ$ and the brightest part of its arc of emission crosses again between $l = 20^\circ$ and $l = 40^\circ$ and accounts for the additional emission in the wings of these profiles. The cut at $l = 80^\circ$ passes through the Cygnus region, a nearby complex region of thermal and nonthermal emission which, in our model coincides in direction with the bifurcation of the Orion spur and the Sagittarius arm. As can be seen from Fig. 2.4a the thermal separation technique indicates that the major part of the emission from the Cygnus complex is thermal in origin and the 'observed' nonthermal emission which is in excess of the model could still contain some unidentified thermal emission. It would have been particularly interesting to study the absorption at 34.5 MHz in this region but this was made impossible by the residual side lobes of the very bright Cygnus A radio galaxy which happens to lie in the same direction.

It might be argued that the number of parameters that we have introduced into our model is larger than necessary and that our approach should have been to use the smallest possible number required to turn a two dimensional distribution of intensity into a three dimensional distribution of emissivity. We believe that all of the parameters that make up our model are there for a good reason concerned with the physics of the synchrotron emission and the spiral structure and that they have to be included in any realistic model. Similar arguments might be made about the TC model of the $\langle n_e \rangle$ distribution. Certainly the information from the dispersion measures of the 70 pulsars for which there is some constraint on the distance is not

sufficient to define all the parameters in Table 4.3 as well as fix the spiral structure and they too had to invoke physical arguments and analogies with external galaxies to construct their model.

In chapter 4 we modelled the absorption of the continuum emission at decametre wavelengths by ionised gas and compared it with observation. The aim was to test the line of sight distribution of synchrotron emission in our model and to distinguish between two variants of the distribution of the mean square thermal electron density. The result confirmed that the absorption model of the synchrotron emissivity in the Galactic plane was broadly correct. We were unable to distinguish, however, between the two spiral arm distributions of thermal electrons, for which the main differences were in the form of the arms within 4 kpc of the Galactic centre. The reasons for this were that the available recombination line surveys did not really have sufficient frequency resolution and the inherent distance ambiguity when converting Doppler shifted frequency to the distance along the line of sight. At almost all longitudes the 'observed' transmission of the decametre emission did fall between the predicted limits, corresponding to the assumption that all of the ionised gas was either at the near or far points. In certain directions one may be able to resolve this distance ambiguity. For example at $l \sim 15^\circ$ (Fig 4.18), the thermal emission should come from the near point. Georgelin & Georgelin (1976) showed that there is a giant HII region at 15° situated at about 2.5 kpc. At $l \sim 31^\circ$, the emission should come from the far point while from the Georgelin & Georgelin data, there is a giant HII region at 7 kpc. The way in which these two authors determine the distance is by finding an OB association which coincides in direction with a particular giant HII region. The star spectral types and magnitudes then allow their distance to be estimated with sufficient precision to tell if the region is at the near or far point. Unfortunately it is not possible to identify all of the extended HII regions with specific groups of stars.

If one was completely confident of the model and the observed transmission one could turn the problem around and for each longitude assign the ionised gas between the near and far points in the proportion required to give agreement with observation. This would then give a way of deriving the distribution of the ionised gas in the Galaxy without the distance ambiguity. There are some uncertainties to bear in mind, however. Firstly, in order to obtain the 'observed' transmission we assumed that the spectral index of the unabsorbed radiation would be constant across the plane. If for instance the electron spectrum were flatter in the inner part of the Galaxy (although there is no evidence for this) the spectral index at $b = 0^\circ$ would be lower than we assumed and we would have underestimated the transmission. Secondly, in separating the thermal and nonthermal emission we took the electron temperature in the HII regions to be 7000 K. This is the best estimate of the average for a large number of clouds along the line of sight. If, however, at a particular longitude a large proportion of the thermal emission was contributed by a single cloud its temperature could differ from the mean and the calculated transmission could be wrong. Finally, as already mentioned in chapter 4, there are some uncertainties in the calibration of the Fleurs and GEETEE surveys over the full range of spatial frequencies. The former array no longer exists but the latter is still operating and it may be possible to check the calibration.

For some ranges of l the 'observed' transmission falls outside the range of predictions. One should note that for $40^\circ < l < 48^\circ$, for instance, most of the recombination line Brightness Temperature on the $l - \nu$ plot is defined by only 1 contour level so the calculated transmission cannot be very precise.

5.2 The magnetic field and cosmic ray electron density

The Galactic magnetic field, H and the cosmic ray electron density, N_e occur explicitly in our model but what we have done is to find the distribution of emissivity, which is proportional to $N_e H^{1.8}$, which fits the observations. We have already pointed out that it was only for convenience in the parameterisation that we attributed the radial variation of the emissivity solely to the variation of H and the variation with distance from the Galactic plane, z , to the variation in N_e . In order to separate these two factors one needs independent information concerning one of them. Measurement of the diffuse gamma-ray emission from the Galactic disk provides information on N_e .

The COS-B satellite and the currently operating EGRET detector on the Compton Gamma-Ray Observatory satellite have made such measurements in the energy range 35 MeV to several GeV. Both are multiplate spark chambers operating by the production of positron-electron pairs via which the direction and energy of the incident gamma-rays are measured. EGRET has a larger collecting area and has now collected more data than was got by COS-B. Both have an angular resolution of about 5° for gamma-rays above 100 MeV.

The diffuse component of the gamma-rays from the interstellar medium in this energy range is produced by three processes. Cosmic ray electrons may interact with starlight photons or with photons of the Cosmic Microwave Background via the Inverse Compton interaction. On starlight photons the electron energy required is of the order of 4 GeV while CMB photons require 200 GeV electrons. Outside the gaseous disk of the Galaxy only these gamma-rays are generated but within the disk the other two processes dominate. The second process is Bremsstrahlung of the cosmic ray electrons on the interstellar gas. Typically the gamma-ray produced has 80% of the initial energy of the electron. The Bremsstrahlung gamma-rays are

predominant below about 100 MeV but above this energy the third process takes over. This is π^0 production by the interaction of cosmic ray nuclei, mainly protons, with the interstellar gas, followed by their decay into two gamma-rays. Typically the original protons will have had 3 to 10 times higher energy than the resultant gamma-ray.

The gamma-ray emissivity of the Galactic disk is therefore proportional to the product of the cosmic ray density and the gas density and if the latter is known the former may be deduced. Cosmic ray electrons that generate the 408 MHz emission would produce Bremsstrahlung gamma-rays of 2 to 3 GeV. At this energy the gamma-ray flux is mainly due to the π^0 production and decay. If, however, the cosmic ray electrons and nuclei are produced by similar sources one would expect the ratio of electrons to nuclei to be constant in the Galaxy and a measurement of the diffuse gamma-ray flux should give the required information about the electron density.

Strong and Mattox have analysed the EGRET data obtained in the first 28 months of its operation (A.W. Strong, private communication at 24th International Cosmic Ray Conference, Rome, August 1995) and have obtained a radial distribution of cosmic ray density in the Galaxy. Their method of analysis is the same as used by Strong et al. (1988) on the COS-B data. They remove an isotropic extragalactic background, the Inverse Compton contribution and the flux from identified point sources. They then assume that the observed gamma-ray intensity at longitude, l , can be represented as the sum of the contributions of a series of concentric rings about the Galactic centre each having uniform emissivity as follows:

$$I(E, l) = \sum_{i=1}^n \frac{q_i(E, R)}{4\pi} (N_{HI,i} + 2X(E, R)W_{CO,i}) \quad (5.1)$$

The term $q_i(E, R)$ gives the production of gamma-rays of energy, E , per Hydrogen atom at galactocentric radius, R , and includes the density of cosmic ray

nuclei and electrons as a function of energy and R . The terms in brackets are the total column density of hydrogen atoms in atomic and molecular form. The column density of HI is directly measured but the column density of molecular hydrogen has to be inferred from the Brightness Temperature of the microwave emission from the associated CO gas, W_{CO} , with X as the effective conversion factor. The factor X is R dependent because of the variation of the composition of the interstellar gas. The energy dependence is allowed because of the possibility of the lower energy cosmic rays being partially excluded from dense molecular clouds. Strong et al. tried various combinations of R and E dependence. The simplest case, where both X and the shape of $q(R)$ were taken to be energy independent gave a reasonable fit to the data but the best fit was obtained for a mild energy dependence for X but no energy dependence of the shape of $q(R)$. The latter implies no variation of the shape of the cosmic ray energy spectrum as a function of R and gives some support to our earlier assumption of constant spectral index across the plane. Fig. 5.2 shows the COS-B results of Strong et al. regarding $q(R)$ together with the results of the new EGRET analysis. The former are consistent with the latter, which have higher statistical accuracy.

In Fig. 5.3 we show the radial dependence of the underlying magnetic field strength normalised to its value at the sun. The solid line is a plot of the expression 3.12 in our model which shows the radial dependence required to give the radial dependence of synchrotron emissivity which fits the observations under the assumption that N_e is independent of R . As the emissivity is $\propto N_e H^{1.8}$ one may obtain the true $H(R)$ by dividing expression 3.12 by $(N_e(R)/N_e(R_0))^{1/1.8}$ as also shown in Fig. 5.3. Apart from the rapid variation of H required in the inner 2.5 kpc of the Galaxy our picture is then of a field strength falling slowly with R . One can also see that the variation does not fit $N_e \propto H^2$ as would be required by equipartition of energy density between the cosmic rays and the magnetic field. Our evidence is

Gamma ray emissivity $E > 100$ MeV

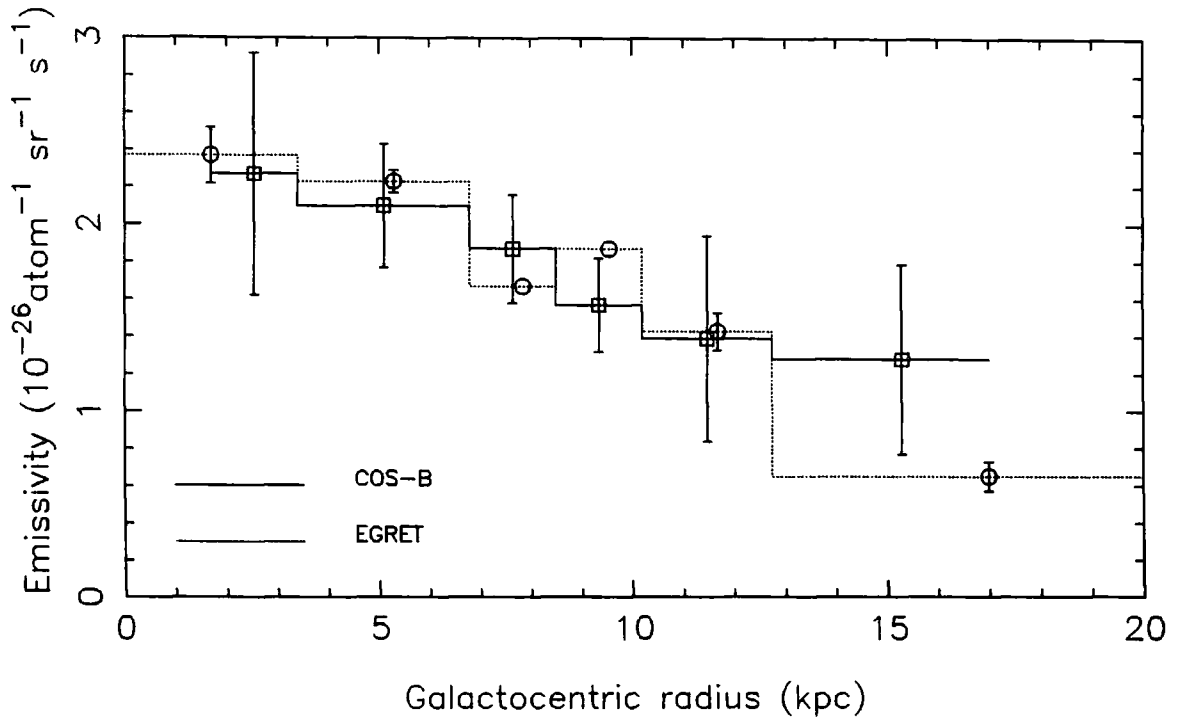


Figure 5.2: The gamma-ray emission per atom of hydrogen as a function of Galactocentric radius as derived by Strong et al.(1988) from COS-B data(solid line histogram) and by Strong and Mattox(private communication) from EGRET data(dotted line). We have adjusted their radius scale to put the Sun at $R = 8.5$ kpc. Some of the EGRET data points have been offset from the centres of their bins so that error bar can be seen.

that except at the outermost part of the Galaxy the magnetic field energy density has a stronger radial variation than does that of the cosmic rays. The equipartition argument, though often invoked, is not so easy to justify. It has been widely used to infer the total energy involved in providing the synchrotron emission of radio galaxies where there is no independent evidence for the magnetic field strength: the combination of field strength and cosmic ray flux which produces the observed luminosity and at the same time gives the most conservative estimate of the total energy in field and cosmic rays is that which is close to equipartition. One has no guarantee that this minimum total energy situation is always the case, however.

When considering the stability of the cosmic ray, magnetic field and interstellar gas system in spiral Galaxies the picture is that the gas layer is held down by its self-gravitation and the gravitational field of the stellar disk. The magnetic field is largely frozen in to the gas by the conductivity of the interstellar medium and the cosmic rays are in turn tied to the magnetic field. When considering the need for energy equipartition it is important to remember that both the cosmic rays and the magnetic field are providing outward pressure on this system. It is true that the energy density of cosmic rays cannot be very much greater than that of the field because, if it were the field orientation would tend to be perpendicular to the disk as the cosmic rays escaped from the Galaxy. There is no reason, however, why the magnetic field energy density should not be much greater than that of cosmic rays in some regions, as indeed seems to be the case in the inner parts of the Galaxy.

The gamma-ray data has as yet given no clear information about the z -dependence of the cosmic ray flux. The polynomial expression 3.5 gives the required variation under the assumption of no z -dependence of H (apart from the demodulation of the spiral arm compression). If one takes it that H will actually be a decreasing function of z then equation 3.5 gives the minimum rate that N_e can decrease with z . One can reverse the argument and infer that the $1/1.8$ root of

expression 3.5 gives the maximum rate of decrease of H with z assuming only that N_e must be a constant or decreasing function of z . This is a useful constraint when discussing the effect of the magnetic field on the stability of the galactic disk.

5.3 Global emission of the Galaxy

It is useful to give the values of the global emission of the Galaxy that our model implies. Integrating our model distributions we find that at 408 MHz the nonthermal luminosity is $6.1 \times 10^{21} \text{ W Hz}^{-1}$. The thermal luminosity at the same frequency is $1.5 \times 10^{20} \text{ W Hz}^{-1}$. The small ratio of total thermal to nonthermal emission may seem surprising when one considers the significant fraction of thermal Brightness Temperature in the Galactic plane profile of Fig. 2.7. The reason is the much smaller thickness of the thermal emission disk compared with the nonthermal disk and halo.

The infrared luminosity of the Galaxy in the $100 \mu\text{m}$ band as given by the work of Broadbent et al. (1989) after scaling to the revised size is $1.2 \times 10^{24} \text{ W Hz}^{-1}$. There is a tight correlation between the infrared and radio continuum luminosities of spiral galaxies (Hummel et al. 1988). The ratio for our Galaxy agrees closely with that for other Sbc galaxies.

As an illustration of the form of the Galactic halo that our model describes we show in Fig. 5.4 the predicted external edge on view. Of the few external spiral galaxies that are sufficiently edge-on and nearby for a radio continuum halo to be observed that most nearly resembling this form is NGC 4631.

5.4 Future Work

Further developments of our method of using the absorption due to the ionised gas to check and improve the synchrotron model depend mainly on im-

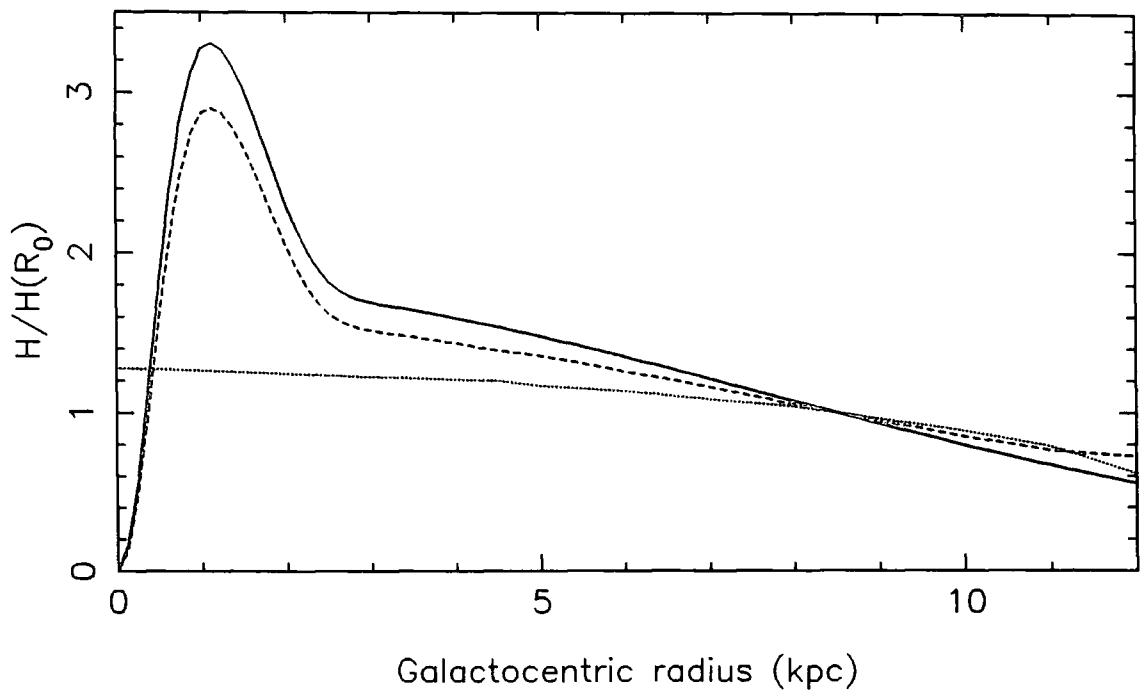


Figure 5.3: The radial variation of underlying field strength, $H(R)$, in the Galaxy normalised to that at the Sun. The solid line shows that value given by our model under the assumption that there is no R -dependence in the cosmic ray density, N_e . The dotted line shows $(N_e(R)/N_e(R_o))^{1/1.8}$ as derived from a weighted fit to the data in Fig.5.2. The dashed line shows our estimate of the actual radial variation of $H(R)$ obtained by dividing the first curve by the second.

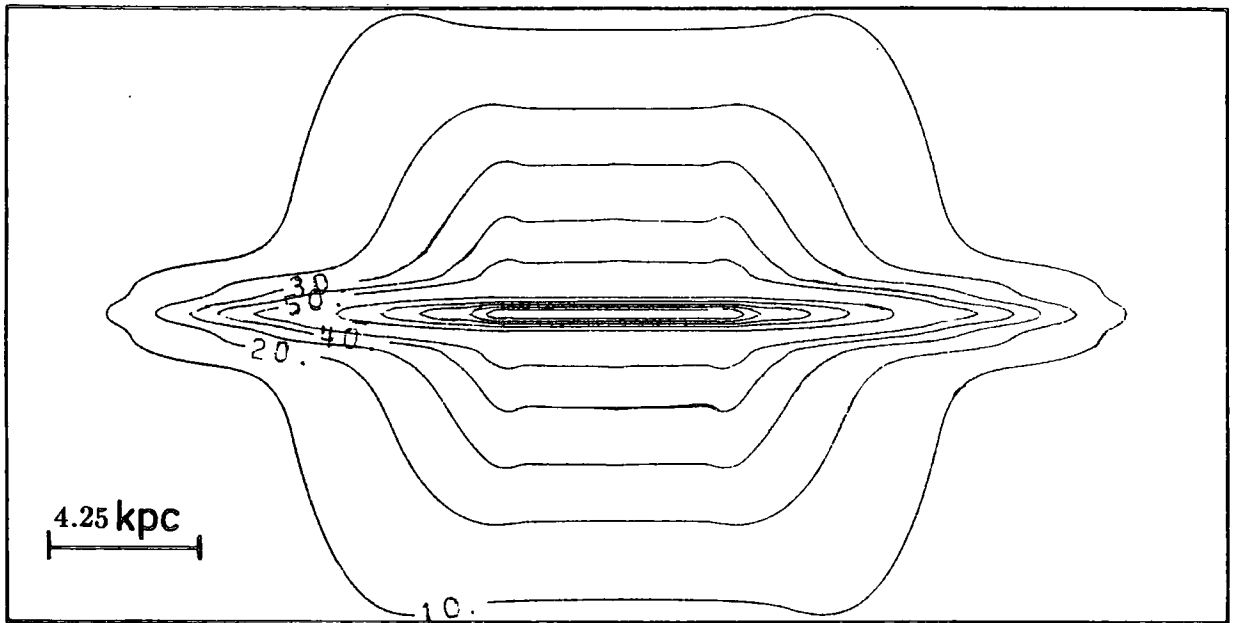


Figure 5.4: The distribution of surface brightness temperature at 408 MHz of the Galaxy viewed edge-on according to our model. The contour are plotted every 10 K from 10 K to 50 K and every 50 K beyond 50 K

improvements in the angular and velocity resolutions of the recombination line surveys. There is no particular problem in improving the latter. Longer integration times with the largest single dish telescopes would increase the sensitivity and allow narrower channels in the frequency domain. The problem of the distance ambiguity would remain but with the range of distances about the two allowed choices reduced it would be less likely that both near and far choices would correspond to the possible position of a spiral arm. A 2-dimensional survey in both l and b is, of course desirable, allowing a three-dimensional picture of the ionised gas distribution. Regarding improvements in the angular resolution, these could only come about by using aperture synthesis rather than single dish instruments as the frequency is fixed by the need to study the $H166\alpha$ line in order to be sensitive to the ionised gas of the appropriate density. A survey at the $4'$ resolution of the IRAS and Parkes 6 GHz continuum surveys would be ideal but such a large scale aperture synthesis survey is a long way off.

We have already remarked that our model aims at describing the synchrotron emission on a scale of detail of typically ~ 130 pc. If one surveys the nonthermal emission at a higher angular resolution then, to a certain extent there is just more detail to explain. However such detail may help to confirm or deny the picture of Galaxy wide shocks being formed by the collisions of clouds in the spiral arms that we have adopted to explain the enhanced emission in the arms. It may also give more information on the rôle of supernova explosions and stellar winds in disrupting the regular field in the arms. There is a recently published Parkes survey of the galactic plane at 2.4 GHz with an angular resolution of $10'$ (Duncan et al., 1995), which shows a considerable amount of detail including low surface brightness loops and spurs which are probably nonthermal features. The Durham group is playing a part in the analysis of data from the new Mauritius Radio Telescope. This operates at 150 MHz where the nonthermal features would be stronger. Data has already

been collected to give a 10' resolution map of the southern hemisphere. Ultimately a 4' resolution map will be produced.

Radio Astronomy, since its birth 65 years ago, has lead to the discovery of the most distant and energetic objects in the universe. Nevertheless the problems that were tackled by the two lone radio astronomers, Jansky and Reber, in the first decade of its life, namely, identifying the processes that generate radio waves in between the stars in our own Galaxy and how they vary from place to place, are still well worth further study.

List of symbols in general use in this thesis

b	galactic latitude
c	velocity of light
e	electron mass
E	cosmic ray energy
h	Planck constant
H	magnetic field intensity in Gauss
I	radiation intensity
k	Boltzmann constant
l	galactic longitude
m	electron mass
n_e	thermal electron number density
n_i	ion number density
N_e	cosmic ray electron intensity per GeV at 1 GeV
R	distance from the Galactic centre
R_\odot	distance of the Sun from the Galactic centre
s	path length along the line of sight
T_e	electron temperature
T_b	brightness temperature
v	velocity
w	angular frequency
z	height above the Galactic plane
Z	atomic number
α	spectral index
ν	frequency
ϵ	emissivity
κ	absorption coefficient
τ	optical depth

References

- Alfvén, H. & Herlofson, N., 1950. *Phys. Rev.*, **78**, 616.
- Altenhoff, W., Mezger, P.G., Wendker, H. & Westerhout, G., 1960. *Veröff. Sternwarte*, Bonn, No.59, p.48.
- Beck, R. & Reich, W., 1985. In: *The Milky Way Galaxy, IAU Symp. No. 106*, p.239, eds. van Woerden, H., Allen, R.J. & Burton, W.B., Reidel, Dordrecht.
- Berkhuijsen, E.M., Haslam, C.G.T. & Salter, C.J., 1971. *Astr. Astrophys.*, **14**, 252.
- Beuermann, K., Kanbach, G. & Berkhuijsen, E.M., 1985. *Astr. Astrophys.*, **153**, 17.
- Blitz, L., Fich, M. & Kulkarni, S., 1983. *Science*, **220**, No.4603, 1233
- Blitz, L., Binney, J., Lo, K.Y., Bally, J. & Ho, P.T.P., 1993. *Nature*, **361**, 417.
- Bok, B.J., 1983. *Astrophys. J.*, **273**, 411.
- Brindle, C., French, D.K. & Osborne, J.L., 1978. *Mon. Not. R. astr. Soc.*, **184**, 283.
- Broadbent, A., 1989. *PhD thesis*, University of Durham.
- Broadbent, A., Haslam, C.G.T & Osborne, J.L., 1989. *Mon. Not. R. astr. Soc.*, **237**, 381.
- Burton, W.B., 1971. *Astr. Astrophys.*, **10**, 76.
- Burton, W.B. & Gordon, M.A., 1978. *Astr. Astrophys.*, **63**, 7.
- Caswell, J.L. & Haynes, R.F., 1987. *Astr. Astrophys.*, **171**, 261.
- Cersosimo, J.C., Azcárate, I.N., Hart, L. & Colomb, F.R., 1989. *Astr. Astrophys.*, **208**, 239.
- Chi, X. & Wolfendale, A.W., 1990. *J. Phys. G:Nucl. Part. Phys.*, **16**, 1409.
- Clemens, D.P., 1985. *Astrophys. J.*, **295**, 422.
- Cohen, R.S., Cong, H., Dame, T.M. & Thaddeus, P., 1980. *Astrophys. J.*, **239**, L53.
- Cohen, R.S., Grabelsky, D.A., Alvarez, H., Bronfman, L., May, J. & Thaddeus, P., 1985. *Astrophys. J.*, **290**, L15.
- Cox, P., Krügel, E. & Mezger, P.G., 1986. *Astr. Astrophys.*, **155**, 380.

- Downes, D., Wilson, T.W., Bieging, J. & Wink, J., 1980. *Astr. Astrophys. Suppl.*, **40**, 379.
- Duncan, A.R., Stewart, R.T., Haynes, R.F. & Jones, K.L., 1995. *Mon. Not. R. astr. Soc.*, **277**, 36.
- Dwarakanath, K.S. & Uday Shankar, N., 1990. *Astr. Astrophys.*, **11**, 323.
- Ellis, R.S. & Axon, D.J., 1978. *Astrophys. Space Sci.*, **54**, L973.
- French, D.K. & Osborne, J.L., 1976. *Mon. Not. R. astr. Soc.*, **174**, 267.
- French, D.K., 1977. *PhD thesis*, University of Durham.
- Georgelin, Y.M. & Georgelin, Y.P., 1976. *Astr. Astrophys.*, **49**, 57.
- Gerola, H. & Seiden, P.E., 1978. *Astrophys. J.*, **223**, 129.
- Golden, R.L., Grimani, C., Kimbell, B.L., Stephens, S.A., Stochaj, S.J. & Webber, W.R., 1994. *Astrophys. J.*, bf 436, 769.
- Grabelsky, D.A., Cohen, R.S., Bronfman, L., May, J., & Thaddeus, P., 1985. *Astrophys. J.*, **315**, 122.
- Greenberg, J.M. & Hong, S.S., 1974. In: *Galactic and Radio Astronomy, IAU Symp. No. 60*, p.155, ed. Kerr, F. & Simonson, S.C., Reidel, Dordrecht.
- Haslam, C.G.T., Quigley, M.J.S. & Slater, C.J., 1970. *Mon. Not. R. astr. Soc.*, **147**, 405.
- Haslam, C.G.T., Wilson, W.E., Graham, D.A. & Hunt, G.C., 1974. *Astr. Astrophys. Suppl.*, **13**, 359.
- Haslam, C.G.T., Klein, U., Slater, C.J., Stoffel, H., Wilson, W.E., Cleary, M.N., Cooke, D.J. & Thomasson, P., 1981. *Astr. Astrophys.*, **100**, 209.
- Haslam, C.G.T. & Osborne, J.L., 1987. *Nature*, **327**, 211.
- Haslam, C.G.T., Slater, C.J., Stoffel, H. & Wilson, W.E., 1982. *Astr. Astrophys. Suppl.*, **47**, 1.
- Haynes, R.F., Caswell, J.L. & Simons, L.W.J., 1978. *Aust. J. Phys. Astrophys. Suppl.*, **45**, 1.

- Heiles, C., 1987. In: *Interstellar Processes*, p.171, eds. Hollenbach, D.J. & Thronson, H.A., Reidel, Dordrecht.
- Hiltner, W.A., 1951. *Astrophys. J.*, **114**, 241.
- Horellou, C., Beck, R., Berkhuijsen, E.M., Krause, M. & Klein, U., 1992. *Astr. Astrophys.*, bf 265, 417.
- Hummel, E., Davies, R.D., Wolstencroft, R.D., van der Hulst, J.M. & Pedler, A., 1988. *Astr. Astrophys.*, **199**, 91.
- Jones, B.B. & Finlay, E.A., 1974. *Aust. J. Phys.*, **27**, 687.
- Kearsey, S., 1983. *PhD thesis*, University of Durham.
- Kiepenheuer, K.U., 1950. *Phys. Rev.*, **79**, 738.
- Kraus, J.D., 1966. In: *Radio Astronomy.*, McGraw - Hill., New York.
- Krause, M., Beck, R. & Hummel, E., 1989. *Astr. Astrophys.*, **217**, 17.
- Kulkarni, S.R. & Heiles, C., 1987. In: *Interstellar Processes*, p.87, eds. Thronson, H. & Hollenbach, D., Reidel, Dordrecht.
- Landecker, T.L & Wielebinski, R., 1970. *Aust. J. Phys. Astrophys. Suppl.*, **16**, 1.
- Lawson, K.D., Mayer, C.J., Osborne, J.L. & Parkinson, M.L., 1987. *Mon. Not. R. astr. Soc.*, **225**, 307.
- Lin, C.C., 1970. In: *Galactic Astronomy*, **2**, eds. Gordon & Breach.
- Lin, C.C. & Bertin, G., 1985. In: *The Milky Way Galaxy.*, *IAU Symp. No. 106*, p.513, eds. Woerden, H.V., Allen, R.J. & Burton, W.B., Reidel, Dordrecht.
- Lin, C.C. & Shu, F.H., 1964. *Astrophys. J.*, **140**, 646.
- Lin, C.C. & Shu, F.H., 1966. *Proc. Nat. Acad. Sci.*, **55**, 229.
- Lin, C.C., Yuan, C. & Shu, F.H., 1969. *Astrophys. J.*, **155**, 721.
- Lizst, H.S., 1985. In: *The Milky Way*, *IAU Symp. No. 106*, p.283, eds. van Woerden, H., Allen, R.J., Burton, W.B., Reidel, Dordrecht.
- Lockman, F.J., 1976. *Astrophys. J.*, **209**, 429.
- Lockman, F.J., 1979. *Astrophys. J.*, **232**, 761.

- Manchester, R.N., 1974. *Astrophys. J.*, **188**, 637.
- Manchester, R.N. & Taylor, J.H., 1977. In: *Pulsars*, W.H.Freeman, San Francisco.
- McKee, C.F. & Ostriker, J.P., 1977. *Astrophys. J.*, **218**, 148.
- Meyer, C.F., 1974. In: *Origin of cosmic rays*, p.233, eds. Osborne, J.L. & Wolfendale, A.W., D.Reidel, Dordrecht.
- Menzel, D.H., 1968. *Nature*, **218**, 756.
- Mezger, P.G., 1978. *Astr. Astrophys.*, **70**, 565.
- Mezger, P.G., Mathis, J.S. & Panagia, N., 1982. *Astr. Astrophys.*, **105**, 372.
- Mezger, P.G., & Smith, L.F., 1975. In: *Proc. of the 3rd European Astronomy Meeting, Tbilisi*, p.369, ed. Kharadze, E.K., Acad. Sci. Georgian SSR.
- Mills, B.V., 1959. In: *Proc. Int. Astron. Union Symposium*, No.9, New York Academic Press, 431.
- Milogradov-Turin, J., 1984. *Mon. Not. R. astr. Soc.*, **208**, 379.
- Milogradov-Turin, J. & Smith, F.J., 1973. *Mon. Not. R. astr. Soc.*, **161**, 269.
- Pauliny-Toth, I.I.K. & Shakeshaft, J.R., 1962. *Mon. Not. R. astr. Soc.*, **124**, 61.
- Phillipps, S., Kearsley, S., Osborne, J.L., Haslam, C.G.T., & Stoffel, H., 1981a. *Astr. Astrophys.*, **98**, 286.
- Phillipps, S., Kearsley, S., Osborne, J.L., Haslam, C.G.T., & Stoffel, H., 1981b. *Astr. Astrophys.*, **103**, 405.
- Reber, G., 1944 *Astrophys. J.*, **100**, 279.
- Reich, W., Fürst, E., Steffen, P., Reif, K. & Haslam, C.G.T., 1984. *Astr. Astrophys. Suppl.*, **58**, 197.
- Reinhardt, M. & Schmidt-Kaler, T., 1979. *Astrophys. Space Sci.*, **66**, 121.
- Reynolds, R.J., 1984. *Astrophys. J.*, **282**, 191.
- Reynolds, R.J., 1985. *Astrophys. J.*, **298**, L27.
- Roberts, W.W., 1969 *Astrophys. J.*, **158**, 123.
- Roberts, W.W. & Yuan, C., 1970. *Astrophys. J.*, **161**, 877.

- Roberts, W.W., Roberts, M.S. & Shu, F.H., 1975. *Astrophys. J.*, **196**, 381.
- Roberts, W.W., & Hausman, M.A., 1984. *Astrophys. J.*, **277**, 744.
- Robinson, B.J, McCutcheon, W.H., Manchester, R.N. & Whiteoak, J.B., 1983. In: *Surveys of the Southern Galaxy*, p.1, eds. Burton, W.B. & Israel, F.P.
- Salter, C.J. & Brown, R.L., 1988. In: *Galactic and Extra-galactic Radio Astronomy*, p.1, eds. Verschuur, G.L, & Kellermann, K.I., Springer - Verlag New York, New York.
- Sanders, D.B., Clemens, D.P., Scoville, N.Z., Solomon, P.M., 1986. *Astrophys. J. Suppl. Ser.*, **60**, 1.
- Sanders, D.B. & Mirabel, I.F., 1985. *Astrophys. J.*, **298**, L31.
- Schmidt, M., 1965. In: *Galactic Structure, Stars and Stellar Systems*, **5**, 513, eds. Blaaw, A. & Schmidt, M.
- Schmidt-Kaler, T. & Wiegandt, R., 1980. *Astr. Astrophys.*, **89**, 67.
- Seiden, P.E. & Gerola, H., 1979. *Astrophys. J.*, **233**, 56.
- Shaver, P.A. & Goss, W.M., 1970. *Aust. J. Phys. Astrophys. Suppl.*, **14**, 133.
- Shu, F.H., Milione, V. & Roberts, W.W., 1973. *Astrophys. J.*, **183**, 819.
- Simard-Normandin, M. & Kronberg, P.P., 1980. *Astrophys. J.*, **242**, 74.
- Simonson, S.C., 1976. *Astr. Astrophys.*, **46**, 261.
- Solomon, P.M., Sanders, D.B., & Rivolo, A.R., 1985. *Astrophys. J.*, **292**, L19.
- Strong, A.W., Bloeman, J.B.G.M., Dame, T.M., Grenier, I.A., Hermsen, W., Lebrun, L.-A. Nyman, Pollock, A.M.T. & Thaddeus, P., 1988. *Astr. Astrophys.*, **207**, 1.
- Taylor, J.H. & Cordes, J.M., 1993. *Astrophys. J.*, **411**, 674.
- Troland, T.H. & Heiles, C., 1986. *Astrophys. J.*, **301**, 339.
- Toomre, A., 1969. *Astrophys. J.*, **158**, 899.
- Toomre, A., 1977. *Ann. Rev. Astr. Astrophys.*, **15**, 478.
- Toomre, A., 1981. In: *The Structure and Evolution of Normal Galaxies*, eds. Fall, S.M. & Lynden- Bell, D., C.U.P., Cambridge.

Weaver, H., 1970. *IAU Symp. No. 38*, p.126. D.Reidel, Dordrecht.

Weaver, H., 1974. In: *Galactic Radio Astronomy, IAU Symp. No. 6*, p.573, eds. Kerr, F.J. & Simonson, S.C. D.Reidel, Dordrecht.

Weaver, H. & Williams, D.R.W., 1973. *Astr. Astrophys. Suppl.*, **8**, 1.